



Deliverable No.6.2

CHIC Cancer Component Models: Initial Tested Versions

Grant Agreement No.: 600841
 Deliverable No.: D6.2
 Deliverable Name: CHIC Cancer Component Models: Initial Tested Versions
 Contractual Submission Date: 1/12/2014
 Actual Submission Date: 5/1/2015

Dissemination Level		
PU	Public	
PP	Restricted to other programme participants (including the Commission Services)	
RE	Restricted to a group specified by the consortium (including the Commission Services)	
CO	Confidential, only for members of the consortium (including the Commission Services)	X



COVER AND CONTROL PAGE OF DOCUMENT	
Project Acronym:	CHIC
Project Full Name:	Computational Horizons In Cancer (CHIC): Developing Meta- and Hyper-Multiscale Models and Repositories for In Silico Oncology
Deliverable No.:	D6.2
Document name:	CHIC cancer component models:initial tested versions
Nature (R, P, D, O) ¹	R
Dissemination Level (PU, PP, RE, CO) ²	CO
Version:	1 (Finalized)
Actual Submission Date:	5/1/2015
Editor:	Georgios S. Stamatakis
Institution:	ICCS-NTUA
E-Mail:	gestam@mail.ntua.gr

ABSTRACT:

The purpose of this deliverable is to present the initial tested versions of a number of representative component models (hypomodels) in relation to workpackage WP6 of the CHIC project. In order to demonstrate the integrative modelling character of CHIC as well as the great potential of combining hypomodels of biomechanisms developed by different modellers or modelling teams across the globe, one of the main clinical scenarios of the CHIC project, namely the lung cancer scenario, has been selected to serve as the driver of the particular hypomodel development. The types of multiscale clinical data being provided by the Pathology Department of the University of Saarland, Homburg, Germany have served as the clinical driver of the hypermodel and its constituent component models (hypomodels). A master topology of the corresponding hypermodel is presented. The relevant hypomodels have been developed by different modelling partners of the CHIC project. For each hypomodel its main tasks, its input and output parameters as well as several indicative behaviour and testing results are presented. A metamodeling description of each hypomodel based on the CHIC 13 perspective approach, which will facilitate its technology mediated linking, is provided. A brief outline of the initial architecture of the multimodeller hypermodels concerning the nephroblastoma and the glioblastoma multiforme scenarios of the CHIC project, currently under development and/or refinement, is also included. Last but not least some important strategy aspects of the CHIC project are presented in order to provide a broader view of the CHIC project deployment principles. A practical vocabulary is provided at the end of the document.

¹ R=Report, P=Prototype, D=Demonstrator, O=Other

² PU=Public, PP=Restricted to other programme participants (including the Commission Services), RE=Restricted to a group specified by the consortium (including the Commission Services), CO=Confidential, only for members of the consortium (including the Commission Services)

KEYWORD LIST:

cancer modelling, multiscale cancer modelling, hypermodelling, CHIC project, hypermodel, hypomodel, component model, tumour growth, angiogenesis, cancer biomechanics, molecular cancer modelling, integrated cancer model, hypermodel based oncosimulator, *in silico* oncology, *in silico* medicine, systems medicine, computational oncology, computational medicine, systems oncology, finite element method, discrete event, discrete entity, partial differential equation, ordinary differential equation

The research leading to these results has received funding from the European Community's Seventh Framework Programme (FP7/2007-2013) under grant agreement n° 600841.

The author is solely responsible for its content, it does not represent the opinion of the European Community and the Community is not responsible for any use that might be made of data appearing therein.

MODIFICATION CONTROL			
Version	Date	Status	Author
1.0	10/11/2014	Draft	G. Stamatakos, ICCS-NTUA
2.0	20/11/2014	Draft	G. Stamatakos, ICCS-NTUA
3.0	27/11/2014	Draft	G. Stamatakos, ICCS-NTUA
4.0	30/11/2014	Revision	G. Stamatakos, ICCS-NTUA
5.0	10/12/2014	Revision	G. Stamatakos, ICCS-NTUA
6.0	3/1/2015	Revision	D. Dionysiou, ICCS-NTUA
7.0 → 1 (Finalized)	4/1/2015	Revision (Finalized)	G. Stamatakos, ICCS-NTUA

List of (additional) contributors

E. Kolokotroni, ICCS-NTUA
 J. A. Grogan, UOXF
 J. Pitt-Francis, UOXF
 P. K. Maini, UOXF
 H. M. Byrne, UOXF
 K. Argyri, ICCS-NTUA
 D. Abler, UBERN
 F. Rikhtegar, UBERN
 P. Büchler, UBERN
 R. Radhakrishnan, UPENN
 E. J. Jordan, UPENN
 V. Sakkalis, FORTH
 E. Tzamali, FORTH
 K. Marias, FORTH
 C. Guiot, UNITO
 E. Venturino, UNITO
 I. Stura, UNITO
 D. Gabriele, UNITO
 E. Georgiadi, ICCS-NTUA
 E. Ouzounoglou, ICCS-NTUA
 M. Antonopoulos, ICCS-NTUA
 M. Viceconti, USFD
 R. Bohle, USAAR
 N. Graf, USAAR
 S. Gool, KUL

Contents

Executive Summary.....	7
I. Introduction.....	9
I1. Purpose and Outline of the Document.....	9
I2. The Master Topology of the First Multimodeller Hypermodel Demonstrator	9
T. The (pure) tumour growth and response to treatment component model.....	11
T1. Introduction.....	11
T2. Model Description.....	12
T3. Parametric Investigation of the Model.....	23
T4. The Lung Cancer Clinical Adaptation Paradigm.....	39
T5. References.....	49
T6. Description of the (Pure) Tumour Growth and Response to Treatment Component Model (T) through the 13 Perspectives.....	57
A. The Vascular/Angiogenesis Component Model.....	59
A1. Introduction.....	59
A2. Hypomodel Description.....	60
A3. Standalone Testing.....	63
A4. Integration.....	65
A5. Further Details.....	69
A6. References.....	69
A7. Description of the The Vascular/Angiogenesis Component Model (A) through the 13 Perspectives.....	71
AA. An Alternative Vascular / Angiogenesis Component Model.....	73
AA1. Introduction.....	73
AA2. Basic Features of the Component Model.....	74
AA3. Reproducing a Series of <i>In Vivo</i> Experiments in Mice Treated with Bevacizumab.....	82
AA4. References.....	85
AA5. Description of the Alternative Vascular / Angiogenesis Component Model (AA) through the 13 Perspectives.....	87
B. The Tumour Growth Biomechanics Component Model.....	89
B1. Introduction.....	89
B2. Scientific Background.....	90
B3. Coupled Model for Realistic Tumour Growth.....	92
B4. Biomechanical and Diffusion Modelling.....	93
B5. Application to Lung Cancer.....	98
B6. Conclusions.....	102
B7. Appendix.....	103
B8. References.....	105
B9. Description of the The Tumour Growth Biomechanics Component Model (B) through the 13 Perspectives.....	109
M. The Subcellular (Atomistic and Molecular) Component Models.....	111
M1. Introduction.....	111
M2. Layer 1.....	111
M3. Layer 2.....	111
M4. Layer 3.....	111
M5. Integration Layer.....	112
M6. Testing, Implementation, and Integration of the Subcellular Models.....	113

M7 Detailed Description and Implementation of the Subcellular Components.....	115
M8. Conclusion.....	121
M9. Description of the Subcellular (Atomistic and Molecular) Component Models (M) through the 13 Perspectives.....	122
N. Potential Addition of a Separate Metabolic Network.....	124
N1. A Brief Outline of the Potential Component Model.....	124
N2. References.....	127
N3. Description of the Potential Addition of a Metabolic Network (N) through the 13 Perspectives.....	128
U. Gross Component Models Based on Simplified Universal Growth Laws.....	130
U1. Model Description.....	130
U2. Model Input.....	130
U3. Model Output.....	131
U4. Sensitivity Analysis.....	131
U5. Flowchart.....	137
U6. References.....	137
U7. Description of the Gross Component Models Based on Simplified Universal Growth Laws through the 13 Perspectives.....	139
A BRIEF INITIAL OUTLINE OF THE TWO ADDITIONAL MULTIMODELLER HYPERMODEL DEMONSTRATORS.....	141
W. The Wilms Tumour (Nephroblastoma) Demonstrator.....	142
W1. An Initial Version of the Topology of the Nephroblastoma multi-modeller hyermodel.....	142
W2. Cellular and Supercellular Level.....	143
W3. Sub-cellular Level.....	143
W4. References.....	143
G. The Glioblastoma Demonstrator.....	145
G1. Introduction.....	145
G2. An Initial Master Topology of the GBM Hypermodel.....	146
G3. References.....	147
S. An Outline of the Overall Strategy of the CHIC Project.....	149
V. VOCABULARY.....	151
V1. Definitions.....	151
C. Conclusion.....	157
Appendix 1 – Abbreviations and Acronyms.....	158

1. Executive Summary

Developing robust, reproducible, interoperable and collaborative hyper-models of diseases and normal physiology is a sine qua non necessity if rational, coherent and comprehensive exploitation of the invaluable information hidden within human multiscale biological data is envisaged. Responding to this imperative in the context of both the broad Virtual Physiological Human (VPH) initiative and the paradigmatic cancer domain, CHIC proposes the development of a suite of tools, services and secure infrastructure that will support accessibility and reusability of VPH mathematical and computational hypermodels. These will include a hypermodelling infrastructure consisting primarily of a hypermodelling editor and a hypermodelling execution environment, an infrastructure for semantic metadata management, a hypermodel repository, a hypermodel-driven clinical data repository, a distributed metadata repository and an in silico trial repository for the storage of executed simulation scenarios. Multiscale models and data will be semantically annotated using the ontological and annotating tools to be developed. An image processing and visualization toolkit, and cloud and virtualization services will also be developed. The CHIC tools, services, infrastructure and repositories will provide the community with a collaborative interface for exchanging knowledge and sharing work in an effective and standardized way. A number of open source features and tools will enhance usability and accessibility. In order to ensure clinical relevance and foster clinical acceptance of hypermodelling in the future, the whole endeavour will be driven by the clinical partners of the consortium. Cancer hypermodels to be collaboratively developed by the consortium cancer modellers will provide the framework and the testbed for the development of the CHIC technologies. Clinical adaptation and partial clinical validation of hypermodels and hypermodel oncosimulators will be undertaken.

The aim of this document is to present the initial tested versions of a number of representative component models (hypomodels) in relation to workpackage WP6 of the CHIC project. In order to demonstrate the integrative modelling character of CHIC as well as the great potential of combining hypomodels of biomechanisms developed by different modellers or modelling teams across the globe, one of the main clinical scenarios of the CHIC project, namely the lung cancer scenario, has been selected to serve as the driver of the particular hypomodel development. The types of multiscale clinical data being provided by the Pathology Department of the University of Saarland, Homburg, Germany have served as the clinical driver of the hypermodel and its constituent component models (hypomodels). A master topology of the corresponding hypermodel is presented. The relevant hypomodels have been developed by different modelling partners of the CHIC project. They include a pure tumour growth hypomodel, which also acts as the hypermodel integrator, two alternative vascular / angiogenesis components, a tumour growth biomechanics hypomodel, and a number of subcellular (atomistic and molecular) hypomodels. In parallel a number of gross phenomenological simplistic models of tumour growth and response to treatment based on universal growth laws have been developed in order to provide a rough but useful method of preliminarily checking the composite and detailed multimodeller hypermodel.

For each hypomodel its main tasks, its input and output parameters as well as several indicative behaviour and testing results are presented. A metamodelling description of each hypomodel based on the CHIC 13 perspective approach which will facilitate its technology mediated linking is provided. A brief outline of the initial architecture of the multimodeller hypermodels concerning the nephroblastoma and the glioblastoma multiforme scenarios of the CHIC project, currently under development and/or refinement, is also included. Last but not least some important strategy aspects

of the CHIC project are presented in order to provide a broader view of the CHIC project deployment principles. A practical vocabulary is provided at the end of the document.

I. Introduction

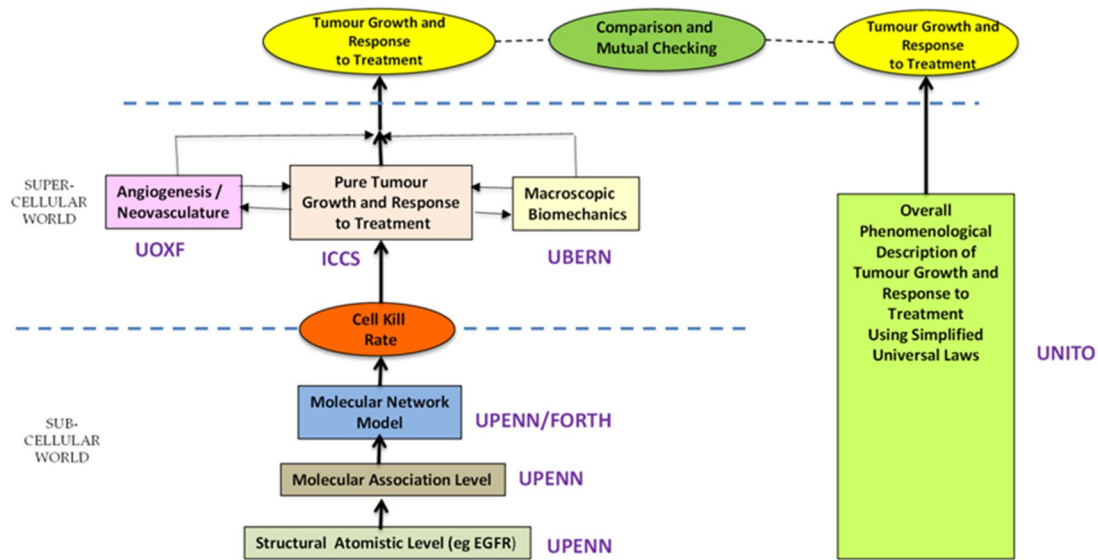
I1. Purpose and Outline of the Document

In this deliverable the initial tested versions of a number of representative component models (hypomodels) in relation to workpackage WP6 of the CHIC project are presented. In order to demonstrate the integrative modelling character of CHIC as well as the great potential of combining hypomodels of biomechanisms developed by different modellers or modelling teams across the globe, one of the main clinical scenarios of the CHIC project, namely the lung cancer scenario, has been selected to serve as the driver of the particular hypomodel development. The types of multiscale clinical data being provided by the Pathology Department of the University of Saarland, Homburg, Germany have served as the clinical driver of the hypermodel and its constituent component models (hypomodels).

A master topology of the corresponding hypermodel is presented. The relevant hypomodels have been developed by different modelling partners of the CHIC project. For each hypomodel its main tasks, its input and output parameters as well as several indicative behaviour and testing results are presented. A metamodeling description of each hypomodel based on the CHIC 13 perspective approach which will facilitate its technology mediated linking is provided. A brief outline of the initial architecture of the multimodeller hypermodels concerning the nephroblastoma and the glioblastoma multiforme scenarios of the CHIC project, currently under development and/or refinement, is also included. Last but not least some important strategy aspects of the CHIC project are presented in order to provide a broader view of the CHIC project deployment principles. A practical vocabulary is provided at the end of the document.

I2. The Master Topology of the First Multimodeller Hypermodel Demonstrator

In order to demonstrate the possibility of the development of a cancer hypermodel to be developed by different cancer modelling groups based at different physical locations on the globe, the master topology shown in Fig. L1 and concerning the clinical scenario of lung cancer has been proposed. The demonstrator consists of two modelling pylons. On the left hand side a multimodeller hypermodel provides a detailed multiscale simulator of the complex phenomenon of *in vivo* tumour growth and response to treatment ("first pylon"). On the right hand side a set of simplistic hypomodels provide a gross description of the same phenomenon ("second pylon").



**CHIC WP6 MASTER TOPOLOGY OF THE LUNG CANCER
MULTI-MODELLER HYPERMODEL**

Fig. L1. The master topology of the first multimodeller hypermodel concerning the lung cancer scenario.

In more detail our approach is as follows. ICCS has undertaken the development of the pure tumour growth hypomodel as well as the integration of the hypomodels developed by other partners in order to end up with the integrated multiscale hypermodel concerning angiogenetic tumour growth and response to treatment. UOXF has undertaken the development of the tumour related angiogenesis hypomodel. UBERN has undertaken the development of the macroscopic biomechanics hypomodel. UPENN has been charged with the development of a composite hypomodel dealing with the atomistic and the molecular levels. In particular this hypomodel comprises a structural atomistic hypo-hypomodel, a molecular association hypo-hypomodel and a molecular network hypo-hypomodel. A future refinement of the molecular network hypo-hypomodel focusing on metabolism is to be made by FORTH. The crucial parameter of cell kill rate that is meaningful for both the subcellular and the cellular levels of biocomplexity has been used as the linking point of the subcellular with the the cellular and supercellular world. In fact atomistic and molecular modeling lead to the patient individualization of this central hypermodelling parameter. In parallel with this complex and detailed multiscale hypermodel, UNITO has produced a number of gross hypomodels based on simplified universal growth laws. Their purpose is to provide an initial very gross but still useful check of the overall behaviour of the multimodeller hypermodel. Conversely, the detailed multiscale multimodeller hypermodel is to serve as a possible corrector of the UNITO gross set of hypomodels. Master topologies for the other two multimodeller hypermodel demonstrators concerning the nephroblastoma (Wilms) and glioblastoma multiforme scenarios are under refinement. Their gross initial outlines are provided in sections W and G of this document.

T. The (Pure) Tumour Growth and Response to Treatment Component Model

T1. Introduction

A core scientific question is how to exploit the cumulative data from experimental and clinical observations towards the design of personalized medicine [Graf & Hoppe, 2006]. Simulation models of cancer dynamics constitute an imperative tool towards this direction. The mathematical modeling of tumour growth and response to treatment could serve as a powerful tool for studying cancer in a more systematic way, can help to better comprehend the underlying biological processes, verify or discard assumptions about the natural mechanisms involved, guide the next research steps and answer questions of clinical importance.

In the present chapter, a clinically-oriented, multiscale, spatiotemporal simulation model of solid tumour free growth and response to therapy has been presented and investigated. The model core stems from previous work of the *In Silico* Oncology and *In Silico* Medicine Group, ICCS, National Technical University of Athens. The model addresses tumours well beyond their initiation phase and aims at simulating their spatiotemporal evolution. It has been designed to incorporate patient-specific data such as imaging-based, histopathological, molecular and treatment data.

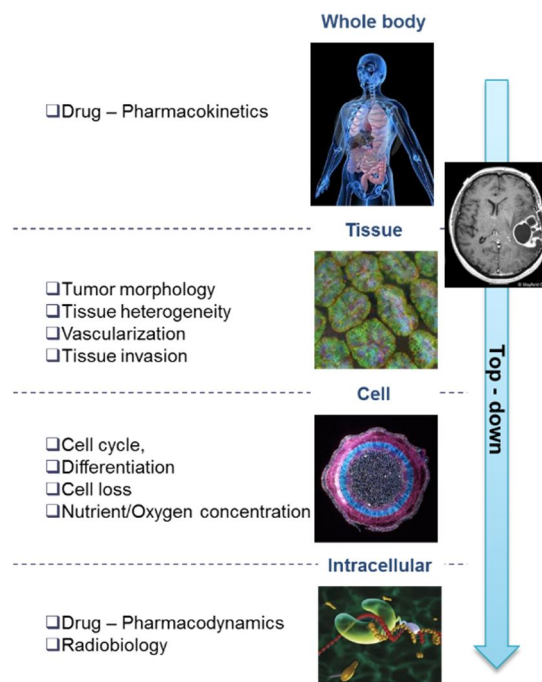


Fig. T1 The multiscale nature of the modelling approach

Prior to an eventual use in the clinical context, any clinically-oriented simulation model must undergo a thorough adaptation, validation and optimization procedure. The first step would be an exhaustive examination of model behaviour with respect to the variation of its input parameters. Such a study is essential for model parameters' adaptation and plausible value range identification, in order to guarantee a biologically relevant virtual tumour behaviour. Furthermore, aspects of the interplay and possible interdependencies of the biological mechanisms modeled, which often cannot be grasped intuitively, can be enlightened and biological experimental observations can be deciphered. A number of parametric studies have been performed in order to study the model's behaviour in relation to the value of each chosen input parameter with the primary aim to deepen and advance quantification of our understanding of tumour response to chemotherapeutic treatment.

T2 Model Description

T2.1 The Cytokinetic Model - Biological Processes Considered

Tumours usually consist of a cluster of heterogeneous cell populations with variable proliferative potential. Experimental observations have indicated that tumour sustenance is attributed to the so-called cancer stem cells [Bjerkvig *et al.*, 2005; Sell 2004; Gupta *et al.*, 2009; Visvader, & Lindeman, 2008], a cell population exhibiting stem cell-like properties, such as unlimited self-renewal and differentiation capacity. Moreover, tumours, not only among different but also within the same tumour type, are characterized by variable differentiated cell composition. The model takes into account cells of distinct mitotic potential and supports the simulation of tumours of different differentiation degree as reflected in the relative percentage of proliferating and differentiated cells.

The adopted cytokinetic model (Fig. T2) incorporates the biological mechanisms of cell cycling, quiescence, recruitment, differentiation and loss via apoptosis (either spontaneous or treatment-induced) and necrosis (starvation-induced) [Stamatakis *et al.*, 2002, 2010, 2011, 2014, Dionysiou *et al.*, 2004, Stamatakis 2011]. Tumour sustenance is attributed to the presence of the cancer stem cells, which have the ability to preserve their own population. Two types of stem cell division are possible: symmetric and asymmetric. An asymmetric stem cell division gives rise to one daughter cell with stem cell fate and one daughter cell (limited mitotic potential or committed progenitor cell) that follows the path towards differentiation. A symmetric stem cell division gives rise to two daughter cells both with a stem cell fate. Specifically, the following five categories of cancer cells are considered in the model:

- i. Stem cells: cells able to perform unlimited number of divisions
- ii. Limited mitotic potential (LIMP) or restricted/committed progenitor cells: cells able to perform a limited number of divisions before becoming terminally differentiated
- iii. Differentiated cells: terminally differentiated cells with no mitotic capacity
- iv. Apoptotic cells: cells that have died through apoptosis
- v. Necrotic cells: cells that have died through necrosis

Stem, LIMP and differentiated cells constitute three categories with distinct mitotic potential.

Proliferating tumour cells (stem or LIMP) go through the four phases of the cell cycle: gap 1 (G1) phase, DNA synthesis (S) phase, gap 2 (G2) phase and mitosis (M) phase. After the completion of mitosis, a fraction of newborn cells will enter the dormant phase, due to insufficient nutrient supply and oxygenation, whereas the rest will continue to cycle. Under conditions of lack of nutrients, dormant cells are assumed to survive only for a limited time length. After the expiration of this time,

dormant cells die through necrosis, unless the local conditions of nutrient and oxygen supply have been reinstated, allowing the re-entering of the dormant cell into the active cell cycle. Any cell may die through spontaneous apoptosis. Differentiated cells may die through apoptosis or necrosis. Table T-1 lists the model parameters and the corresponding biological mechanisms as described above.

When a tumour is chemotherapeutically treated, a fraction of cancer cells are lethally hit by the drug or its metabolites. Lethally hit cycling tumour cells enter a rudimentary cell cycle that leads to apoptotic death via a specific phase dictated by the action mechanism of the chemotherapeutic agent used. Similarly, in the case of cell cycle non-specific drugs, lethally hit dormant (G0) cells enter the G0hit phase. Marking of a cell as *hit* by the drug is assumed to take place at the instant of drug administration although its actual time of death is dictated by the specific pharmacokinetics and pharmacodynamics of the drug. It is pointed out however that cell cycle phase specific drugs can be readily modeled by the cytokinetic model shown in Fig. T2 by appropriately selecting the “Chemo” induced exit from the normal cell cycle for both cases of stem and LIMP cells.

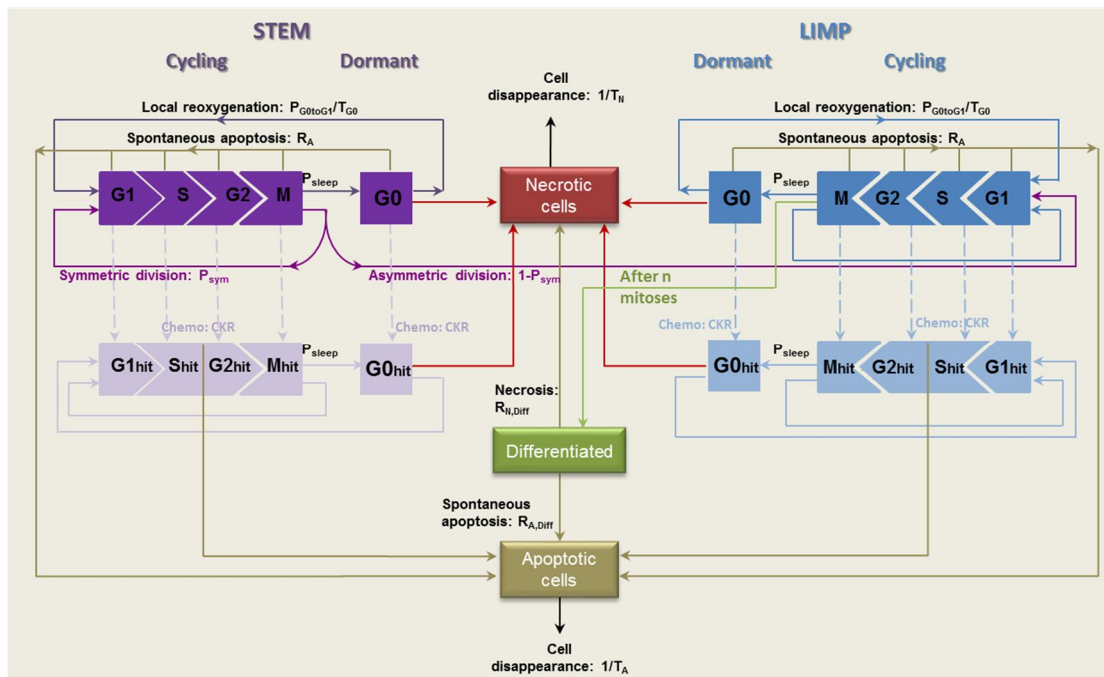


Fig. T2: Generic cytokinetic model (cell category / phase transition diagram) for tumour response to chemotherapy. Abbreviations: STEM: stem cell. LIMP: Limited Mitotic Potential tumour cell (also called committed or restricted progenitor cell). DIFF: terminally DIFFerentiated tumour cell. G1: Gap 1 cell cycle phase. S: DNA synthesis phase. G2: Gap 2 phase. M: Mitosis phase. G0: dormant, resting phase. Chemo: chemotherapeutic treatment. Hit: cells lethally hit by the drug.

TABLE T-I. CODE INPUT PARAMETERS

Parameter symbol	Description	Units	Value range
CELL PHASE DURATIONS			
$T_c[\text{class}^*]$	Cell cycle duration	hours	-
$T_{G0}[\text{class}^*]$	G0 (dormant phase) duration i.e. time interval before a dormant cell enters necrosis	hours	-
$T_N[\text{region}\ddagger]$	Time needed for both necrosis to be completed and its lysis products to be removed from the tumour	hours	-
$T_A[\text{region}\ddagger]$	Time needed for both apoptosis to be completed and its products to be removed from the tumour	hours	-
CELL CATEGORY/PHASE TRANSITION RATES AND FRACTIONS			
R_A	Apoptosis rate of living stem and LIMP tumour cells (fraction of cells dying through apoptosis per unit time)	hours ⁻¹	0-1
R_{NDiff}	Necrosis rate of differentiated tumour cells	hours ⁻¹	0-1
R_{ADiff}	Apoptosis rate of differentiated tumour cells	hours ⁻¹	0-1
$P_{G0toG1}[\text{class}^*][\text{region}\ddagger]$	Fraction of dormant (stem and LIMP) cells that re-enter cell cycle	-	0-1
$P_{sleep}[\text{region}\ddagger]$	Fraction of cells entering the G0 phase following mitosis	-	0-1
$P_{sym}[\text{region}\ddagger]$	Fraction of stem cells that perform symmetric division	-	0-1
MISCELLANEOUS PARAMETERS			
Cell density	Number of biological cells normally contained within a unit volume	mm ⁻³	10 ⁶
Voxel dimension	Dimension of voxel/GC edge	mm	1 or 2, depends on tumour size and computing resources
N_{LIMP}	Number of mitoses performed by LIMP cells before becoming differentiated	-	≥1
$x_{dim}, y_{dim}, z_{dim}$	Number of geometrical cells along the x, y, z axis respectively	-	depends on tumour size and computing resources
tumour_length tumour_breadth tumour_width	Dimensions of the three tumour axes in mm in the case a triaxial ellipsoidal tumour is considered	-	depends on tumour imageable characteristics
necrotic_length necrotic_breadth necrotic_width	Dimensions of the necrotic region along the three axes in GCs in case a triaxial ellipsoidal tumour is considered	-	depends on tumour imageable characteristics
Execution time	Execution stop time after initialization	days	-
Spatial evolution?	Will geometric spatial evolution be included in the simulations? "True": yes. The functions for tumour differential expansion/shrinkage are enabled "False": no. The functions for tumour differential	-	0 or 1

margin_percent	expansion/shrinkage are disabled Acceptable temporary over-loading or under-loading of each geometrical cell as a fraction of unity	-	0.0 - 0.5
color_criterion	Minimum percentage of tumour cells that should be dead in order to denote ("paint") the corresponding geometrical cell as necrotic	-	0.9 - 0.999
Input image?	true: consider the input image file false: no input image file	-	0 or 1
Image filename	Name of the input image file	-	-
Output directory	Name of the directory where the output files are stored	-	-
mode	The tumour course to be simulated	-	1: Free growth, 2: treatment response
CHEMOTHERAPY PARAMETERS			
$D_{\text{chemo}}[\text{drug}\dagger]$	Drug dose	mg m ⁻²	depends on clinical data
$T_{\text{chemo, adm}}[n][\text{drug}\dagger]$	Time point of nth drug administration, n=1,...	days	depends on clinical data
Cell kill rate[drug†]	The numbers of biological cells lethally hit by the drug at each administration	-	0-1
Distance_factor[region‡]	Factor adapting the cell killing probability as estimated by pharmacodynamics to each tumour region	-	0-1
Cell kill factor [class*]	Factor adapting cell killing probability to stem or LIMP cells	-	0-1
*Defined separately for stem and LIMP cells (class: {stem, LIMP})			
‡Defined separately for proliferating and necrotic region (region: {proliferating, necrotic})			
†Defined separately for each drug administrated			

T2.2 Model Implementation Choices - Basic Notions

Model implementation is based on the consideration of a discrete time and space stochastic cellular automaton, representing the tumour region. More specifically, a three dimensional (3-D) cubic discretizing mesh is superimposed upon the anatomical region of interest. The elementary cube of the mesh is called geometrical cell (GC). The size of the GC can be defined by the user. Typical values considered are 1x1x1 or 2x2x2 mm³. The exact choice depends on tumour size and available computational resources. Each GC occupied by the tumour corresponds to a cluster of heterogeneous cells found in various states. More specifically, the biological cells residing within each occupied GC are distributed into the five categories mentioned above i.e. the stem, LIMP, differentiated, apoptotic and necrotic categories. From the mathematical standpoint each cell category defines an equivalence class. Distribution of the cells into the five equivalence classes creates one level of biological cell population partitioning within each GC. At each given instant each stem or LIMP cell can be either proliferating or dormant. Proliferation or dormancy creates another level of cell population partitioning. Cell cycle phases (G1, S, G2, M) introduce a finer partitioning of proliferating cells (stem and LIMP) into subclasses. A further partitioner in the case of therapeutic intervention is treatment hitting i.e. a boolean variable denoting whether a biological cell has been hit by treatment. Each occupied GC is assumed to initially contain a fixed *Number of Biological Cells* (NBC). This number is based primarily on observations available in pertinent literature, e.g. 10⁶ biological cells/mm³ [Steel, 1997, p.9], unless more specific data are available. The cytokinetic model

regulates the transitions between the various cell states, whereas adequately shaped morphological rules are introduced in order to regulate the cell movement throughout the tumour volume, as described in the following sections.

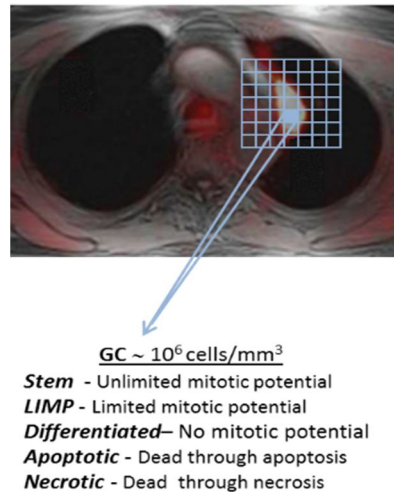


Fig. T3: Discretizing mesh and the concept of Geometrical Cell (GC)

Time is discretized. The time unit is taken one hour which is approximately the duration of mitosis, the shortest cell cycle phase [Bast *et al.*, 2000]. For any given instant the biological cells belonging to the same cell category and cell cycle phase within a given GC are assumed synchronized. However, biological cells belonging to different GCs or to different categories and cell cycle phases within the same GC are not assumed synchronized. From the computational standpoint a sufficient number of registers are used to describe the state of each GC occupied by the tumour. They include i.a. the number of biological cells residing in each equivalence class and subclass and the time spent at each subclass.

The duration of mitosis phase is considered constant and equal to 1h [Bast *et al.*, 2000]. The rest of the cell cycle phases durations are computed based on Salmon *et al.* (2001), after having taken into consideration the above assumption regarding the constant duration of mitosis. More specifically the following equations are used: $TG1 = TS = 0.41(Tc-TM)$, $TG2 = 0.18(Tc-TM)$, $TM = 1h$.

The simulation code has been implemented in C++.

T2.3 Simulation Procedure

A detailed flowchart of the simulation algorithm is depicted in Fig. T4. The major steps involved are described below.

STEP 0: Tumour Definition

The model supports the simulation of three-dimensional tumours of arbitrary shape, as well as the division of tumour area into regions of different metabolic activity (e.g. necrotic and proliferative). Mesh initialization involves the definition of occupied and non occupied GCs, based on the available patient-specific imaging data. Occupied GCs (i.e. GCs that belong to the tumour region) can be

further subdivided into necrotic or proliferative, provided that the relevant info has been foreseen in the segmented tumour images. The values assigned to the model input parameters can be defined for each type of GC in relation to the considered metabolic subregions. Patient specific data such as histological data (e.g. type, stage and differentiation grade) and molecular data, as well as other tumour specific data, can be incorporated for further refinement of the values attributed to the model input parameters. In case of macroscopically homogeneous tumours, all occupied GCs are characterized by identical values. It should be noted that in the absence of 3D imaging data the tumour shape is approximated with a triaxial ellipsoid. The length of the axes of the ellipsoid are assumed equal to the maximum tumour diameter(s) as measured based on e.g. ultrasound examination.

STEP 1: Free Growth Check

Based on the cytokinetic model described previously, stem cells are responsible for sustaining the cancer and their behaviour plays a determinant role for cancer free growth evolution. Depending on the values assigned to the model parameters that describe the life course of stem cells, it is possible to simulate cancer with variable degree of aggressiveness in terms of growth rate. Furthermore, there exist certain ‘forbidden’ value combinations of these parameters that lead to biologically irrelevant cancers, i.e. cancers that diminish over time of their own accord, unable to sustain growth.

A condition is applied to check whether the value combination of input parameters leads to a growing or self-diminishing cancer. The condition has been derived [Kolokotroni *et al.*, 2011] from an analytical treatment of model assumptions following the methodology of Bertuzzi *et al.* (1997).

$$\left(1 + P_{sym}\right) \left(1 - P_{sleep} + P_{sleep} \frac{P_{G0toG1}/T_{G0}}{R_A + 1/T_{G0}}\right) e^{-R_A T_c} \geq 1$$

In order to take into account any divergence between the simulating results and the above condition we assume that for values of the left side of the above inequality lower than 0.9 cancer free growth cannot be sustained, whereas for values above 1.1 free growth is ensured. In the middle value range the cancer free growth is checked based on simulation results during the tumourigenesis process.

STEP 2: Tumourigenesis (Creation of the Tumour at Baseline)

The technique applied for the determination of tumour’s cell composition is critical, so as to avoid latent artificial tumour growth behaviours. A decrease in tumour volume followed by a volume increase is a very common pattern [Kolokotroni *et al.*, 2008]. In order to avoid an abnormal free growth behaviour at the beginning of the simulation, the automatic tumour initialization methodology has been developed [Stamatakis *et al.*, 2010], according to which the initial relative population (expressed as a fraction of the total tumour cell population) of each equivalence class and its equivalence subclasses is adjusted to the values attributed to the cell category and cell phase transition rates. The principle of the technique is to start with a small number of stem cells and with specific cell category transition rates that are assumed to hold true for a relatively small time interval about the treatment baseline. The phase durations and transition rates acting as input parameters to the model are defined. Gradually, all cell categories and phases become populated and after sufficient time the relative cell categories populations tend to reach an equilibrium state. If in subsequent simulations the GCs are initialized using the cell category /phase relative population

values corresponding to this equilibrium state, a mathematically monotonous and biologically normal free growth behaviour will be achieved.

STEP 3: Population Initialization

The biological cells residing within each geometrical cell of the mesh are distributed into the five cell categories (i.e. stem, LIMP, differentiated, apoptotic, necrotic), based on the fractions calculated during the previous step. The initial distribution of the proliferating cells throughout the cell cycle phases (G1, S, G2, M) is assumed proportional to the corresponding cell cycle phases durations. The mean time spent by the biological cells of a given equivalence subclass in the same subclass is initialized using a random number generator (Monte Carlo technique). The time under consideration can vary between 0 and the maximum time of the corresponding phase. As mentioned above biological cells belonging to different GCs or to different categories and cell cycle phases within the same GC are not assumed synchronized.

At each time step i.e. every hour the discretizing mesh covering the anatomical region of interest is virtually scanned in order to apply the basic metabolic, cytokinetic, pharmacokinetic / pharmacodynamic and mechanical rules that govern the spatiotemporal evolution of the tumour system. For practical reasons each complete virtual scan can be viewed as consisting of two mesh scans.

STEP 4: First Mesh Scan

The first scan aims at updating the state of each GC according to the proposed and adopted cytokinetic model of Fig. T2. The time registers of the various cell subclasses within each geometrical cell are updated and the cytokinetic diagram is applied within each GC as follows. Spontaneous apoptosis induced cell loss from each non treatment perturbed cell cycle phase and the G0 phase is calculated for each cell category based on the spontaneous apoptotic rates assumed. Any necessary transitions between equivalence subclasses ($G1 \rightarrow S$, $S \rightarrow G2$, $G2 \rightarrow M$, $M \rightarrow G1$ or $M \rightarrow G0$) take place for biological cells clustered in the same subclass. The latter depends on the updated value of the corresponding time registers. If the mean time that the clustered cells have spent in the corresponding phase has become equal to or larger than the phase duration, then the cells enter a new phase and equivalence subclass.

In any one of the cases of dormant (including stem and LIMP), differentiated, necrotic and apoptotic cells a fraction of the corresponding subclass(es) population may be transferred to another subclass or disappear from the tumour at each time step according to the cytokinetic model (Fig. T2). Therefore the following transitions may take place. For stem and LIMP cells: $G0 \rightarrow G1$ or $G0 \rightarrow \text{Necrosis}$ or $G0 \rightarrow \text{Apoptosis}$. For differentiated cells: $\text{Differentiated} \rightarrow \text{Necrosis}$ or $\text{Differentiated} \rightarrow \text{Apoptosis}$. For dead cells of any mitotic potential category: $\text{Apoptosis} \rightarrow \text{Cell disappearance}$, $\text{Necrosis} \rightarrow \text{Cell disappearance}$. Most of the corresponding rates are parameters of the model (Table T-I).

As far as chemotherapy is concerned, at any time instant corresponding to drug administration, the numbers of proliferating and dormant cells belonging to each one of the phases G1, S, G2, M or G0 and to each one of the stem or LIMP mitotic potential categories that are designated as hit by the drug are computed. The latter is achieved through the utilization of the cell kill ratio (CKR) parameter that corresponds to the drug and dose (per m^2 of the patient surface) considered. In terms of the

simulation model's parameters the cell kill ratio is the percentage of LIMP and stem cells hit by the chemotherapeutic agent after each drug administration. The above mentioned cell numbers are added to the corresponding cell numbers of the drug affected equivalence subclasses, designated as "phase" hit e.g. G1hit in the cytokinetic diagram of Fig. T2.

STEP 5: Second Mesh Scan

The second scan aims at simulating tumour expansion or shrinkage, while preserving a roughly uniform cell density throughout the tumour volume. To this end, adequately shaped morphological rules are introduced, which may lead to tumour expansion, as is the case in free tumour growth, or no change in tumour volume or tumour shrinkage as is usually the case after treatment administration. The adopted morphological rules [Dionysiou *et al.*, 2004, 2006] aim at preserving the cohesion and initial shape figure of the tumour under the assumption that the mechanical properties of the surrounding normal tissues are invariant throughout the simulation, while preventing the tumour to acquire an artificial shape. During the above process artificial tumour fragmentation may, however, occur and a special procedure has been devised in order to achieve macroscopic tumour cohesion [Giatili *et al.*, 2008]. The latter usually characterizes tumour shrinkage following treatment.

For practical reasons at any given time point the total cell population that can be accommodated in each GC is allowed to fluctuate between a minimum ($0.9 \cdot \text{NBC}$) and a maximum ($1.1 \cdot \text{NBC}$) value. If the total population exceeds the maximum value of $1.1 \cdot \text{NBC}$ then a procedure is initiated that attempts to unload the total GC population minus NBC to neighbouring GCs (26 GC neighbourhood is considered) possessing empty space i.e. GCs with total cell population less than NBC. The procedure starts from the neighbouring GC possessing the maximum free space. If two or more neighbouring GCs possess the same free space then a random number generator is used so as to select the visiting order of the GCs. The procedure is repeated until all the excess cells have been transferred, provided this is possible. If the procedure fails to reduce the total population of the GC under consideration below the upper limit (maximum value) then an adjacent GC is freed from its contents which are moved outwards. The latter push the contents of a chain of geometrical cells outwards too. The excess contents of the GC under consideration are placed into the newly freed adjacent GC. The previous process leads to differential tumour expansion. The position of the GC to be freed from its contents relative to the GC with the excess contents is determined using a random number generator. The shifting of the chain of GCs mentioned above can take place along any randomly selected direction. The direction is selected based on a random number generator.

On the other hand if the GCs total cell population is below the minimum value then a similar procedure attempts to unload all cells to neighbouring GCs possessing free space. If the GC becomes empty, then a chain of GC contents is shifted towards the GC under consideration so as to fill the vacuum generated. The latter leads to differential tumour shrinkage. Shifting of the GC content chain takes place as follows. Six lines of random direction are chosen based on a random number generator. The outermost non-empty GC along each one of these directions is detected and its "6-Neighbour" GCs belonging to the Tumour (NGCT) are counted. The direction corresponding to the maximum NGCT is selected.

The above procedure, however, may give rise to the following "side effects". (a) Tumour fragmentation: some GCs belonging to the tumour become separated from the main tumour mass. (b) Vacuum enclosures: holes that correspond to empty GCs are created inside the tumour. In order to avoid the occurrence of the above side effects an algorithm has been developed that: (I) detects tumour occupied GCs that are surrounded by empty GCs in a "6-GCs Neighbourhood" and moves

their contents (by one GC at each time step) towards the tumour's center of mass. The direction of movement is chosen based on the minimum distance of the GC under consideration from the center of mass along the x, y, z coordinates. The corresponding quantity to be calculated each time is the following:

$$\min\{\text{abs}(\text{GC.x-center.x}), \text{abs}(\text{GC.y-center.y}), \text{abs}(\text{GC.z-center.z})\}$$

where $\text{abs}()$ denotes absolute value, GC.x, GC.y and GC.z are the x, y and z coordinates of the GC respectively and center.x, center.y and center.z are the x, y and z coordinates of the tumour's center of mass respectively. If more than one direction is characterized by the same minimum distance then a random number generator is used for the selection of the movement direction. (II) detects empty GCs that are surrounded by occupied GCs in a "6-GCs Neighbourhood" and fills them with the contents of adjacent GCs by applying the tumour shrinkage procedure described above.

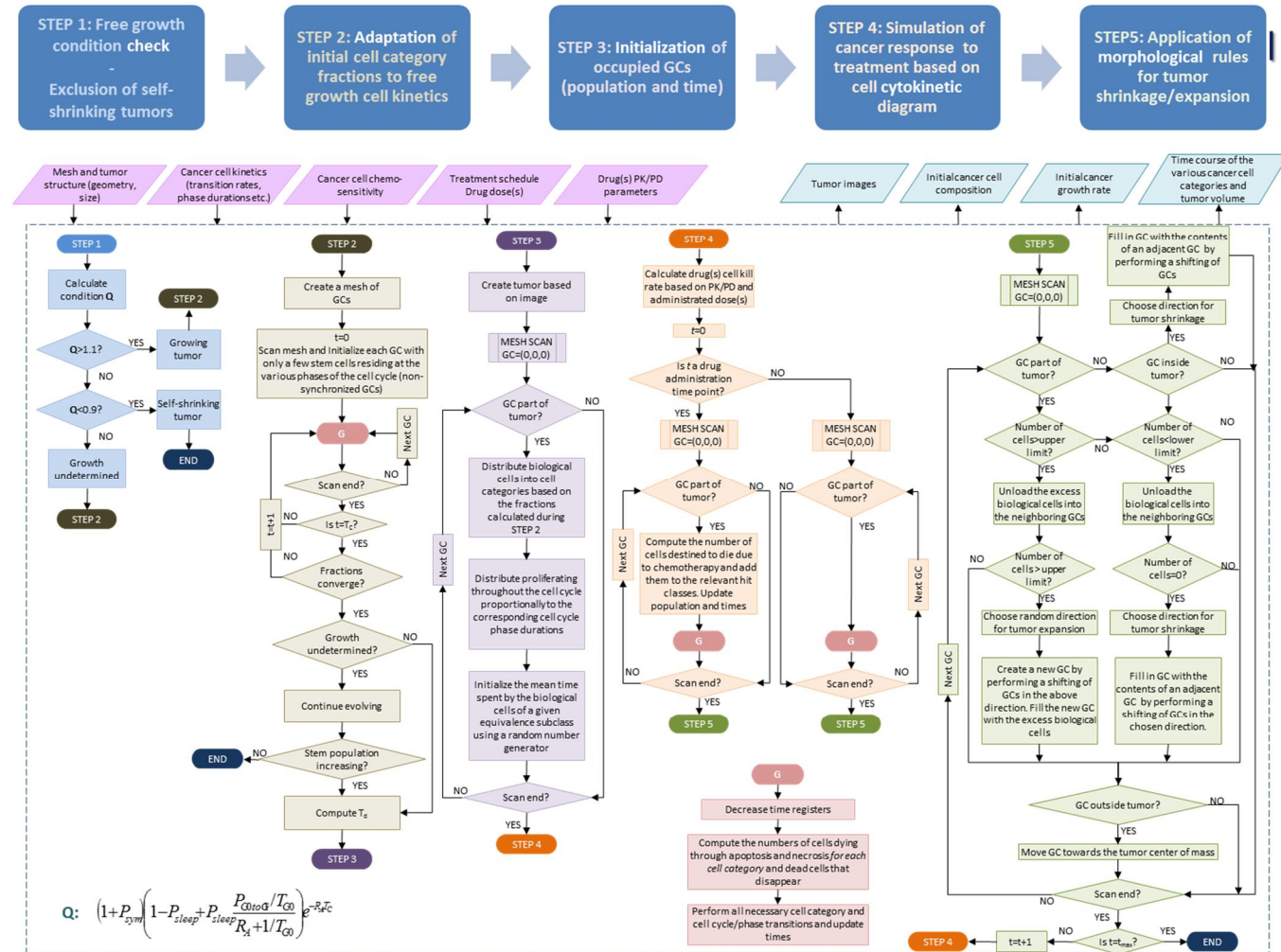


Fig. T4: Flow chart of the simulation procedure for a macroscopically homogeneous solid tumour of arbitrary shape. Abbreviations: GC: geometrical cell. NBC: Number of Biological Cells normally contained within a geometrical cell of the mesh, t : simulation time step.

T2.4 Code Input Arguments and Output Files

The code accepts as input argument an XML file that contains the values (element <value>) to be assigned to the model input parameters. The XML file also includes a description of each parameter accompanied by the applicable value range, the considered units and the default values. If no input argument is passed, then the code is executed using some default values.

The *core output of the simulation code* is a number of matrices corresponding to the discretization mesh of the anatomic region of interest for a series of time points. These matrices contain all the necessary biological information to be used for the 3D metabolic, kinetic etc. reconstruction of the tumour at several time points or the production of several diagrams describing tumour dynamics and response to therapy as a function of space and/or time.

More specifically, the current version of the code can give as an output:

1. *tumour_evolution.dat*: A dat file containing the time evolution of the various total cell categories populations that comprise the tumour as well as its volume in mm³, and the number of occupied GCs for each time step. The cell categories classes reported are stem proliferating, stem G0, stem proliferating hit by chemotherapy, stem G0 hit by chemotherapy, LIMP proliferating, LIMP G0, LIMP proliferating hit by chemotherapy, LIMP G0 hit by chemotherapy, differentiated, apoptotic, necrotic, stem (proliferating + G0), LIMP (proliferating + G0), proliferating (stem + LIMP), G0 (stem + LIMP), living, hit (chemotherapy), dead and total.
2. *initial_tumour.dat*: A dat file listing the three coordinates (x, y, z) at the mesh coordinate system of each occupied GC belonging to the initial tumour at time step 0, that can be used for the 3D presentation of the initial tumour and its total cell population.
3. *final_tumour.dat*: A dat file listing the three coordinates (x, y, z) at the mesh coordinate system of each occupied GC belonging to the final tumour, that can be used for the 3D presentation of the final tumour and its total cell population.
4. *oncosim-parameters.log*: A log file containing the values assigned to the model input parameters.
5. *tumour_dynamics.dat*: A dat file containing free growth dynamic characteristics of the simulated tumour i.e. the volume doubling time and the relative population of the various cell categories per metabolic region, e.g. proliferating and necrotic (if any).
6. *final_tumour.raw*: A raw file containing horizontal cutting planes of the final tumour that can be used for the 3D representation of the tumour. Only occupied GCs (GCs belonging to the tumour) and GCs representing normal tissue are considered.
7. *output.xml*: An XML file containing the path of the above files and the relative reduction of the tumour volume based on the simulation predictions (*100% of the original volume) : (Initial tumour volume – Final tumour volume)/ Initial tumour volume

The adaptation of model's input/output format and method of parsing model parameters is foreseen based on the guidelines of WP7 in order to facilitate the communication of the current model with other component models as a part of the generic CHIC lung specific hypermodel.



T3. Parametric Investigation of the Model

Any model must initially undergo an in-depth parametric investigation, for a number of reasons, including: detecting biologically irrelevant virtual tumour behaviour, narrowing the acceptable value range of the model parameters, correlating these parameters with kinetic and other quantities reported in literature (e.g. doubling time, growth fraction, differentiation grade etc.) and determining the sensitivity or robustness of the output in relation to uncertainties in the input data. Only then can an efficient methodology for the adaptation of model input parameters to patient and tumour specific data be defined and the credibility of the model results be increased.

In this section, the results of several parametric studies of the simulation model are presented. The impact of the model parameters given in Table T-I on tumour's growth rate and cell population composition and treatment induced tumour regression has been investigated.

T3.1 Untreated Tumour Growth and Chemotherapeutic Response Curve Patterns

Tumour growth is a complex phenomenon involving the interplay of various underlying biological mechanisms. This is reflected in the great diversity of growth patterns reported in literature. This diversity involves not only the shape of the time course of tumour volume, but also the observed growth rate. A number of experimental or clinical tumour data are successfully described by the simple cases of exponential and Gompertzian functions, however the need for more complex growth patterns is evident in other cases [Retsky *et al.*, 1990; Chignola *et al.*, 2000]. The model is characterized by the potential to simulate a wide range of experimental/clinical tumour data sets by properly adjusting the model input parameters. Most importantly, the model parameters are not arbitrarily defined, but are related to specific biological mechanisms, such as cell proliferation, quiescence, differentiation and loss, thereby enabling the independent handling and study of each of the above phenomena.

The model supports the division of tumour volume into regions of distinct metabolic activity (i.e. necrotic, and proliferative). However, in the absence of relevant info in the segmented tumour images, only a single proliferative region is considered. This implies that microscopic necrotic regions, primarily due to imperfect neovascularization of the tumour, are postulated rather homogeneously distributed over the entire tumour. In the case of tumours with macroscopically distinct tumour subregions, an equivalent tumour of the same constitution, in terms of cell categories population numbers, is being considered. The above treatment implies that the values assigned to the various tumour dynamics parameters (such as cell category transition rates) are assumed to reflect mean values over the entire tumour mass. Moreover, spatial metabolic homogeneity is a characteristic feature of tumours at the beginning of their avascular growth phase prior to the formation of a necrotic core.

Furthermore, in our modelling approach the cell category transition rates are assumed constant during the simulation duration. Such an approximation is considered applicable for a relatively short time interval compared to the tumour's lifetime (for example, during a chemotherapeutic treatment course) and the constant values are assumed to reflect the means of the actual cell category transition rates over the interval. The use of mean values in several tumour dynamics parameters over a substantial time interval is quite customary in radiobiology [Begg, 1997].

Finally, the model aims at simulating fully developed, clinical tumours, well beyond their initiation phase. For such a biological system it is rational to assume that a state of population equilibrium and of balanced growth has been achieved. A tumour is in a state of population equilibrium (or balanced growth) when each cell category population as a proportion of the total cell population tends to a limit, even though the total population increases. The proper initialization of tumour cell populations [Stamatakis *et al.*, 2010; Kolokotroni *et al.*, 2011] ensures conditions of balanced growth from the beginning of the simulation.

A tumour characterized by space and time independent growth kinetics parameters and population equilibrium would demonstrate a grossly exponential growth pattern [Kolokotroni *et al.* 2011]. Even though it is generally accepted [Steel, 2002] that tumours grow in a Gompertzian manner during their lifetime (i.e. the growth progressively slows as the tumour enlarges), a number of lung cancer cases reported in literature exhibit fairly constant growth rates on the logarithmic scale [Geddes 1979; Quint *et al.*, 2008; Friberg and Mattson 1997; Mackintosh *et al.*, 2014] over prolonged periods of time (ranging from months to years). It has been argued that these tumours were probably still in the exponential phase of Gompertzian curve at the time of diagnosis and clinical surveillance [Quint *et al.*, 2008].

Fig. T5 and Fig. T6 show the simulated time course of a macroscopically homogeneous tumour under free growth and treatment conditions respectively. In the case of treatment a typical scheme for non small cell lung cancer has been assumed that is based on the combination of two chemo drugs i.e. cisplatin and gemcitabine. The doublet regimen is administrated three times as a three-week cycle. On the first day of treatment cycle the patient is given both the gemcitabine and cisplatin. On the same day of the following week (day eight) only Gemcitabine is administrated. Qualitatively a fairly expected and reasonable tumour dynamics behaviour can be easily noticed. An exponential pattern of growth in the absence of treatment and tumour regression followed by repopulation after each chemotherapeutic session in the case of treatment are successfully demonstrated.

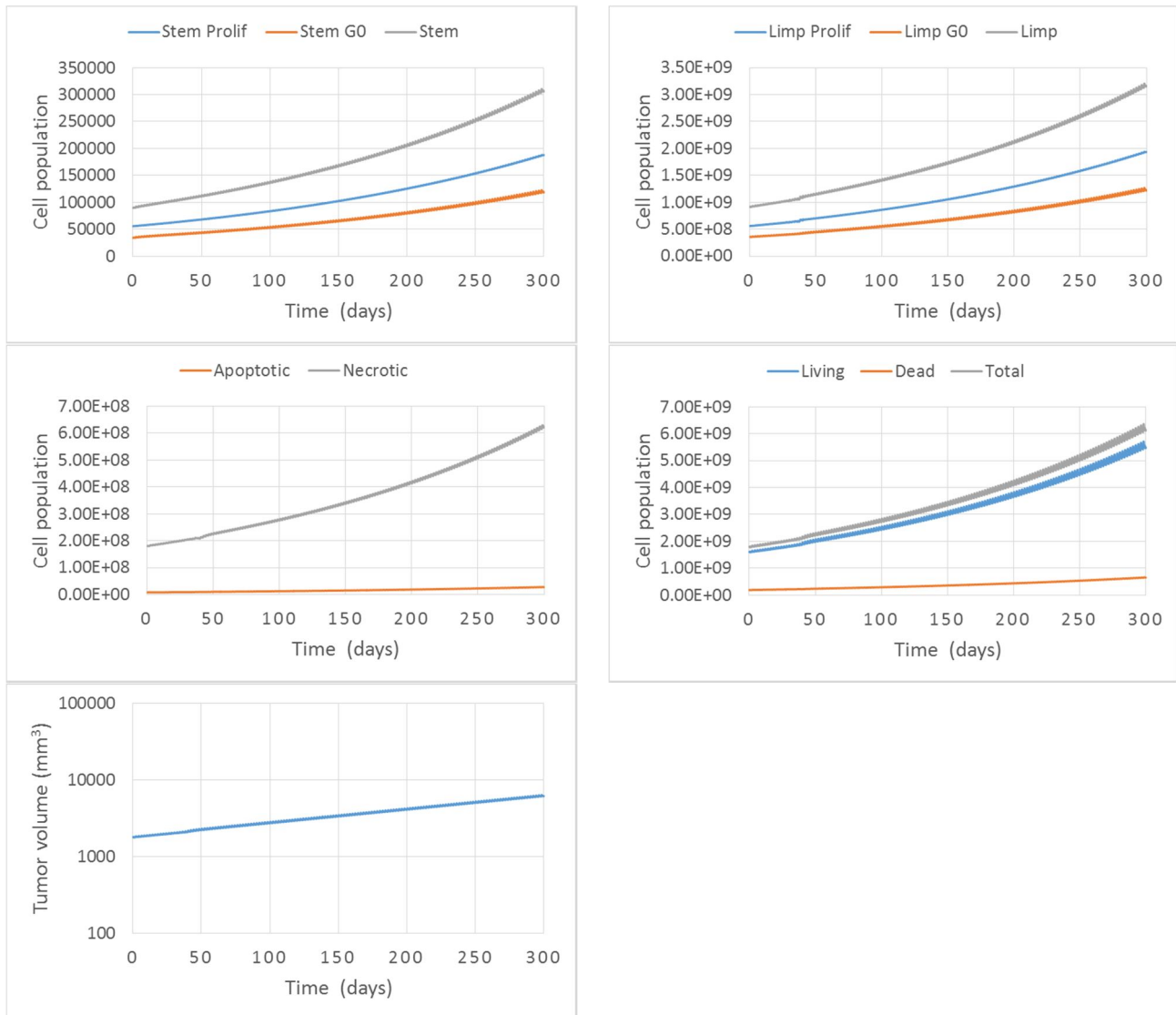


Fig. T5: Various tumour cell populations as a function of time in the case of untreated tumour growth simulation. A homogeneous spherical tumour of 15mm diameter is considered. The values of code input parameters that regulate tumour growth dynamics are given in Table T-X.

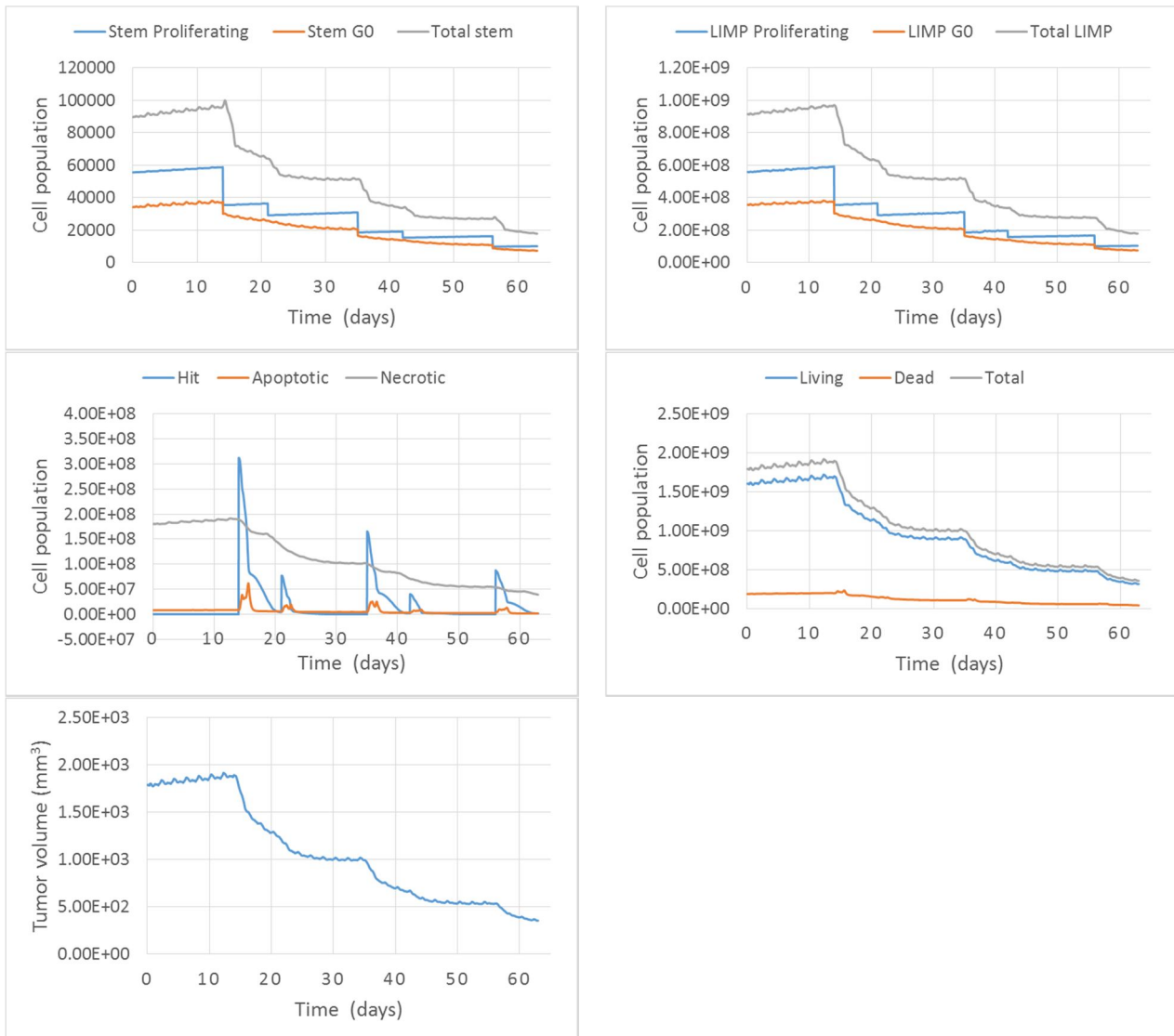


Fig. T6: Various tumour cell populations as a function of time in the case of treatment response simulation. A homogeneous spherical tumour of 15mm diameter is considered. A cell cycle specific (gemcitabine) and a cell cycle non-specific (cisplatin) drug are administrated as a three-week cycle. Gemcitabine is given on days 14, 21, 35, 42, 56 and 63. The effect of gemcitabine on proliferating cells is evident from the sudden drop in their population. Cisplatin is administrated on days 14, 35 and 56. Cisplatin affects both proliferating and G0 cells. The values of code input parameters that regulate tumour dynamics are given in Table T-X.

T3.2 OFAT Analysis

In the case of untreated tumour growth, the effect of the model parameters on the tumour doubling time, the growth fraction, and the various cell category relative populations, has been thoroughly studied in [Kolokotroni *et al.*, 2011]. Here the main conclusions are summarized.

In the case of treatment, the effect of the model parameters on treatment response is investigated. Plots by varying one input parameter, while keeping the others at a baseline value have been produced (one factor at a time –OFAT- analysis). The method has been applied for all model input parameters that regulate tumour dynamics (Table T-I). The output measure considered has been the overall tumour shrinkage on day 63 from simulation onset. The therapeutic scheme considered is the same as above. A macroscopically homogeneous tumour has been assumed.

T3.2.1 Tumour Doubling Time

For a macroscopically homogeneous tumour under balanced exponential growth, the doubling time is affected only by the parameters that describe the cytokinetic behaviour of stem cells, i.e. the cell category that sustains the tumour. Parameters related to LIMP, differentiated or dead cells appear to have no effect on the growth rate of the tumour. More explicitly, doubling time is regulated by the following parameters [Kolokotroni *et al.*, 2011]:

Cell cycle duration (T_C). In accordance with literature low values of T_C are associated with rapidly evolving tumours. A short cell cycle implies that more mitotic divisions are performed within the same time interval, resulting in a tumour that grows faster and hence is characterized by a short doubling time.

Symmetric division fraction (P_{sym}). For high values of P_{sym} , the simulated tumour is characterized by a short doubling time of a few days, implying a rather aggressive tumour. Higher values of P_{sym} are associated with more stem cells being born after each mitotic event, thereby resulting in an increased stem cell birth rate and faster growing tumours.

Fraction of newborn cells entering G0 phase (P_{sleep}). Low values of P_{sleep} are associated with short doubling times. This parameter is related to the loss of stem cells due to starvation. When P_{sleep} increases, more stem cells enter the G0 phase after completion of mitosis and follow the path to necrosis. Hence, fewer newborn cells enter the cell cycle after the completion of mitosis and the tumour's growth rate is slower.

Fraction of dormant (G0) cells that re-enter cell cycle (P_{G0toG1}). High values of the parameter P_{G0toG1} result in shorter doubling times and faster growing tumours. As P_{G0toG1} increases, more dormant cells re-enter the cell cycle and hence the number of dividing stem cells is higher. No upper or lower limit exists in this case.

Apoptosis rate of stem and LIMP cells (R_A). The apoptosis rate has a similar effect on doubling time to the parameters T_C and P_{sleep} . As the apoptosis rate increases, more stem cells die before reaching mitosis and hence fewer cells divide, resulting in a tumour with longer doubling time.

Dormant (G0) phase duration (T_{G0}). The increase of dormant phase duration leads to an increase in doubling time. However, for the range of T_{G0} considered in the study (up to 500h), the effect of this parameter is negligible.

It is worth noting that an upper limit in the case of T_C , P_{sleep} and R_A and a lower limit in the case of P_{sym} exists (depending on the values attributed to the rest of the parameters) beyond which tumour growth cannot be sustained.

T.3.2.2 Relative Cell Category Populations

Based on [Kolokotroni *et al.*, 2011] the following observations can be made regarding the effect of the model's parameters on the relative populations (fractions) of the various cell categories:

- Increasing the lifespan of a cell category (T_C , T_{G0} , T_N , T_A) results in an increase in its fraction in the tumour bulk, e.g. a high growth fraction (fraction of proliferating cells) is associated with a relatively high cell cycle duration
- A decrease in the 'removal' rate of living cells towards apoptotic or necrotic cell compartments (R_A , $R_{A,Diff}$, $R_{N,Diff}$) leads to an increase in its fraction in the tumour bulk (cell removal rate corresponds to the reciprocal of cell lifespan)
- Increasing the fraction of stem cells that performs symmetric divisions, P_{sym} , leads to a larger growth fraction and fraction of dormant cells, due to an increase in the fraction of stem cells (proliferative and dormant) in the tumour, which is reasonable as more stem cells are produced after mitosis, and a decrease in differentiated cells, as fewer cells follow the path to differentiation.
- Variations in the value of the fraction of cells that enter the G0 phase after mitosis would result in a redistribution of LIMP and stem cells in the dormant and the proliferative cell cycle phases. More specifically, as P_{sleep} increases the percentage of growth fraction (proliferating LIMP and stem cells) decreases, whereas the percentage of cells resting in G0 phase (dormant LIMP and stem cells) increases, to a lower, however, degree.
- Variation of the number of mitotic divisions that LIMP cells undergo before becoming terminally differentiated, N_{LIMP} , regulates only the relative populations of stem and LIMP cells and has no effect on the fraction of proliferating (LIMP and stem), dormant (LIMP and stem), differentiated and dead cell categories. More specifically, higher values of N_{LIMP} correspond to a higher fraction of LIMP and a lower fraction of stem cells population.

T3.2.3 Tumour Shrinkage

The effect of the model's parameters on tumour shrinkage one week after the last administration of the doublet regimen, has been investigated. Based on the derived results (Fig. T7 and Fig.T8) the following observations can be made:

Cell cycle duration (T_C). Slow-cycling cancer cell populations are associated with a better chemotherapeutic response. Longer cell cycle implies that less mitotic divisions take place within the

same time interval and, hence, the tumour grows at a slower pace. Since the replenishment of the cells lost due to chemo and, hence, the tumour repopulation between the drug administrations decelerates, the therapy-induced tumour shrinkage is greater. On the other hand, if the cell cycle is too short, even though therapy will slow growth, the tumour may fail to shrink with treatment.

Symmetric division fraction (P_{sym}). A large fraction of stem cells that undergo symmetric divisions (P_{sym}) may imply a poor treatment response. As the frequency of symmetric self-renewals increases, stem cells replace their treatment-induced losses quicker and repopulate the tumour at a higher pace, resulting in less tumour shrinkage. For values of P_{sym} above a limit, the treatment may not be effective in shrinking the tumour.

Fraction of newborn cells entering G0 (P_{sleep}). The effect of P_{sleep} on doubling time is similar to the case of the cell cycle duration parameter. A high fraction of newborn cells that enter a quiescent state after mitosis is associated with slowly growing tumours, due to the small number of newborn cells that begin a new cycle. Therefore, the repopulation of surviving cells during treatment cycles is slower, the tumour shrinkage is greater and, hence, the treatment response is better.

Fraction of dormant (G0) cells that re-enter cell cycle (P_{G0toG1}). G0 cells are removed from the corresponding class at a rate equal to the reciprocal of the dormant phase duration. A fraction equal to P_{G0toG1} re-enters the cell cycle, whereas the rest ($1 - P_{G0toG1}$) dies through necrosis. Increase of the value of P_{G0toG1} leads to a decrease in tumour shrinkage. For relatively high values, therapy cannot outstrip tumour growth rate and the final volume is greater than the initial one.

Apoptosis rate of stem and LIMP cells (R_A). Spontaneous cell loss has been considered the same for proliferating and dormant cells. Higher values of R_A are associated with tumours evolving at a slower pace and hence with better therapeutic response. On the other hand, for values of R_A close to zero the therapy has a modest effect on tumour shrinkage.

Apoptosis rate of differentiated cells (R_{ADiff}). For the considered values of the rest of the model parameters, the effect of spontaneous apoptosis rate of terminally differentiated cells on chemotherapeutic outcome is negligible.

Necrosis rate of differentiated cells (R_{NDiff}). This parameter corresponds to the mechanism of necrosis due to a deficient supply of nutrients and oxygen to the differentiated cells. For values of R_{NDiff} close to zero, increase of the parameter results in a remarkable increase of tumour shrinkage, however, for higher values, variation of the parameter has no effect on tumour regression. As the chemotherapeutic agent considered in these studies targets proliferating and G0 cells (stem and LIMP), there is a delay in the appearance of the effect of therapy on the rest of the cell categories (differentiated and dead cells). When this delay is small, the effect of therapy passes onto the differentiated cells quicker and their population declines in a greater extent. This delay is small, when the lifespan of the differentiated cell category is short and/or their portion in the bulk of the tumour is low. Higher values of R_{NDiff} are associated with shortly lived differentiated cells and hence a lower fraction of differentiated cells. The effect of the variation of the above parameter on therapeutic outcome is insignificant when the delay is small enough compared to the period between two drug administrations.

Dormant (G0) phase duration (T_{G0}). The variation of this parameter seems to have an insignificant effect on tumour response to treatment.

Apoptosis duration (T_A). Because of the very low fraction of apoptotic cells and their rapid removal rate from the tumour bulk, the variation of T_A has no effect on tumour response to treatment.

Necrosis duration (T_N). Increase in necrosis duration results in a decrease in volume reduction. However the effect is profound for considerably high values of the parameter. Prolonged necrosis duration is associated with a high proportion and a slow elimination rate of necrotic cells. Hence, as in the case of differentiated cells, therapy ‘delays’ in affecting this population and the response is worst.

Number of LIMP stages (N_{LIMP}). The parameter refers to the number of mitotic divisions that LIMP cells undergo before becoming terminally differentiated. Variation of this parameter regulates only the relative populations of stem and LIMP cells. Since, in the present study, therapy is considered to equally affect stem and LIMP cells, the parameter has no effect on treatment outcome.

Cell kill rate (CKR): The outcome of a chemotherapeutic scheme strongly depends on the pharmacodynamics of the chemotherapeutic agent used. The model successfully simulates the shrinkage of a tumour to a higher degree as the cell kill ratio increases. The value of the cell kill ratio could be thought of as summarizing important genetic determinants influencing a particular patient’s tumour response to chemotherapy. There exists a limit in the cell kill ratio values, below which the specific therapeutic scheme fails to shrink the tumour. This limit primarily depends on the growth rate of the simulated tumour. The deviation in the parametric results between drugs A and B is due to the fact that drug B is given twice as often.

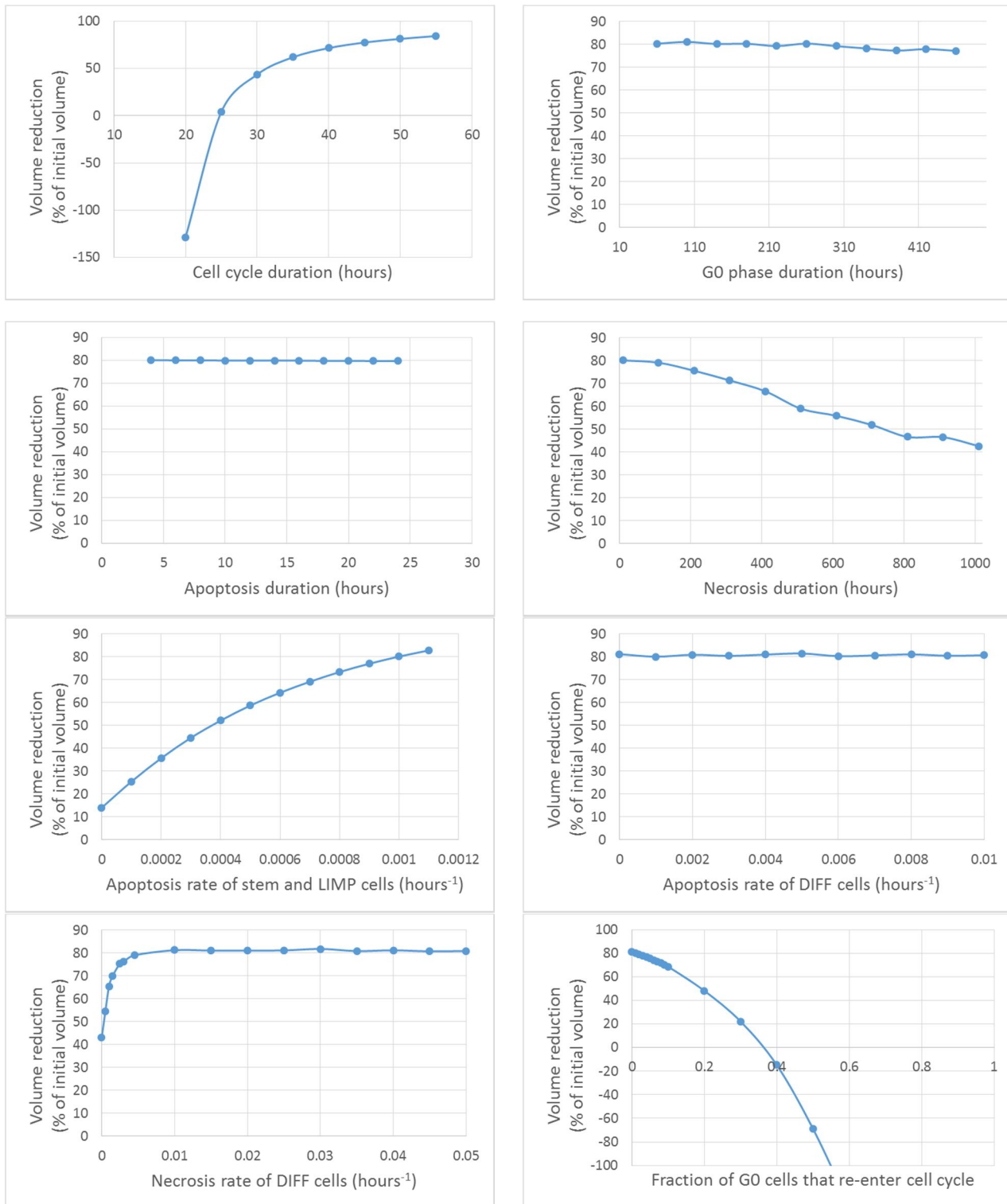


Fig. T7: Effect of model input parameters on the tumour volume reduction. The values assigned to the rest of the model input parameters are reported in Table T-X.

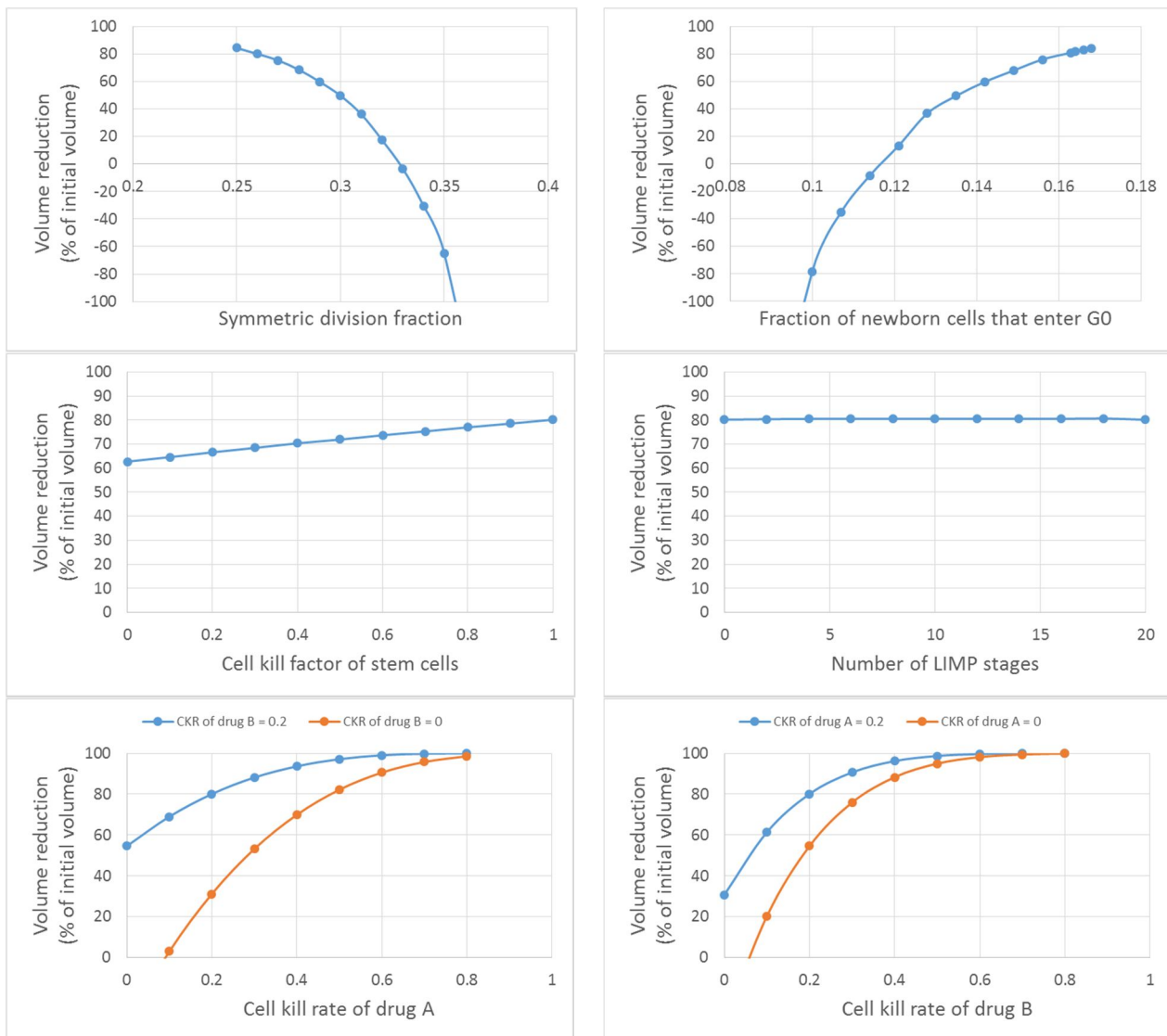


Fig. T8: Effect of model input parameters on the tumour volume reduction. The values assigned to the rest of the model input parameters are reported in Table T-X.

T3.3 LHS/RCC Analysis

OFAT is the most straightforward approach to determine parameter sensitivity, understand the relation between input and output and identify the most or less critical parameters of a model. However, this approach does not take into account the presence of correlations between inputs and cannot catch the effect of simultaneously varying more than one parameter on output. Sampling-based approaches are considered more appropriate for the study of multi-parametric models. The Latin Hypercube Sampling method is considered an efficient tool used to generate a set of well distributed combinations of model parameter values. It provides the best compromise between efficient coverage of input parameter space and realistic assessment of the combined effect of inputs on output, with a relatively small sample size.

Due to the unavailability of relevant data, a uniform distribution for all of the model parameters has been assumed. LHS is run to produce 500 combinations of parameter values. For each combination the volume doubling time, the fraction of the various cell categories and the volume reduction are calculated. For each model parameter, a scatter plot displaying the 500 values for the parameter under examination against CKR is produced. A statistical analysis of the scatter plots is subsequently performed in order to quantify and rank the correlation between inputs and outputs. A rank transformation has been applied to account for the effect of nonlinear but monotonic relationships between the inputs and outputs. Specifically, the values of inputs/outputs data are replaced by their ranks and the correlation coefficients are calculated on the rank transformed data. $P < .01$ has been considered as statistically significant. Values of RCC (Rank Correlation Coefficient) close to ± 1 indicate a strong influence of the input parameter on output. The parameters with RCC values > 0.5 or < -0.5 are the most important. The negative sign indicates an inversely proportionality between the input parameter and the outcome measure.

Indicative results of the Latin Hypercube Sampling-based sensitivity analysis in the form of scatterplots are presented in Fig.T9 - Fig.T11. The more the shape an input parameter imparts on the output measure, the stronger the correlation between them. The rank correlation coefficients accompanied by their p-values are reported in Table T-II and Table T-III. Correlations above 0.2 (moderate to strong) are denoted in bold. The following observations can be made:

- The most determinant factor in treatment response is the rate at which tumour replenishes its treatment-induced losses. In our modelling approach this rate is reflected in the rate that grows in the absence of treatment, i.e. in the volume doubling time.
- Tumours with doubling time approximately above 60 days consistently shrink as a result of treatment, independent of the specific choice of input parameter values.
- The sensitivity of tumour cells to the chemo regimen, as reflected in the value of cell kill rate, also has a considerable effect on treatment outcome.
- A higher fraction of stem cells and a lower growth fraction are associated with worst short-term treatment response, however the influence seems moderate.
- The fraction of stem cells is most sensitive to the self-renewal rate followed by the number of LIMP stages (for the value range considered)
- The growth fraction is most sensitive to the cell losses due to starvation (as reflected in the parameter P_{sleep}), followed by the cell cycle duration. The same applies for the fraction of dormant cells.
- As anticipated, a higher self-renewal rate of stem cells leads to a lower fraction of terminally differentiated cells.

TABLE T-II. RANK CORRELATION COEFFICIENTS RESULTS
(p-values in italics)

(p-values in italics)	Doubling time	Volume reduction
Fraction of Stem Cells	-0.14393 <i>P=0.001385</i>	-0.24235 <i>P<10⁻⁶</i>
Fraction of LIMP Cells	0.072905 <i>P=0.106636</i>	0.224451 <i>P<10⁻⁶</i>
Growth Fraction	-0.0333 <i>P=0.461552</i>	0.251282 <i>P<10⁻⁶</i>
Fraction of Dormant Cells	-0.07307 <i>P=0.105823</i>	-0.2471 <i>P<10⁻⁶</i>
Fraction of Terminally Differentiated Cells	0.149931 <i>P=0.00086</i>	0.148182 <i>P=0.00093</i>
Fraction of Apoptotic Cells	0.012714 <i>P=0.778696</i>	0.101851 <i>P=0.023</i>
Fraction of Necrotic Cells	0.246278 <i>P<10⁻⁶</i>	0.106378 <i>P=0.018</i>
Doubling Time	1 <i>P<10⁻⁶</i>	0.520082 <i>P<10⁻⁶</i>

TABLE T-III. RANK CORRELATION COEFFICIENTS RESULTS
(p-values in italics)

	Doubling Time	Fraction of Stem Cells	Fraction of LIMP Cells	Growth Fraction	Fraction of Dormant Cells	Fraction of DIFF Cells	Fraction of Apoptotic Cells	Fraction of Necrotic Cells	Volume reduction
T_c	0.008686 $P=$ <i>0.847751</i>	0.187657 $P=$ <i>0.000029</i>	-0.0346 $P=$ <i>0.444328</i>	0.67201 $P<10^{-6}$	-0.45676 $P<10^{-6}$	-0.26984 $P<10^{-6}$	0.145984 $P=$ <i>0.001179</i>	-0.33182 $P<10^{-6}$	0.103748 $P=$ <i>0.021491</i>
T_{G0}	0.019394 $P=$ <i>0.66815</i>	0.03767 $P=$ <i>0.404913</i>	0.040617 $P=$ <i>0.369143</i>	-0.18064 $P=$ <i>0.000057</i>	0.208857 $P=$ <i>0.000003</i>	-0.10769 $P=$ <i>0.016985</i>	-0.10946 $P=$ <i>0.015241</i>	-0.15002 $P=$ <i>0.000854</i>	-0.0531 $P=$ <i>0.240253</i>
T_N	-0.02518 $P=$ <i>0.577738</i>	-0.02096 $P=$ <i>0.643084</i>	-0.02208 $P=$ <i>0.625501</i>	0.011601 $P=$ <i>0.797638</i>	-0.06019 $P=$ <i>0.183051</i>	0.081335 $P=$ <i>0.071757</i>	-0.14708 $P=$ <i>0.001081</i>	0.565302 $P<10^{-6}$	-0.0997 $P=$ <i>0.027175</i>
T_A	0.186979 $P=$ <i>0.000031</i>	-0.01418 $P=$ <i>0.753977</i>	-0.02587 $P=$ <i>0.56745</i>	0.055268 $P=$ <i>0.221531</i>	-0.08883 $P=$ <i>0.049172</i>	0.063303 $P=$ <i>0.161357</i>	0.68221 $P<10^{-6}$	0.016769 $P=$ <i>0.7109</i>	0.117287 $P=$ <i>0.009288</i>
R_A	0.046398 $P=$ <i>0.304872</i>	0.247986 $P<10^{-6}$	-0.22903 $P<10^{-6}$	0.469885 $P<10^{-6}$	-0.38564 $P<10^{-6}$	-0.06357 $P=$ <i>0.159604</i>	0.550288 $P<10^{-6}$	-0.07305 $P=$ <i>0.10594</i>	-0.0237 $P=$ <i>0.600407</i>
R_{ADiff}	-0.0267 $P=$ <i>0.555039</i>	-0.03634 $P=$ <i>0.421736</i>	0.06525 $P=$ <i>0.148822</i>	0.008997 $P=$ <i>0.842369</i>	0.035526 $P=$ <i>0.43219</i>	-0.06587 $P=$ <i>0.145016</i>	0.084195 $P=$ <i>0.062294</i>	-0.04394 $P=$ <i>0.331198</i>	0.015606 $P=$ <i>0.730127</i>
R_{NDiff}	0.010782 $P=$ <i>0.811646</i>	0.094794 $P=$ <i>0.03574</i>	0.182922 $P=$ <i>0.000046</i>	0.102576 $P=$ <i>0.023018</i>	0.141779 $P=$ <i>0.001635</i>	-0.43579 $P<10^{-6}$	-0.13358 $P=$ <i>0.00302</i>	0.14547 $P=$ <i>0.001228</i>	-0.04068 $P=$ <i>0.368431</i>
P_{G0toG1}	0.084485 $P=$ <i>0.061395</i>	0.009633 $P=$ <i>0.83139</i>	-0.03925 $P=$ <i>0.38545</i>	-0.18227 $P=$ <i>0.000049</i>	0.151911 $P=$ <i>0.000732</i>	-0.02717 $P=$ <i>0.548096</i>	0.024335 $P=$ <i>0.590621</i>	-0.14657 $P=$ <i>0.001125</i>	-0.00425 $P=$ <i>0.925205</i>
P_{sym}	-0.22389 $P=$ <i>0.000001</i>	0.798332 $P<10^{-6}$	-0.45972 $P<10^{-6}$	-0.03861 $P=$ <i>0.393298</i>	0.387114 $P<10^{-6}$	-0.84083 $P<10^{-6}$	0.269024 $P<10^{-6}$	-0.54902 $P<10^{-6}$	-0.27086 $P<10^{-6}$
P_{sleep}	-0.08882 $P=$ <i>0.049189</i>	0.387702 $P<10^{-6}$	-0.12713 $P=$ <i>0.004782</i>	-0.78927 $P<10^{-6}$	0.942498 $P<10^{-6}$	-0.52483 $P<10^{-6}$	-0.17891 $P=$ <i>0.000067</i>	-0.24306 $P<10^{-6}$	-0.1887 $P=$ <i>0.000026</i>
N_{LIMP}	-0.05411 $P=$ <i>0.231415</i>	-0.53258 $P<10^{-6}$	0.566091 $P<10^{-6}$	-0.0027 $P=$ <i>0.952459</i>	0.00183 $P=$ <i>0.96773</i>	0.006829 $P=$ <i>0.880024</i>	-0.05413 $P=$ <i>0.231219</i>	-0.01503 $P=$ <i>0.739725</i>	0.130355 $P=$ <i>0.00381</i>
CKR_A	0.003866 $P=$ <i>0.93191</i>	0.073472 $P=$ <i>0.103932</i>	-0.05408 $P=$ <i>0.231614</i>	-0.01691 $P=$ <i>0.708557</i>	0.051926 $P=$ <i>0.250787</i>	-0.04977 $P=$ <i>0.271053</i>	-0.07415 $P=$ <i>0.100791</i>	-0.00718 $P=$ <i>0.873877</i>	0.339066 $P<10^{-6}$
CKR_B	0.026783 $P=$ <i>0.553803</i>	-0.01405 $P=$ <i>0.756204</i>	-0.01818 $P=$ <i>0.68785</i>	0.014133 $P=$ <i>0.754754</i>	-0.03497 $P=$ <i>0.43942</i>	0.04381 $P=$ <i>0.33267</i>	0.070398 $P=$ <i>0.119262</i>	0.013432 $P=$ <i>0.766557</i>	0.471956 $P<10^{-6}$
CKR_{Total}	-0.00824 $P=$ <i>0.855505</i>	0.016772 $P=$ <i>0.710853</i>	-0.04746 $P=$ <i>0.293917</i>	-0.02655 $P=$ <i>0.55733</i>	0.013869 $P=$ <i>0.759192</i>	0.030421 $P=$ <i>0.50125</i>	-0.01653 $P=$ <i>0.714917</i>	0.017045 $P=$ <i>0.706346</i>	0.604767 $P<10^{-6}$
CKF	0.002234 $P=$ <i>0.960612</i>	-0.09012 $P=$ <i>0.045935</i>	0.080008 $P=$ <i>0.07653</i>	0.016564 $P=$ <i>0.714275</i>	-0.03535 $P=$ <i>0.434499</i>	0.046497 $P=$ <i>0.303844</i>	0.012204 $P=$ <i>0.787361</i>	0.065195 $P=$ <i>0.149167</i>	0.271891 $P<10^{-6}$

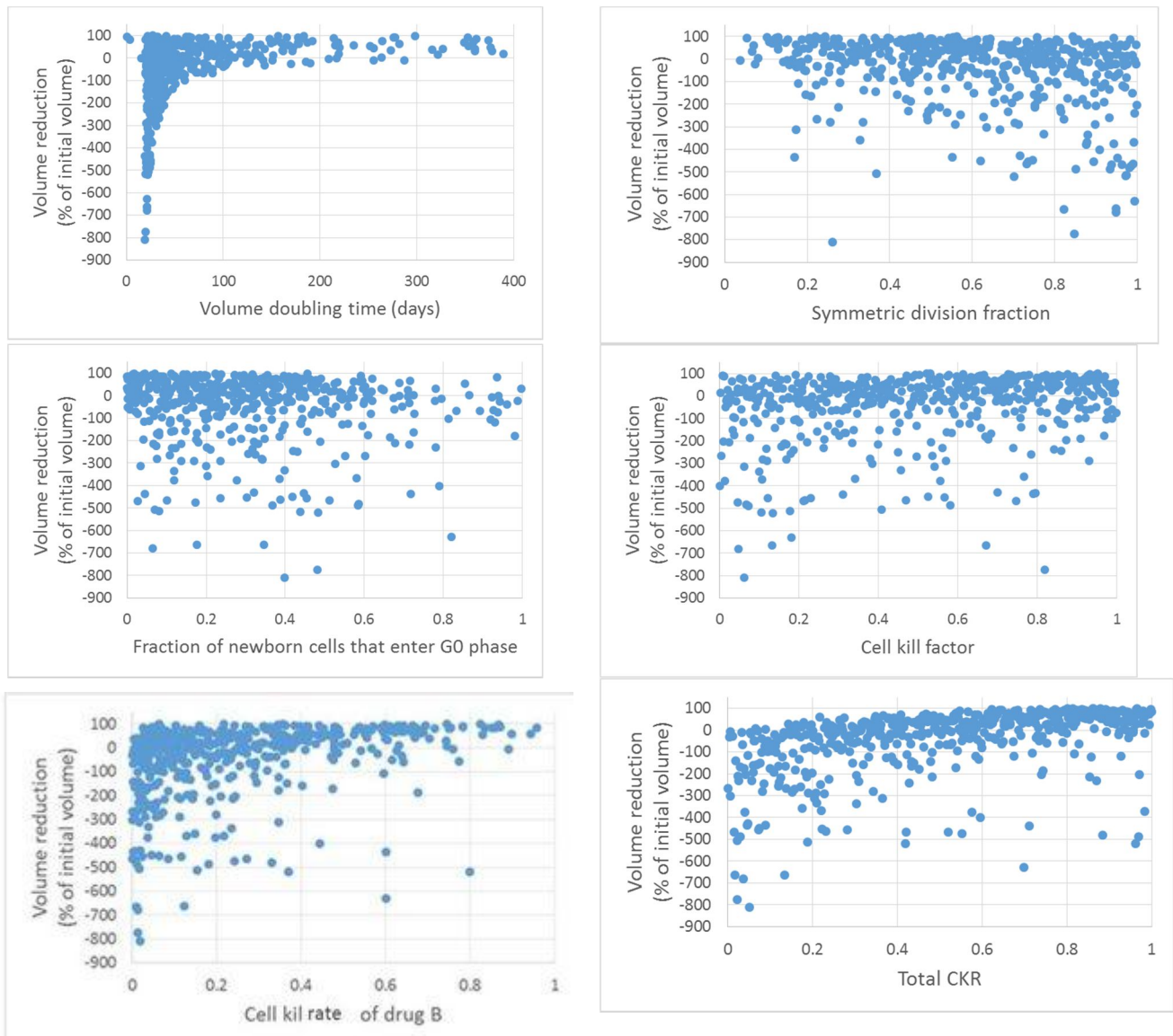


Fig. T9 Latin Hypercube Sampling-based sensitivity analysis by scatterplots. The effect of indicative input parameters on tumour volume reduction.

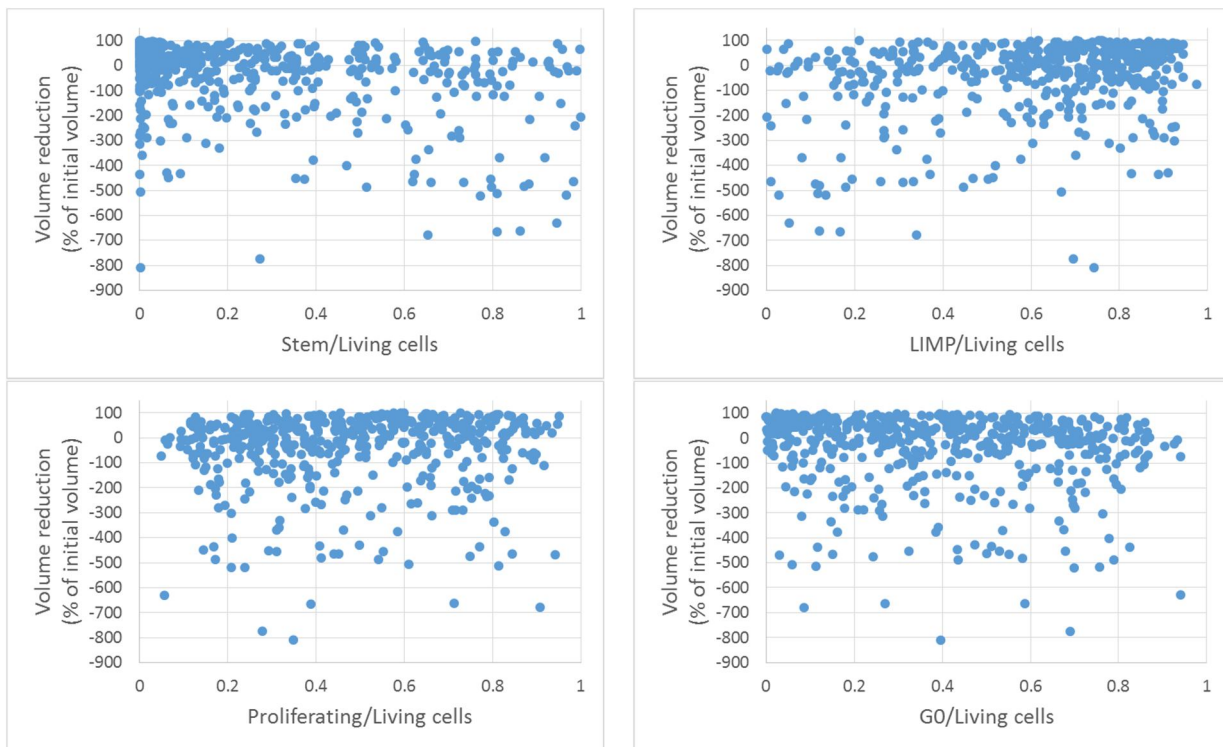


Fig. T10 Latin Hypercube Sampling-based sensitivity analysis by scatterplots. The effect of indicative input parameters on tumour volume reduction.

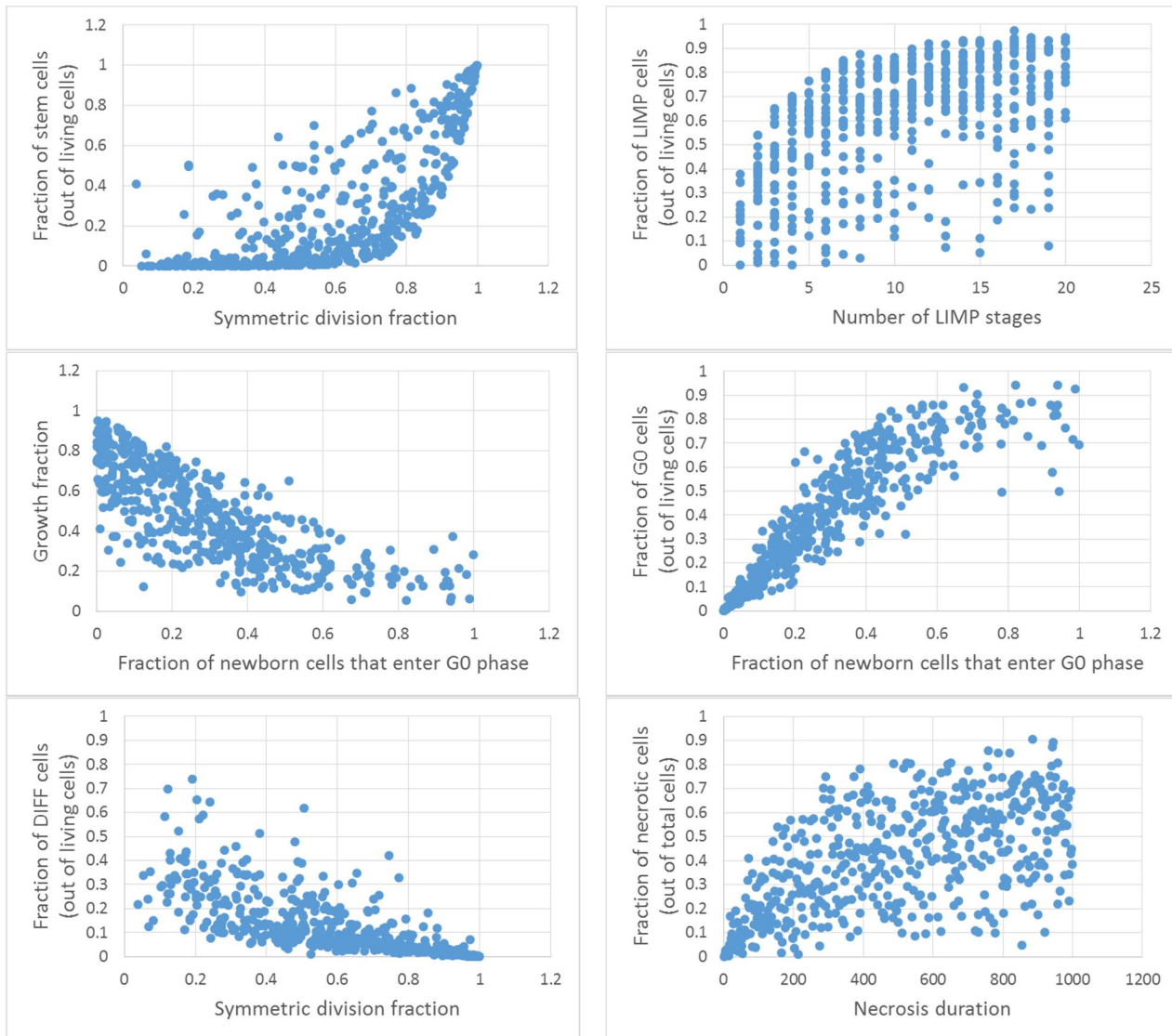


Fig. T11: Latin Hypercube Sampling-based sensitivity analysis by scatterplots. The effect of indicative input parameters on various cell category fractions.

T4. The Lung Cancer Clinical Adaptation Paradigm

In this section a proof of concept clinical adaptation paradigm is presented. More specifically, the core of the ICCS-NTUA *In Silico* Oncology and *In Silico* Medicine Group discrete model presented previously has been applied to the case of lung cancer neoadjuvant chemotherapy treatment. More specifically, the model has been applied to a clinical data set of 2 patients with primary lung cancer, treated with a combination of cisplatin and gemcitabine (2 three-week cycles). On the first day of treatment cycle the patients is given both the gemcitabine and cisplatin. On the same day of the following week (day eight) only Gemcitabine is administrated. The study is focused on the cytotoxic efficacy of cisplatin and gemcitabine, as expressed by the apparent cell kill rate (CKR) of the drug, i.e. the fraction of cancer cells that are lethally hit by the drugs after each chemotherapeutic session. The CKR can be thought of as summarizing important genetic determinants influencing the tumour response to therapy. Here, a plausible value combination of the apparent cell kill rate (CKR) of the drugs involved is suggested following the exploitation of cancer-specific literature data, the actual clinical data and the simulation outcome.

The data following anonymization has been provided by the Institute of Pathology, University Hospital of Saarland, and the Saarland Tumour Centre, Germany in the framework of ContraCancrum European Commision-funded program (FP7-ICT-2007-2- 223979).

T4.1 NSCLC Proliferation Kinetics

Growth rate: Table T-IV summarizes some of the largest studies on the growth rate of primary NSCLC found in literature. The review reveals a very wide range of tumour volume doubling times spanning from ~20 days to negative values. Regardless of method, the vast majority of studies have reported shorter doubling times in SCC than in ADC. Mean and median values for SCC are usually below 140 days, whereas slowly growing or stable tumours (with doubling time more than a year or negative) are more frequently reported for the ADC type. Notably, for cases with three or more tumour observations, the growth rate appears fairly constant on the log scale over the observation period [Geddes 1979; Quint *et al.*, 2008; Friberg and Mattson 1997].

Growth fraction: In the vast majority of the reviewed studies Ki-67 values derive from specimens of surgically resected tumours, without pre-operative systemic therapy or radiotherapy. A wide range of Ki-67 values has been observed for NSCLC [0-94% depending on study], whereas Ki-67 index has consistently been reported to be lower in adenocarcinoma than in squamous cell carcinoma (Table T-V)[Huang *et al.*, 2005]. Regarding prognosis, Ki-67 LI seems to be of significance in NSCLC with a high value indicating poor prognosis.

Cell cycle time: For the purposes of the present study, the average cell cycle duration of human lung tumours, *in vivo*, is assumed to be reflected in the mean generation time (or population doubling time) of lung cancer cell lines. In the reviewed literature, population doubling times of established cell lines derived from patients with adenocarcinoma or squamous cell carcinoma range between 18 h and 134 h (Table T-VI).

Necrosis: During tumour growth, cell necrosis is believed to be the result of oxygen supply deprivation (hypoxia) caused by an insufficient tumour vascular network. A positive correlation of necrosis extent with increased tumour size [Koskal *et al.*, 2013], high-grade (poorly differentiated)

disease and poor prognosis (especially for stage I and II disease) has been demonstrated [Park *et al.*, 2011]. The above findings suggest that extensive tumour necrosis reflects a fast growing tumour that outstrips its blood supply and, hence, is associated with a more aggressive tumour phenotype [Park *et al.*, 2011]. Necrosis appears more often in SCC than in ADC indicating the more aggressive nature of the former type [Koskal *et al.*, 2013] (Table T-VII).

Apoptosis: Consistent with most solid tumour types [Proskuryakov & Gabai, 2010], the frequency of apoptosis in NSCLC appears to be very low, most likely due to the rapid formation and phagocytic clearance of apoptotic debris *in vivo* (Kerr *et al.* 1972; Dewey *et al.*, 1995; Ribba *et al.* 1996). In the reviewed studies (Table T-VIII), the mean apoptotic index (AI - expressed as the number of apoptotic cells and/or bodies per 100 malignant cells) spans from 0 to 12%, with a mean and median value ranging between 0.3-4.3 and 0.8–4, respectively. Higher levels of apoptosis have been reported in literature for SCC than ADC; however, the difference is not characterized as statistically significant.

Cancer stem cells (CSCs): In the majority of the reviewed publications, the reported frequencies for lung cancer ADC and SCC, either in primary tumours or established cell lines, is below 0.01%. The method used is based on the tumour formation incidence following inoculation of varied quantities of tumour cells in immunocompromised mice. However, it has been argued that the microenvironment limitations of the immunocompromised mice used for xenotransplantation may result in an underestimation of the true CSC percentage [Kelly *et al.*, 2007; Quintana *et al.*, 2008]. These findings motivated Ishizawa *et al.* (2010) to compare the tumourigenic capacity of a variety of solid tumours, including lung adenocarcinoma and squamous cell carcinoma, using both typical (NOD/SCID mice) and highly permissive (NSG mice) xenotransplantation conditions. Although elevated, the study failed to demonstrate high proportions of CSCs using NSG mice, in all of the primary tumours examined. More specifically, the estimated frequency of CSCs was of the order of 10^{-5} in non-small cell lung adenocarcinoma and 10^{-5} - 10^{-4} in squamous cell carcinoma [Table T-IX].

Table T-IIIV. TUMOUR VOLUME DOUBLING TIMES IN DAYS FOR NSCLC ACCORDING TO HISTOLOGICAL TYPE

Study	Number of cases	Mean $\pm \sigma$	Median	Range
Adenocarcinoma				
Spratt <i>et al.</i> , 1963	7	269	-	Min:32
Steel, 1977	64	148	-	-
Geddes, 1979	60	161	-	-
Kerr and Lamb, 1984	4	72	-	23-110
Usuda <i>et al.</i> , 1994	86	223.1 \pm 209.4	-	-
Hasegawa <i>et al.</i> , 2000	49	533	-	-
Winner-Muram <i>et al.</i> , 2002	15	-	157	64-(-26711)
Jennings <i>et al.</i> , 2006	51	166**	216**	32-(-52)**
Lindell <i>et al.</i> , 2007	22 non-BAC 9 BAC	746 780	343 210	-
Quint <i>et al.</i> , 2008	15	127	181	58-2239
Honda <i>et al.</i> , 2009	35	976 \pm 3134)	258	69 -18678 [†] 5 cases negative
Dhopeshwarkar <i>et al.</i> , 2011	21	292	227	-
Henschke <i>et al.</i> , 2012	55	-	140 (solid) 251 (subsoid)	-
Kanashiki <i>et al.</i> , 2012	140	177	134	-
Murai <i>et al.</i> , 2012	135	-	170	-
Heuvelmans <i>et al.</i> , 2013	15	-	196	-
Mackintosh <i>et al.</i> , 2014	36	-	294**	54-2256 [†] 3 cases negative
Nakamura <i>et al.</i> , 2014	69	-	305	-
Squamous cell carcinoma				
Spratt <i>et al.</i> , 1963	6	93	-	14-(-325)
Steel, 1977	85	85	-	-
Geddes, 1979	111	88	-	-
Kerr and Lamb, 1984	7	146	-	20-382
Usuda <i>et al.</i> , 1994	67	104.7 \pm 105.6	-	-
Hasegawa <i>et al.</i> , 2000	8	129 \pm 97	-	-
Winner-Muram <i>et al.</i> , 2002	16	-	119	33-1004
Jennings <i>et al.</i> , 2006	48	132**	142**	26-(-50)**
Lindell <i>et al.</i> , 2007	8	103	88	-
Quint <i>et al.</i> , 2008	11	128	139	79-901
Honda <i>et al.</i> , 2009	11	126 \pm 58	131	39-221
Dhopeshwarkar <i>et al.</i> , 2011	4	73	63	-
Henschke <i>et al.</i> , 2012	21	-	88	-
Kanashiki <i>et al.</i> , 2012	44	133	99	-
Murai <i>et al.</i> , 2012	66	-	93	-
Heuvelmans <i>et al.</i> , 2013	6	-	142	-
Mackintosh <i>et al.</i> , 2014	6	-	97	66-255
Nakamura <i>et al.</i> , 2014	-	-	81	-

Table T-V. Ki-67(%) LABELING INDEX FOR NON-SMALL CELL LUNG CANCER

Study	No of patients	Stage	Mean $\pm \sigma$	Median	Range
Soomro & Whimster, 1990	ADC: 30 SCC:36	-	10.99 \pm 11.09 15.71 \pm 12.59	7.45 13.8	0-47.5 0-49.2
Hayashi <i>et al.</i> , 1993	ADC:34 SCC:19	-	15.2 \pm 1.8 29.5 \pm 3.5	-	0-50** 10-70**
O'Neill <i>et al.</i> 1996	ADC:22 SCC:54	T1, T2	21 31.8	-	5.2-56.2 8.9-72
Rudolph <i>et al.</i> , 1998	23	-	38.3 \pm 17.8	-	-
Hommura <i>et al.</i> , 2000	215	(p) I-IV	36.7 \pm 27.3	-	0-93
Cagini <i>et al.</i> , 2000	99	I, II	25.3 \pm 19.3	20	-
Demarchi <i>et al.</i> , 2000	ADC:64	I-III	21.6 \pm 16.8	22.22	0-67
van de Vaart <i>et al.</i> 2000	27	III	59.6 \pm 19.3	60.3	22-94.3
Rigau <i>et al.</i> , 2002	86	I-IV		37	-
Tsoli <i>et al.</i> , 2001	Total:69 ADC:33 SCC:31 ULC:5	I-III	34.8 \pm 11.29 29.4 \pm 10.1 40.14 \pm 10.42	33.1 29.2 39.65	4.6 -70.4
Ferreira <i>et al.</i> , 2001	Total:144	I-III	49.3 \pm 25.1	-	-
Takahashi <i>et al.</i> , 2002	Total:62	pT1-pT4	24.5	-	-
Haga <i>et al.</i> 2003	Total:187 ADC:122 SCC:65	I	19.3 10.7 35.4	-	-
Tsubochi <i>et al.</i> 2006	Total:219 ADC:116 SCC:97 AD/SCC:5 Large:1	I-III	18.9 12.0 26.1	-	-
Kaira <i>et al.</i> , 2008	Total: 321 ADC:200 SCC:100 Large:21	I-III	35 \pm 24 23 \pm 20 54 \pm 17 56 \pm 21	32 18 56	5-92
Warth <i>et al.</i> 2014	Total:1065 ADC:184 SCC:233		40.7 25.8 52.8		-
Chen <i>et al.</i> 2014	Total:191	I-IV		31	-

SCC: Squamous cell carcinoma, ADC: Adenocarcinoma, NSCLC: Non small cell lung cancer, UCL: undifferentiated large cell carcinoma

*Explicitly stated that neither chemotherapy nor radiotherapy was performed before surgery or biopsy

** Approximately determined from relevant graph in the study

Table T-VI. POPULATION DOUBLING TIME (IN HOURS) FOR HUMAN NON-SMALL CELL LUNG CANCER ESTABLISHED CELL LINES

Study	No of cell lines	Range (Median)
Lieber <i>et al.</i> , 1976	1 ADC	48
Kimura <i>et al.</i> , 1979	1 SCC	46
Loh <i>et al.</i> , 1984	3 ADC, 1 ADSCC	34.5, 36.1, 55.8, 102.8
Olsson <i>et al.</i> , 1984	1 SCC	~ 30 to 40
Brower <i>et al.</i> , 1986	7 ADC, 1 SCC	18-58 (38.5)
Masuda <i>et al.</i> , 1991	15 ADC, 1 SCC	21-65.5 (38.65)
Campling <i>et al.</i> , 1992	1 ADC	41.4
Liu & Tsao, 1993	4ADC, 1 SCC, 1ADSCC	53-134 (79.5)
Giaccone <i>et al.</i> , 1992	2 ADC	24, 72
Li <i>et al.</i> , 2012	1 ADC, 2SCC	25, 38, 42
ADSCC: mixed squamous and adenocarcinoma of the lung		

Table T-VII. PERCENT (%) OF VIABLE TUMOUR^A OR TUMOUR NECROSIS^B FOR NON-SMALL CELL LUNG CANCER

Study	No of patients	Stage	Mean $\pm \sigma$	Median	Range/ Distribution
Kessler <i>et al.</i> , 1996 ^b	Total:593 ADC:124 SCC:394 Large:46	I-III	15.7 \pm 0.9	5	-
Pataer <i>et al.</i> , 2012 ^a	Bronchoalveolar:29 Total:192				11-30 (6) 31-50% (27) 51-70% (64) 71-100% (69) >1/3 (11); <1/3 (87)
Khan <i>et al.</i> , 2004 ^b	Total:98 ADC:26 SCC:70 Undifferentiated:1 Bronchoalveolar:1				
Törmänen <i>et al.</i> , 1995 ^b	Total:75 ADC:24 SCC:47 LCC:1 SCLC:3	I-IIIa	-	-	SCC: 0% (3); 1-20% (24); 21-50% (13); 51-70% (6); >71% (1) ADC: 0% (17); 1-20% (2); 21-50% (2); 51-70% (2); >71% (1)
Lee <i>et al.</i> , 1989 ^b	Total:30 ADC:8 SCC:18 LCC:4	III	-	-	\leq 25%: 26 \geq 26%:4

Table T-VIII. APOPTOTIC INDEX (NUMBER OF APOPTOTIC CELLS AND APOPTOTIC BODIES PER 100 TUMOUR CELLS) FOR NON-SMALL CELL LUNG CANCER

Study	No of patients	Stage	Mean $\pm \sigma$	Median	Range
van de Vaart <i>et al.</i> , 2000	Total:27 ADC:6 SCC:11 Large:9 Undifferentiated:1	III	1.8	2	0-8
Tsoli <i>et al.</i> , 2001	Total:69 ADC:33 SCC:31 ULC:5	I-III	2 ± 1.97 2.35 ± 2.5 1.46 ± 1.09	1.35 1.4 1.15	0.1-10.6
O'Neill <i>et al.</i> 1996	Total:76 ADC:22 SCC:54	T1, T2	1.1 2.3	-	0.1-5.4 0.1-9.6
Ferreira <i>et al.</i> , 2001	Total:144 ADC:40 SCC:74 LCC:30	I-III	0.65 ± 0.41	-	-
Stammler & Volm, 1996	Total:178	I-III	0.37 ± 0.29	0.25	0-1.7
Ghosh <i>et al.</i> , 2001	SCC:134		0.3029 ± 0.2475	0.223	0.024-1.455
Hwang <i>et al.</i> , 2001	Total:68 ADC:6 SCC:62	I-III	4.3 ± 2.6 5.9 ± 3.54 4.1 ± 2.5	4	0.2-12
Gorgoulis <i>et al.</i> 2000	Total:63 ADC:30 SCC:28 ULC:5	I-III	2.009 ± 1.961 2.3 ± 2.5 1.56 ± 1.11	1.4 1.4 1.2	0.1-10.6
Langendijk <i>et al.</i> 2000	Total:75 SCC:37 Others:	III	0.9	-	0-10
Tanaka <i>et al.</i> 1999	Total:236 ADC:130 SCC:85 LCC:13 Others:8	I-IIIa	1.88 ± 0.14 1.97 ± 0.23 1.96 ± 0.19	1.1	-
Komaki <i>et al.</i> 1996	Total:173 ADC:73 SCC:86 LCC:3 AD-SCC:6 Others:8	-	-	1.0	0.2-2.8
Törmänen <i>et al.</i> 1995	Total:75 ADC:24 SCC:47 LCC:1 SCLC:3	I-IIIa	1.24 ± 0.24 1.20 ± 0.19	-	-
Dworakowska <i>et al.</i> , 2009	Total:170	-	1.2 ± 1.0 (of 168)	0.8 (of 168)	(2 had 0%)

SCC: Squamous cell carcinoma, ADC: Adenocarcinoma, NSCLC: Non-small cell lung cancer, ULC: undifferentiated large cell carcinoma

*Explicitly stated that neither chemotherapy nor radiotherapy was performed before surgery or biopsy

Values have been adjusted to express % of viable tumour cells

Table T-IX. FREQUENCY OF CANCER STEM CELLS (CSCs) IN NON-SMALL CELL LUNG CANCER

Study	Cell line/ Primary Sample	Percentage (%)	Mice
Ho <i>et al.</i> , 2007	6 cell lines H460, H23, HTB-58, A549, H441, H2170	H460: 0.0004* H441: 0.0054* A549: 0.0044*	NOD/SCID
Levina <i>et al.</i> , 2008	1 cell line H460	0.0026*	SCID
Ishizawa <i>et al.</i> , 2010	Primary tumours ADC: 3 SCC: 3	ADC: 0.0033-0.0063 SCC: 0.0063-0.0238	NSG
Zhang <i>et al.</i> , 2012	H460	ADC: 0.0023, <0.001 SCC: 0.008-0.0023 0.0003*	NOD/SCID NU/NU
Singh <i>et al.</i> , 2013	H1650	0.0073*	SCID-beige

SCC: Squamous cell carcinoma, ADC: Adenocarcinoma, NSCLC: Non-small cell lung cancer
 * Estimated from published data based on extreme limiting dilution analysis [Hu & Smyth, 2009]. Values have been rounded to four decimal places

T4.2 Modelling of Drug Mechanism Action

The cytotoxic effect of cisplatin on cancer cells has primarily been attributed to the formation of cisplatin-gDNA adducts (mainly I,2-d(GpG) and I,2-d(ApG) intrastrand cross-links) [Jordan & Carmo-Fonseca 2000; Siddik 2003; Wang *et al.*, 2004]. In an attempt to remove these adducts and restore DNA lesions, the cells undergo a transient S arrest and a more persistent G2/M arrest [Ormerod *et al.*, 1994]. Failure of DNA repair mechanisms, in case of extended damage, activates a number of signal transduction pathways (e.g. p53 involved pathways, c-Abl- and p73-dependent cascade, mitogen-activated protein kinase pathways, protein kinase C pathway, regulation of Bcl-2 family proteins, calcium signaling, death receptor signaling, mitochondrial pathways and caspases cascade) that lead to programmed cell death or apoptosis [Jordan & Carmo-Fonseca, 2000; Siddik, 2003; Wang *et al.*, 2004; Sedletska *et al.*, 2005; Florea & Büsselberg, 2011; Basu & Krishnamurthy, 2010]. Accumulating evidence, derived from various cancer cell lines including non small cell lung cancer, has linked the initiation of apoptotic pathway with the activity of mismatch repair proteins and the G2/M checkpoint [Sorenson *et al.*, 1990; Jordan & Carmo-Fonseca, 2000; Siddik, 2003; Wang *et al.*, 2004]. Lethally damaged cells seem to stay trapped, but viable, at G2/M phase for a few days and then proceed to death [Sorenson *et al.*, 1990]; in addition, entrance to mitosis and realization of a final aberrant mitosis prior to death has been observed [Demarcq *et al.*, 1994]. Cisplatin is cell cycle-non specific drug. In our modeling approach, tumour cells are assumed to absorb Cisplatin at all cycling phases, as well as at G0 phase, whereas apoptotic death of hit cells takes place in G2 phase.

Studies with a wide spectrum of cell lines [Cartee *et al.*, 1998; Tolis *et al.*, 1999; Cappella *et al.*, 2001; Mini *et al.*, 2006] have evinced apoptosis as the method of cell death induced by gemcitabine (dFdC). Inside the cell, dFdC undergoes a series of phosphorylations resulting in its active diphosphate (dFdC-DP) and triphosphate (dFdC-TP) forms. dFdC-induced apoptosis is primarily related with the incorporation of the triphosphate form into the DNA strand during replication, acting competitively with the normal nucleoside deoxycytidine triphosphate-dCTP [Huang and Plunkett, 1995; Cartee *et al.*, 1998; Mini *et al.*, 2006]. The inhibition of chain elongation and the inability of proofreading polymerases to recognize and remove the erroneous nucleoside (mask chain termination), impair DNA synthesis and induce apoptosis [Huang and Plunkett, 1995; Mini *et al.*, 2006]. The above effect is self-potentiated by the function of dFdC-DP that inhibits ribonucleotide reductase, causing

depletion of dCTP pool, and, hence, favors both dFdC phosphorylation and incorporation into DNA. Notably, in solid tumours, the cytotoxic effect of dFdC is not limited in the S-phase cells and the drug kill cells in all proliferative phases [Latz *et al.*, 1998; Cappella *et al.*, 2001]. dFdC also inhibits RNA synthesis [Ruiz van Haperen *et al.*, 1993; Mini *et al.*, 2006] and dCMP deaminase and CTP synthetase activities [Mini *et al.*, 2006]. In our modeling approach, tumour cells are assumed to absorb the drug at all cycling phases, whereas apoptotic death of hit cells takes place in S phase.

T4.3 Clinical Adaptation

The patient specific data that have been exploited by the model are the applied chemotherapeutic scheme (drugs, administration instants) and the 3D image of the tumour as reconstructed from CT imaging data. The sets of imaging data were provided for two time instants before and after the completion of the treatment. Due to the non availability of data related to any distinct internal metabolic regions, the virtual tumour implemented is homogeneous with a shape compliant to the reconstructed tumour image.

A two - step adaptation process is followed. The first step refers to the adaptation of the model parameters that regulate cancer free growth kinetics. In general, a large number of virtual tumour implementations (virtual instances) corresponding to certain given or known parameter values exist. Narrowing this large window of possible solutions, ideally to one solution for a specific clinical case, is a critical first step in the adaptation procedure. Due to the non-availability of proliferation indices, such as Ki-67, thymidine labeling or mitotic indexes, and data that could allow the precise estimation of the rate of tumour growth, such as at least two volumetric data before the therapy, a literature survey has provided biologically reasonable values for critical tumour kinetics features (Section T4.1). In the adaptation paradigm presented here the following assumptions/constraints were imposed, based on literature:

- Volume doubling time (T_d): 170 days
- Growth fraction: 35%
- Cell cycle duration: 48 days
- Percentage of necrotic cells (out of total cells): 10%
- Percentage of stem cells (out of living cells): 0.006%

At a second step, the CKR of the drugs is adapted to the observed tumour size reduction. Since the regimen given consists of two chemotherapeutic agents, it is not possible to accurately determine the cell kill rate of each drug from the data provided, even in the ideal case of the availability of the all required proliferation indices and tumour free growth kinetics features that would enable the excellent fitting of the model parameters to the clinical case examined. In the paradigm presented here an 'apparent' combination of the CKR of the drugs involved for the virtual tumour implementation considered is determined (Tables T-X and T-XI). The adaptation of CKR was performed automatically using an optimization procedure (the `fzero` command in Matlab), that returns the zero of the difference between the observed volume of the real tumour based on the 2nd DICOM data set and the final volume of the simulated tumour. The algorithm uses a combination of bisection, secant, and inverse quadratic interpolation methods.

An excellent fitting between the simulation results and the patient volumetric data has been achieved in all cases (deviation less than 1%). The results indicate a feasible value combination of the apparent CKR of the drugs, however, due to the small size of the sample examined and the consideration of only one possible virtual tumour implementation, no conclusion can be drawn.

Fig. T12 shows the simulated time course of tumour volume for all clinical cases. The time instances of drugs administration are evident. The onset (time 0) and the finishing time point of simulation correspond to the time instances of the initial and the final tumour CT image acquisition.

TABLE T-X. ADAPTATION OF PARAMETER VALUES USED FOR THE CLINICAL CASES SIMULATIONS AND RESULTING TUMOR CHARACTERISTICS

Parameter	Value
T_c	48 h
T_{G0}	190 h
T_N	20 h
T_A	6 h
N_{LIMP}	20
R_A	0.001 h^{-1}
R_{ADiff}	0.001 h^{-1}
R_{NDiff}	0.011 h^{-1}
P_{G0toG1}	0.01
P_{sym}	0.26
P_{sleep}	0.16183
CKRA	0.2
CKRB	0.2
CKF	1
Tumor Characteristic	Value
Doubling Time	170 d
Fraction of Stem Cells‡	0.00006
Fraction of LIMP Cells‡	0.57
Growth Fraction‡	0.35
Fraction of Dormant Cells ‡	0.22
Fraction of DIFF Cells‡	0.43
Fraction of Apoptotic Cells*	0.004
Fraction of Necrotic Cells*	0.10
‡out of living cells	
*out of total cells	

TABLE T-XI. CELL KILL RATE ADAPTATION

	Case Study	
	A	B
Cisplatin cell kill rate	0.16	0.23
Gemcitabine cell kill rate	0.13	0.2
Sum of cell kill rates	0.28	0.42
Initial tumour volume (mm ³)	100264	101216
Final tumour volume based on DICOM (mm ³)	46824	26336
Simulated final tumour volume (mm ³)	46668	25810
Relative reduction of the tumour volume based on the DICOM data (% of the original volume)	53.30	73.98
Relative reduction of the tumour volume based on the simulation predictions (% of the original volume)	53.45	74.50
Relative deviation between predicted and real tumour shrinkage (% of the real shrinkage)	-0.28	-0.70

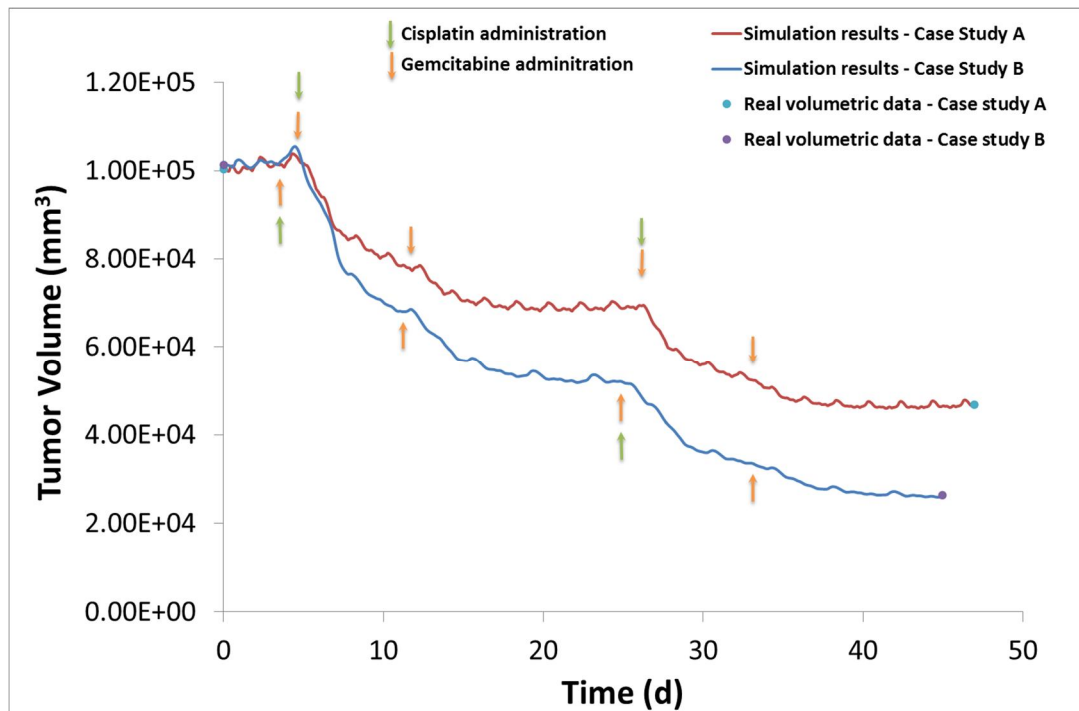


Fig. T12: Simulated time course of the tumour volume for the case studies A and B. The time points of each drug administration (Gemcitabin, Cisplatin) is indicated for each clinical case.

T5 References

Alakananda Basu and Soumya Krishnamurthy, "Cellular Responses to Cisplatin-Induced DNA Damage," *Journal of Nucleic Acids*, vol. 2010, Article ID 201367, 16 pages, 2010. doi:10.4061/2010/201367

Barnes, J.A., Dix, D.J., Collins, B.W., Luft, C., Allen, J.W., 2001. Expression of inducible Hsp70 enhances the proliferation of MCF-7 breast cancer cells and protects against the cytotoxic effects of hyperthermia. *Cell Stress Chaperones* 6 (4), 316–325.

Bast, R.C., Kufe, D.W., Pollock, R.E., Weichelbaum, R.R., Holland, J.F., Frei E., Eds. 2000. *Cancer Medicine* 5th ed., B.C. Decker Inc, Hamilton, Ontario, Canada

Begg A.C., Cell proliferation in tumours, in: G.G. Steel (Editor), *Basic Clinical Radiobiology*, second ed., Arnold, London, 1997.

Bertuzzi, A., Gandolfi, A., Sinisgalli, C., 1997. Steel's Potential Doubling Time and Its Estimation in Cell Populations Affected by Nonuniform Cell Loss. *Mathematical Biosciences* 143, 61-89

Bjerkvig R., B. Tysnes, K. Aboody, J. Najbauer, A. Terzis, The origin of the cancer stem cell: current controversies and new insights, *Nature* 5 (2005) 899-904.

Boyle P and Levin B (Eds), *World Cancer Report 2008*, World Health Organization, International agency for research on Cancer, Lyon, 2008.

Brower M, Carney DN, Oie HK, Gazdar AF, Minna JD. Growth of cell lines and clinical specimens of human non-small cell lung cancer in a serum-free defined medium. *Cancer Res.* 1986 Feb;46(2):798-806.

Bullwinkel J, Baron-Lühr B, Lüdemann A, Wohlenberg C, Gerdes J, Scholzen T, *et al.* Ki-67 protein is associated with ribosomal RNA transcription in quiescent and proliferating cells. *J Cell Physiol* 2006;206(3):624–35.

Cagini L, Monacelli M, Giustozzi G, Moggi L, Bellezza G, Sidoni A, Bucciarelli E, Darwish S, Ludovini V, Pistola L, Gregorc V, Tonato M. Biological prognostic factors for early stage completely resected non-small cell lung cancer. *J Surg Oncol.* 2000 May;74(1):53-60.

Campling BG, Haworth AC, Baker HM, Greer DL, Holden JJ, Bradley EC, Pym J, Dexter DF. Establishment and characterization of a panel of human lung cancer cell lines. *Cancer.* 1992 Apr 15;69(8):2064-74.

Cappella P, Tomasoni D, Faretta M, Lupi M, Montalenti F, Viale F, Banzato F, D'Incalci M, Ubezio P. Cell cycle effects of gemcitabine. *Int J Cancer.* 2001 Aug 1;93(3):401-8.

Cartee L, Kucera GL, Willingham MC. Induction of apoptosis by gemcitabine in BG-1 human ovarian cancer cells compared with induction by staurosporine, paclitaxel and cisplatin. *Apoptosis.* 1998 Dec;3(6):439-49.

Chen P, Li WM, Lu Q, Wang J, Yan XL, Zhang ZP, Li XF. Clinicopathologic features and prognostic implications of NOK/STYK1 protein expression in non-small cell lung cancer. *BMC Cancer.* 2014 Jun 4;14:402. doi: 10.1186/1471-2407-14-402.

Chignola R., A. Schenetti, G. Andrichetto, E. Chiesa, R. Foroni, S. Sartoris, G. Tridente, and D. Liberati, Forecasting the growth of multicell tumour spheroids: implications for the dynamic growth of solid tumours, *Cell Prolif.*, 33 (2000) 219-229.

Christine M. Sorenson, Michael A. Barry and Alan Eastman, Analysis of Events Associated With Cell Cycle Arrest at G2 Phase and Cell Death Induced by Cisplatin, *J Natl Cancer Inst* 82: 749–755, 1990.

Demarchi LM, Reis MM, Palomino SA, Farhat C, Takagaki TY, Beyruti R, Saldiva PH and Capelozzi VL, Prognostic values of stromal proportion and PCNA, Ki-67, and p53 proteins in patients with resected adenocarcinoma of the lung, *Mod Pathol* (2000) 13(5):511-20.

Demarcq C, Bunch RT, Creswell D, Eastman A, The Role of Cell Cycle Progression in Cisplatin-induced Apoptosis in Chinese Hamster Ovary Cells, *Cell Growth Differ.* 1994 Sep;5(9):983-93.

Dewey, W.C., Ling, C.C., Meyn, R.E., 1995. Radiation-induced apoptosis: relevance to radiotherapy. *Int. J. Radiat. Oncol. Biol. Phys.* 33 (4), 781–796.

Dhopeshwarkar MR, Roberts HC, Paul NS, Dong Z, Tsao M and Menezes RJ: Screen-detected lung cancer: a retrospective analysis of CT appearance. *Acad Radiol* 18: 1270-1276, 2011.

D.D.Dionysiou, G.S. Stamatakos, N.K.Uzunoglu, K.S.Nikita, A. Marioli , A Four Dimensional In Vivo Model of Tumour Response to Radiotherapy: Parametric Validation Considering Radiosensitivity, Genetic Profile and Fractionation , *J. theor. Biol.* , 230 , 1-20 , 2004

Dionysiou DD, Stamatakos GS, Uzunoglu NK, Nikita KS, A computer simulation of in vivo tumour growth and response to radiotherapy: New algorithms and parametric results, *Comp Biol Med* (2006) 36:448–464.

Dworakowska D., Jassem E., Jassem J., Karmolinski A., Lapinski M., Tomaszewski D., Rzyman W., Jaskiewicz K., Sworczak K. and Grossman A.B. (2009). Prognostic value of the apoptotic index analysed jointly with selected cell cycle regulators and proliferation markers in non-small cell lung cancer. *Lung Cancer* (Amsterdam, Netherlands) 66, 127.

Ferreira CG, van der Valk P, Span SW, Ludwig I, Smit EF, Kruijt FA, Pinedo HM, van Tinteren H, Giaccone G. Expression of X-linked inhibitor of apoptosis as a novel prognostic marker in radically resected non-small cell lung cancer patients. *Clin Cancer Res.* 2001 Aug;7(8):2468-74.

Fleckenstein D, K, Eble M, Blatter J, Wannenmacher M, Weber KJ. Radiosensitizing potential of gemcitabine (29,29-difluoro-29-deoxycytidine) within the cell cycle in vitro. *Intl J Radiat Oncol Biol Phys* 1998;41:875– 82.

Florea A-M, Büsselberg D. Cisplatin as an Anti-Tumour Drug: Cellular Mechanisms of Activity, Drug Resistance and Induced Side Effects. *Cancers.* 2011; 3(1):1351-1371.

Friberg S and Mattson S, On the Growth Rates of Human Malignant Tumours: Implications for Medical Decision Making, *J Surg Oncol* (1997) 65:284–297.

Geddes DM, The natural history of lung cancer: a review based on rates of tumour growth, *Br J Dis Chest* (1979) 73:1–17.

Gerdes J, Lemke H, Baisch H, Wacker HH, Schwab U, Stein H, *et al.* Cell cycle analysis of a cell proliferation-associated human nuclear antigen defined by the monoclonal antibody Ki-67. *J Immunol* 1984;133(4):1710–5.
Ghosh M, J Crocker, A Morris. Apoptosis in squamous cell carcinoma of the lung: correlation with survival and clinicopathological features. *J Clin Pathol* 2001;54:111–115

Giaccone G, Gazdar AF, Beck H, Zunino F, Capranico G. Multidrug sensitivity phenotype of human lung cancer cells associated with topoisomerase II expression. *Cancer Res.* 1992 Apr 1;52(7):1666-74.

Giatili SG, Stamatakis GS, Dionysiou DD, Kolokotroni EA and Georgiadi ECh, Geometrical and Mechanical Aspects of Tumour Growth and Response to Chemotherapeutic Schemes in the Context of the ACGT Oncosimulator, Proceedings of the 3rd International Advanced Research Workshop on In Silico Oncology, Istanbul, Turkey, Sept. 23-24, 2008. Edited by Stamatakis G and Dionysiou D pp.35-37, 2008

Gonzalez V.M., M.A. Fuertes, C. Alonso, J.M. Perez, Is cisplatin-induced cell death always produced by apoptosis?, Mol Pharmacol, 59 (2001), pp. 657–663

Gorgoulis VG, Kotsinas A, Zacharatos P, Mariatos G, Liloglou T, Tsoli E, Kokotas S, Fassoulas C, Field JK, Kittas C. Association of allelic imbalance at locus D13S171 (BRCA2) and p53 alterations with tumour kinetics and chromosomal instability (aneuploidy) in nonsmall cell lung carcinoma. Cancer. 2000 Nov 1;89(9):1933-45.

Graf N., A. Hoppe, What are the expectations of a Clinician from in Silico Oncology?. In proc. 2nd International Advanced Research Workshop on In Silico Oncology. 25-26 Sept. 2006, Kolymari, Chania, Crete. pp.36-38.

Gupta P.B., C.L. Chaffer, R.A. Weinberg, Cancer stem cells: mirage or reality? Nat. Med. 15 (9) (2009) 1010–1012.

Haga Y, Hiroshima K, Iyoda A, Shibuya K, Shimamura F, Iizasa T, *et al.* Ki-67 expression and prognosis for smokers with resected stage I non-small cell lung cancer. Ann Thorac Surg 2003;75(6):1727–32 [discussion 1732].

Hasegawa M, Sone S, Takashima S, Li F, Yang ZG, Maruyama Y and Watanabe T, Growth rate of small lung cancers detected on mass CT screening, Br J Radiol (2000) 73:1252–1259.

Henschke CI, Yankelevitz DF, Yip R, Reeves AP, Farooqi A, Xu D, Smith JP, Libby DM, Pasmantier MW, Miettinen OS; Writing Committee for the I-ELCAP Investigators. Lung cancers diagnosed at annual CT screening: volume doubling times. Radiology. 2012 May;263(2):578-83. doi: 10.1148/radiol.12102489. Epub 2012 Mar 27.

Hommura F, Dosaka-Akita H, Mishina T, Nishi M, Kojima T, Hiroumi H, Ogura S, Shimizu M, Katoh H and Kawakami Y, Prognostic significance of p27KIP1 protein and ki-67 growth fraction in non-small cell lung cancers, Clin Cancer Res (2000) 6(10):4073–4081.

Honda O, Johkoh T, Sekiguchi J, Tomiyama N, Mihara N, Sumikawa H, Inoue A, Yanagawa M, Daimon T, Okumura M and Nakamura H, Doubling time of lung cancer determined using three-dimensional volumetric software: Comparison of squamous cell carcinoma and adenocarcinoma, Lung Cancer (2009) 66(2):211-217.

Hu Y, Smyth GK. ELDA: extreme limiting dilution analysis for comparing depleted and enriched populations in stem cell and other assays. J Immunol Methods. 2009 Aug 15;347(1-2):70-8. doi: 10.1016/j.jim.2009.06.008. Epub 2009 Jun 28.

Huang C, Liu D Masuya D, Nakashima T, Kameyama K, Ishikawa S, *et al.* Clinical application of biological markers for treatments of resectable non-small-cell lung cancers. Br J Cancer 2005;92(7):1231–9. :

Huang CL, Liu D, Nakano J, Yokomise H, Ueno M, Kadota K, Wada H. E2F1 overexpression correlates with thymidylate synthase and survivin gene expressions and tumour proliferation in non small-cell lung cancer. Clin Cancer Res. 2007 Dec 1;13(23):6938-46.

Hwang JH, Lim SC, Kim YC, Park KO, Ahn SJ, Chung WK. Apoptosis and bcl-2 expression as predictors of survival in radiation-treated non-small-cell lung cancer. Int J Radiat Oncol Biol Phys. 2001 May 1;50(1):13-8.

Ishizawa K, Rasheed ZA, Karisch R, Wang Q, Kowalski J, Susky E, Pereira K, Karamboulas C, Moghal N, Rajeshkumar NV, Hidalgo M, Tsao M, Ailles L, Waddell TK, Maitra A, Neel BG, Matsui W. Tumour-initiating cells are rare in many human tumours. Cell Stem Cell. 2010 Sep 3;7(3):279-82. doi: 10.1016/j.stem.2010.08.009.

Jakobsen JN and Sørensen JB, Clinical impact of ki-67 labeling index in non-small cell lung cancer Lung Cancer (2013) 79(1):1-7.

Jennings SG, Winer-Muram HT, Tann M, *et al.* Distribution of stage I lung cancer growth rates determined with serial volumetric CT measurements. Radiology 2006;241:554–563.

Jordan, P.; Carmo-Fonseca, M. Molecular mechanisms involved in cisplatin cytotoxicity. Cell. Mol. Life Sci. 2000, 57, 1229–1235.

Kaira K, Oriuchi N, Imai H, Shimizu K, Yanagitani N, Sunaga N, Hisada T, Tanaka S, Ishizuka T, Kanai Y, Endou H, Nakajima T and Mori M, Prognostic significance of L-type amino acid transporter 1 expression in resectable stage I–III nonsmall cell lung cancer, Br J Cancer (2008) 98(4):742–748

Kanashiki M1, Tomizawa T, Yamaguchi I, Kurishima K, Hizawa N, Ishikawa H, Kagohashi K, Satoh H. Volume doubling time of lung cancers detected in a chest radiograph mass screening program: Comparison with CT screening. Oncol Lett. 2012 Sep;4(3):513-516. Epub 2012 Jun 28.

Katzung BG, Basic and Clinical Pharmacology, 8th ed., Lange Medical Books/McGraw-Hill, United States, 2001.
Kerr J.F., Wyllie A.H. and Currie A.R. (1972). Apoptosis: a basic biological phenomenon with wide-ranging implications in tissue kinetics. Br. J. Cancer 26, 239.

Kerr KM and Lamb D, Actual growth rate and tumour cell proliferation in human pulmonary neoplasms, Br J Cancer (1984) 50(3):343-349.

Kimura N, Shibuya T, Niho Y, Nakamura H, Matsuo S, Imamura T, Miyamoto N, Yanase T. Human lung cancer cell line (KSNY) producing colony-stimulating activity which affects both human and mouse marrow cells. Gan. 1979 Dec;70(6):807-10.

Koksai D, Demirag F, Bayiz H, Ozmen O, Tatci E, Berktaş B, Aydoğdu K, Yekeler E. The correlation of SUVmax with pathological characteristics of primary tumour and the value of Tumour/ Lymph node SUVmax ratio for predicting metastasis to lymph nodes in resected NSCLC patients. J Cardiothorac Surg. 2013 Apr 4;8:63. doi: 10.1186/1749-8090-8-63.

Kolokotroni E.A., D.D.Dionysiou, N.K.Uzunoglu, G.S.Stamatakis, “Studying the growth kinetics of untreated clinical tumours by using an advanced discrete simulation model”, Mathematical and Computer Modelling 54, Issues 9-10, pp. 1989-2006, 2011. doi:10.1016/j.mcm.2011.05.007

Kolokotroni, E. A., Stamatakis, G. S., Dionysiou, D. D., Georgiadi, E. Ch., Desmedt, C., Graf, N.M., 2008. Translating Multiscale Cancer Models into Clinical Trials: Simulating Breast Cancer Tumour Dynamics within the Framework of the “Trial of Principle” Clinical Trial and the ACGT Project. Proc. 8th IEEE International Conference on Bioinformatics and Bioengineering (BIBE 2008), Athens, Greece, 8-10 Oct. 2008. IEEE Catalog Number: CFP08266, ISBN: 978-1-4244-2845-8, Library of Congress: 2008907441, Paper No. BE-2.1.1, length: 8 pages (in electronic format) 2008..

Komaki R., Fujii T., Perkins P., Ro J.Y., Allen P.K., Mason K.A., Mountain C.F. and Milas L. (1996). Apoptosis and mitosis as prognostic factors in pathologically staged N1 nonsmall cell lung cancer. Int. J. Rad. Oncol. Biol. Phys. 36, 601-605

Kroep JR, Giaccone G, Tolis C, Voorn DA, Loves WJ, Groeninger CJ, Pinedo HM, Peters GJ. Sequence dependent effect of paclitaxel on gemcitabine metabolism in relation to cell cycle and cytotoxicity in non-small-cell lung cancer cell lines. Br J Cancer. 2000 Oct;83(8):1069-76.

Langendijk H, Thunnissen E, Arends JW, de Jong J, ten Velde G, Lamers R, Guinee D, Holden J, Wouters M. Cell proliferation and apoptosis in stage III inoperable non-small cell lung carcinoma treated by radiotherapy. *Radiother Oncol.* 2000 Aug;56(2):197-207.

Lee TK, Horner RD, Silverman JF, Chen YH, Jenny C, Scarantino CW. Morphometric and morphologic evaluations in stage III non-small cell lung cancers. Prognostic significance of quantitative assessment of infiltrating lymphoid cells. *Cancer.* 1989 Jan 15;63(2):309-16.

Lelle RJ, Heidenreich W, Stauch G and Gerdes J, The correlation of growth fractions with histologic grading and lymph node status in human mammary carcinoma, *Cancer* (1987) 59:83-88.

Li J, Yang H, Chen L, Li Y, Zhu Y, Dai Y, Chen K, Ai J, Zeng T, Mao X, Liu L, Li X, Guan XY. Establishment and characterization of human non-small cell lung cancer cell lines. *Mol Med Rep.* 2012 Jan;5(1):114-7. doi: 10.3892/mmr.2011.613. Epub 2011 Oct 3.

Lieber M, Smith B, Szakal A, Nelson-Rees W, Todaro G. A continuous tumour-cell line from a human lung carcinoma with properties of type II alveolar epithelial cells. *Int J Cancer.* 1976 Jan 15;17(1):62-70.

Lindell RM, Hartman TE, Swensen SJ, Jett JR, Midthun DE, Tazelaar HD, and Mandrekar JN, Five-year lung cancer screening experience: CT appearance, growth rate, location, and histologic features of 61 lung cancers, *Radiology* (2007) 242:555–562.

Liu C, Tsao MS. Proto-oncogene and growth factor/receptor expression in the establishment of primary human non-small cell lung carcinoma cell lines. *Am J Pathol.* 1993 Feb;142(2):413-23.

Loh PM, Clamon GH, Robinson RA, White ML, Hukku B, Rossi NP, Peterson WD, Establishment and characterization of four new human non-small cell lung cancer cell lines. *Cancer Res.* 1984 Aug;44(8):3561-9.

Mackintosh JA, Marshall HM, Yang IA, Bowman RV, Fong KM. A retrospective study of volume doubling time in surgically resected non-small cell lung cancer. *Respirology.* 2014 Jul;19(5):755-62. doi: 10.1111/resp.12311. Epub 2014 May 6.

Mackintosh JA, Marshall HM, Yang IA, Bowman RV, Fong KM. A retrospective study of volume doubling time in surgically resected non-small cell lung cancer. *Respirology.* 2014 Jul;19(5):755-62. doi: 10.1111/resp.12311. Epub 2014 May 6.

Masuda N, Fukuoka M, Takada M, Kudoh S, Kusunoki Y. Establishment and characterization of 20 human non-small cell lung cancer cell lines in a serum-free defined medium (ACL-4). *Chest.* 1991 Aug;100(2):429-38.

Merrill GF. 1998. Cell synchronization. *Methods Cell Biol* 57: 229–249.

Mini E, Nobili S, Caciagli B, Landini I, Mazzei T. Cellular pharmacology of gemcitabine. *Ann Oncol.* 2006 May;17 Suppl 5:v7-12.

Murai T, Shibamoto Y, Baba F, Hashizume C, Mori Y, Ayakawa S, Kawai T, Takemoto S, Sugie C, Ogino H. Progression of non-small-cell lung cancer during the interval before stereotactic body radiotherapy. *Int J Radiat Oncol Biol Phys.* 2012 Jan 1;82(1):463-7. doi: 10.1016/j.ijrobp.2010.10.001. Epub 2010 Nov 20.

Olsson L, Sorensen HR, Behnke O. Intratumoural phenotypic diversity of cloned human lung tumour cell lines and consequences for analyses with monoclonal antibodies. *Cancer.* 1984 Nov 1;54(9):1757-65.

O'Neill AJ, Staunton MJ, Gaffney EF. Apoptosis occurs independently of bcl-2 and p53 over-expression in non-small cell lung carcinoma. *Histopathology.* 1996 Jul;29(1):45-50.

Ormerod MG, Orr RM, Peacock JH, The role of apoptosis in cell killing by cisplatin: a flow cytometric study, *Br J Cancer.* 1994 Jan;69(1):93-100.

Park SY, Lee HS, Jang HJ, Lee GK, Chung KY, Zo JI. Tumour necrosis as a prognostic factor for stage IA non-small cell lung cancer. *Ann Thorac Surg*. 2011 Jun;91(6):1668-73. doi: 10.1016/j.athoracsur.2010.12.028.

Peng Huang and William Plunkett, 'Fludarabine- and gemcitabine-induced apoptosis: incorporation of analogs into DNA is a critical event' *Cancer Chemother Pharmacol* (1995) 36:181-188

Perry MC (Ed.), *The Chemotherapy Source Book*, 3rd ed., Lippincott Williams and Wilkins, Philadelphia, 2001.
Proskuryakov SY, Gabai VL. Mechanisms of tumour cell necrosis. *Curr Pharm Des*. 2010 Jan;16(1):56-68.

Quint LE, Cheng J, Schipper M, Chang AC and Kalemkerian G, Lung lesion doubling times: values and variability based on method of volume determination, *Clin Radiol* (2008) 63(1):41-48.

Retsky M. W., D. E. Swartzendruber, R. H. Wardwell, P. D. Bame, Is gompertzian or exponential kinetics a valid description of individual human cancer growth?, *Med. Hypotheses* 33 (1990) 95–106

Ribba, B., Colin, T., Schnell, S., 2006. A multiscale mathematical model of cancer, and its use in analyzing irradiation therapies. *Theor. Biol. Med. Model.* 3:7, doi:10.1186/1742-4682-3-7.

Rigau V, Molina TJ, Chaffaud C, Huchon G, Audouin J, Chevret S, Bréchet JM. Blood vessel invasion in resected non small cell lung carcinomas is predictive of metastatic occurrence. *Lung Cancer*. 2002 conNov;38(2):169-76.

Rudolph P, Peters J, Lorenz D, Schmidt D and Parwaresch R, Correlation between mitotic and Ki-67 labeling indices in paraffin-embedded carcinoma specimens, *Hum Pathol* (1998) 29(11):1216-1222.

Ruiz van Haperen VW, Veerman G, Vermorken JB, Peters GJ. 2',2'-Difluoro-deoxycytidine (gemcitabine) incorporation into RNA and DNA of tumour cell lines. *Biochem Pharmacol*. 1993 Aug 17;46(4):762-6.

Saintigny P, Kambouchner M, Ly M, Gomes N, Sainte-Catherine O, Vassy R, Czernichow S, Letoumelin P, Breau JL, Bernaudin JF, Kraemer M. Vascular endothelial growth factor-C and its receptor VEGFR-3 in non-small-cell lung cancer: concurrent expression in cancer cells from primary tumour and metastatic lymph node. *Lung Cancer*. 2007 Nov;58(2):205-13. Epub 2007 Aug 7.

Salmon, S.E., Sartorelli, A.C., 2001. Cancer Chemotherapy. In: Katzung, B.G. (Eds.), *Basic & Clinical Pharmacology*. Lange Medical Books/McGraw-Hill: International Edition, pp. 923-1044.

Sedletska, Y.; Giraud-Panis, M.J.; Malinge, J.M. Cisplatin is a DNA-damaging antitumour compound triggering multifactorial biochemical responses in cancer cells: importance of apoptotic pathways. *Curr. Med. Chem. Anticancer Agents* 2005, 5, 251–265.

Sell S., Stem cell origin of cancer and differentiation therapy, *Crit. Rev. Oncol. Hematol.* 51 (2004) 1–28.
Sergey Y. Proskuryakov and Vladimir L. Gabai. Mechanisms of Tumour Cell Necrosis *Current Pharmaceutical Design*, 2010, 16, 56-68

Siddik, Zahid H. "Cisplatin: mode of cytotoxic action and molecular basis of resistance." *Oncogene* 22 (2003): 7265–7279.

Singh S, Bora-Singhal N, Kroeger J, Laklai H, Chellappan SP. β Arrestin-1 and Mcl-1 modulate self-renewal growth of cancer stem-like side-population cells in non-small cell lung cancer. *PLoS One*. 2013;8(2):e55982. doi: 10.1371/journal.pone.0055982. Epub 2013 Feb 13.

Spratt JS, Spjut HJ and Roper CL, The frequency distribution of the rates of growth and the estimated duration of primary pulmonary carcinomas, *Cancer* (1963) 16:687–693.

G.S. Stamatakos, D.D. Dionysiou, E.I. Zacharaki, N.A. Mouravliansky, K.S.Nikita, N.K. & Uzunoglu , In silico radiation oncology: combining novel simulation algorithms with current visualization techniques , IEEE Proceedings: Special Issue on Bioinformatics: Advances and Challenges , 90(11) , 1764-1777 , 2002

Stamatakos G.S., Kolokotroni E.A., Dionysiou D.D., Georgiadi E.C., Desmedt C., An advanced discrete state-discrete event multiscale simulation model of the response of a solid tumour to chemotherapy: Mimicking a clinical study. J Theor Biol. 266(1) (2010) 124–139.

G.Stamatakos "In Silico Oncology Part I: Clinically Oriented Cancer Multilevel Modeling Based on Discrete Event Simulation" In T.Deisboeck and G. Stamatakos Eds 407-436 2011-01-01 CRC Press, Print ISBN: 978-1-4398-1440-6 eBook ISBN: 978-1-4398-1442-0 DOI: 10.1201/b10407-19 Boca Raton, Florida, USA, 2011

G.S.Stamatakos, E.Ch.Georgiadi, N.Graf, E.A.Kolokotroni, and D.D.Dionysiou, "Exploiting Clinical Trial Data Drastically Narrows the Window of Possible Solutions to the Problem of Clinical Adaptation of a Multiscale Cancer Model", PLOS ONE 6(3), e17594, 2011

G Stamatakos, IEEE , D Dionysiou, A Lunzer, R Belleman, E Kolokotroni, E Georgiadi, M Erdt, J Pukacki, S Rueping, S Giatili, A d'Onofrio, S Sfakianakis, K Marias, C Desmedt, M Tsiknakis, and N Graf, "The Technologically Integrated Oncosimulator: Combining Multiscale Cancer Modeling with Information Technology in the In Silico Oncology Context" DOI:10.1109/JBHI.2013.2284276 IEEE J Biomedical and Health Informatics vol.18, No. 3, pp.840-854 2014

Stammler G. and Volm M. (1996). Apoptosis in non-small cell lung cancer as related to drug resistance and prognosis. Apoptosis 1, 95- 99.

Steel 1977, In Steel (Editor), Basic Clinical Radiobiology, 3rd ed., Arnold, London, 2002.

Steel, G.G. 1997. Clonogenic cells and the concept of cell survival. In: Steel, G.G. (Ed.), Basic Clinical Radiobiology, second ed. Arnold: London, UK.

Takahashi S, Kamata Y, Tamo W, Koyanagi M, Hatanaka R, Yamada Y, Tsushima T, Takaya S and Fukuda I, Relationship between postoperative recurrence and expression of cyclin E, p27, and Ki-67 in non-small cell lung cancer without lymph node metastases, Int J Clin Oncol (2002) 7(6):349-55.

Tanaka F, Kawano Y, Li M, Takata T, Miyahara R, Yanagihara K, Ohtake Y, Fukuse T, Wada H. Prognostic significance of apoptotic index in completely resected non-small-cell lung cancer. J Clin Oncol. 1999 Sep;17(9):2728-36.

Tolis C, Peters GJ, Ferreira CG, Pinedo HM, Giaccone G. Cell cycle disturbances and apoptosis induced by topotecan and gemcitabine on human lung cancer cell lines. Eur J Cancer. 1999 May;35(5):796-807.

Törmänen U, Eerola AK, Rainio P, Vähäkangas K, Soini Y, Sormunen R, Bloigu R, Lehto VP, Pääkkö P. Enhanced apoptosis predicts shortened survival in non-small cell lung carcinoma. Cancer Res. 1995 Dec 1;55(23):5595-602.

Tsoli E, Gorgoulis VG, Zacharatos P, Kotsinas A, Mariatos G, Kastrinakis NG, Kokotas S, Kanavaros P, Asimacopoulos P, Bramis J, Kletsas D, Papavassiliou AG, Kittas C. Low levels of p27 in association with deregulated p53-pRb protein status enhance tumour proliferation and chromosomal instability in non-small cell lung carcinomas. Mol Med. 2001 Jun;7(6):418-29.

Tsubochi H, Sato N, Hiyama M, Kaimori M, Endo S, Sohara Y, *et al.* Combined analysis of cyclooxygenase-2 expression with p53 and Ki-67 in nonsmall cell lung cancer. Ann Thorac Surg 2006;82(4):1198–204.

Usuda K, Saito Y, Sagawa M, Sato M, Kanma K, Takahashi S, Endo C, Chen Y, Sakurada A and Fujimura S, Tumour doubling time and prognostic assessment of patients with primary lung cancer, *Cancer* (1994) 74:2239–2244.

Vakifahmetoglu H, Olsson M, Tamm C, Heidari N, Orrenius S, Zhivotovsky B. DNA damage induces two distinct modes of cell death in ovarian carcinomas. *Cell Death Differ* 2008; 15: 555–566.

van de Vaart PJ, Belderbos J, de Jong D, Sneeuw KC, Majoor D, Bartelink H, Begg AC. DNA-adduct levels as a predictor of outcome for NSCLC patients receiving daily cisplatin and radiotherapy. *Int J Cancer*. 2000 Mar 20;89(2):160-6.

Visvader J.E., G.J. Lindeman, Cancer stem cells in solid tumours: accumulating evidence and unresolved questions, *Nat. Rev. Cancer* 8 (10) (2008) 755-768.

Wang G, Reed E, Li QQ., Molecular basis of cellular response to cisplatin chemotherapy in non-small cell lung cancer (Review)., *Oncol Rep*. 2004 Nov;12(5):955-65.

Warth A, Cortis J, Soltermann A, Meister M, Budczies J, Stenzinger A, Goeppert B, Thomas M, Herth FJ, Schirmacher P, Schnabel PA, Hoffmann H, Dienemann H, Muley T, Weichert W. Tumour cell proliferation (Ki-67) in non-small cell lung cancer: a critical reappraisal of its prognostic role. *Br J Cancer*. 2014 Sep 9;111(6):1222-9. doi: 10.1038/bjc.2014.402. Epub 2014 Jul 22.

Winer-Muram HT, Jennings SG, Tarver RD, Aisen AM, Tann M, Conces DJ and Meyer CA, Volumetric growth rate of stage I lung cancer prior to treatment: serial CT scanning, *Radiology* (2002) 223:798–805.

Zhang X, Fang B, Mohan R, Chang JY. Cocksackie-adenovirus receptor as a novel marker of stem cells in treatment-resistant non-small cell lung cancer. *Radiother Oncol*. 2012 Nov;105(2):250-7. doi: 10.1016/j.radonc.2012.09.002. Epub 2012 Sep 27.

T6. Description of the (pure) Tumour Growth and Response to Treatment Component Model (T) through the 13 Perspectives

TABLE "T-13P" (FIRST PART)		
PERSPECTIVE CODE NUMBER	PERSPECTIVE TITLE	PERSPECTIVE VALUE(S)
I	TUMOUR-AFFECTED NORMAL TISSUE MODELLING	tumour normal tissue
II	SPATIAL SCALE(S) OF THE MANIFESTATION OF LIFE	cellular tissue organ body system
III	TEMPORAL SCALE(S) OF THE MANIFESTATION OF LIFE	h d
IV	BIOMECHANISM(S) ADDRESSED	cell cycling stem cell division progenitor cell division apoptosis necrosis metabolism chemotherapy cell kill radiotherapy cell kill volume growth volume shrinkage
V	TUMOUR TYPE(S) ADDRESSED	lung cancer other solid tumours
VI	TREATMENT MODALITY(-IES) ADDRESSED	chemotherapy radiotherapy targeted therapy

TABLE "T-13P (SECOND PART)		
PERSPECTIVE CODE NUMBER	PERSPECTIVE TITLE	PERSPECTIVE VALUE(S)
VII	GENERIC CANCER BIOLOGY – CLINICALLY DRIVEN CHARACTER OF THE MODELLING APPROACH	generic cancer biology clinically driven
VIII	ORDER OF ADDRESSING DIFFERENT SPATIAL SCALES	top-down bottom-up
IX	ORDER OF ADDRESSING DIFFERENT TEMPORAL SCALES	short periods → longer periods
X	MECHANISTIC-STATISTICAL CHARACTER OF THE MODELLING APPROACH	mechanistic
XI	DETERMINISTIC-STOCHASTIC CHARACTER OF THE MODELLING APPROACH	deterministic stochastic
XII	CONTINUOUS-FINITE-DISCRETE CHARACTER OF THE MATHEMATICS INVOLVED	discrete
XIII	CLOSED FORM SOLUTION – ALGORITHMIC SIMULATION MODELLING APPROACH	algorithmic simulation

A. The Vascular/Angiogenesis Component Model

A1. Introduction

A suitable form for the University of Oxford (UOXF) vasculature hypomodel for the lung cancer clinical case was decided at the 3rd WP6 modellers' meeting (05/11/14, Athens). It was broadly identified that the model should take an angiogenic stimulus as input and return a vessel density or volume fraction as an output. In particular, it was identified that the vasculature hypomodel should interface with the tumour growth and response to treatment hypomodel developed at ICCS and potentially subcellular models developed at FORTH. Further details are contained in the meeting minutes document.

The integration strategy for the vasculature hypomodel is shown in Fig. A1.

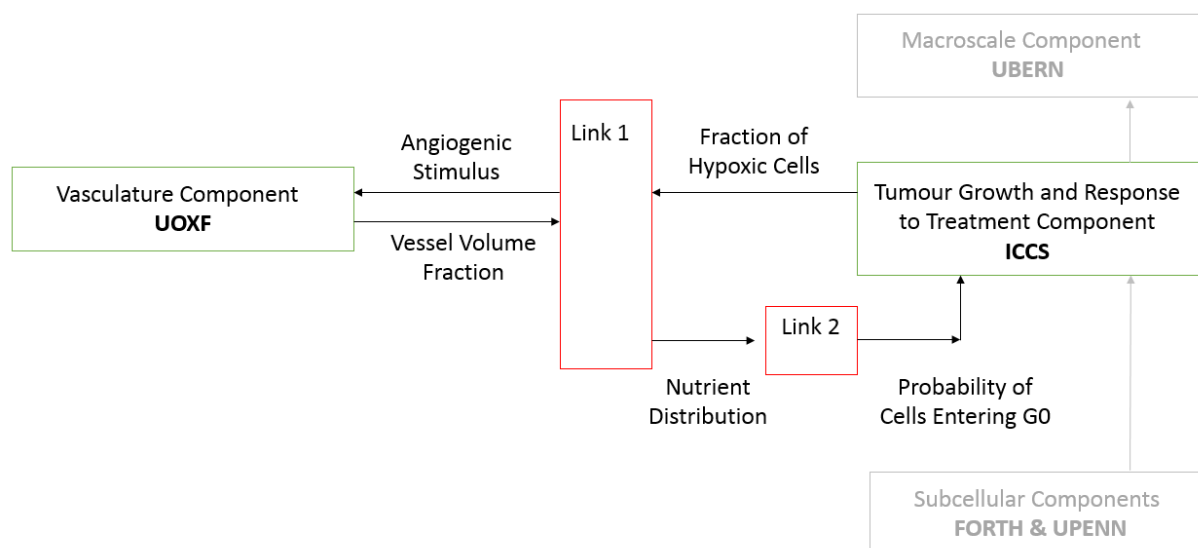


Fig. A1 Integration strategy for the vasculature hypomodel.

The linking components shown in Fig. A1 require further discussion between UOXF, ICCS and FORTH, however an example of Link 1 is included in this report, primarily for the purpose of demonstrating and testing the integration scenarios for the vasculature component. Link 2 might be handled by a molecular level metabolic network model being developed by FORTH, which could provide proliferation rates to the ICCS component based on input nutrient concentrations. However, the metabolic component is not considered necessary but rather a possible refinement, due to the fact that metabolism is grossly addressed by the pure tumour growth component model.

As will be discussed subsequently the vasculature update rules used in the presented component model are highly simplified. This is due to the limited information concerning the vasculature available for the specific clinical case of lung cancer (namely CT, histology, molecular data and treatment schedule). In developing the presented component particular attention has therefore been given to developing software where: i) the vasculature update rule can be easily modified,

which will be relevant for adapting to available data in subsequent clinical cases, and ii) integration with partner codes is straightforward.

A2. Hypomodel Description

A schematic of the vasculature hypomodel is shown in Fig. A2. The model takes a domain geometry, time step size and a spatial distribution of angiogenic stimulus as input and returns a spatial distribution of vessel volume fractions. Given that the vasculature hypomodel communicates with the ICCS tumour growth model, as shown in Fig. A1, the domain geometry is discretized into equidistant points, corresponding to the Geometric Cell (GC) discretization of the ICCS model. The ICCS model is described in further detail in Stamatakis et al. (2010).

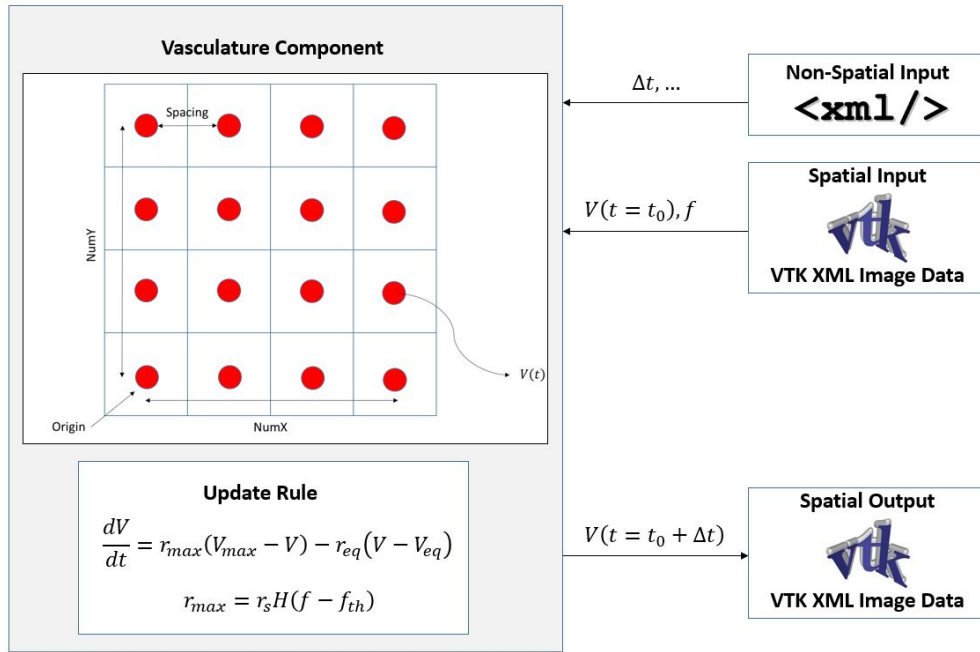


Fig. A2 Schematic of the vasculature component model. Further details on the input file format are given in Fig. A3.

At each point the dimensionless vessel volume fraction (V) is updated through time (t) according to:

$$\frac{dV}{dt} = r_{max}(V_{max} - V) - r_{eq}(V - V_{eq}) \quad (A1)$$

where V_{max} and V_{eq} are the maximum vascular volume fraction and equilibrium vascular volume fraction. The parameters r_{max} and r_{eq} control the rates at which the corresponding volume fractions are approached.

In the subsequent testing of the presented hypomodel the rate parameter r_{max} is taken as a function of the concentration of a growth factor f , representing a diffusible angiogenic stimulus. However it can also be a function of other inputs, such as anti-angiogenic drug concentration. The particular form of the growth factor dependence used in the testing is:

$$r_{max} = r_s H(f - f_{th}) \quad (A2)$$

where r_s is a parameter controlling the rate at which maximum vessel volume fraction is approached in the presence of angiogenic stimulus, H is the Heaviside step function and f and f_{th} are respective growth factor concentration and threshold concentration above which vascular volume fraction increases. Within the tested implementation Eqn. (A1) is updated using a forward difference time integration rule, although it is noted that for this simple case it could be solved analytically. Table A-1 lists the component model parameters and dimensions.

TABLE A-1. LIST OF INPUT AND OUTPUT PARAMETERS FOR THE VASCULATURE COMPONENT MODEL

Parameter	Description	I/O Format	Dimension
$V(t = t_0)$	Input vessel volume fraction	Input: Spatial / VTK	None
N	Number of time steps	Input: Non-spatial / XML	None
Δt	Time increment	Input: Non-spatial / XML	T
V_{max}	Maximum vessel volume fraction	Input: Non-spatial / XML	None
V_{eq}	Equilibrium vessel volume fraction	Input: Non-spatial / XML	None
r_{eq}	Equilibrium rate parameter	Input: Non-spatial / XML	T^{-1}
r_s	Stimulus rate parameter	Input: Non-spatial / XML	T^{-1}
f	Growth factor concentration	Input: Spatial / VTK	Arbitrary provided it is the same as f_{th} dimension
f_{th}	Threshold growth factor concentration	Input: Non-spatial / XML	Arbitrary provided it is the same as f dimension
$V(t = t_0 + N\Delta t)$	Output vessel volume fraction	Output: Spatial / VTK	None

As discussed, the vasculature update rules in Eqns. (A1) and (A2) and time integration rule used are highly simplified. However they can be easily updated in the vasculature component code, as may be required when considering clinical cases with more detailed information on the vasculature. In particular, it has been verified that Systems Biology Markup Language (SBML) readers (libsbml, Bornstein et al. (2008)) and solvers (libsbmlsim, Takizawa et al. (2013)) can be integrated within the presented code through their respective Python APIs. This would allow more general vasculature update and time integration rules to be specified as model input, without needing to know the details of the simulation code itself. Examples of alternate update rules are those of Hardnfeldt et al. (1999), Poleszczuk et al. (2011) and Hubbard and Byrne (2013).

The parameters used in the presented model, although defined in terms of potentially measurable quantities, are unlikely to be directly determined based on the available lung cancer clinical data. A more indirect determination based on knowledge of tumour shape evolution and combination with the ICCS tumour growth code may be necessary.

The model is coded in Python and can be run in three ways; i) as a standalone script, ii) as a Python module as part of a parent code and iii) as a co-execution. Methods (i) and (ii) are demonstrated in this report while method (iii) is under-going testing and may require further discussion with partners involved in wrapper development. When used as a standalone script the model uses an XML input file format for non-spatial parameter information (shown in Fig. A3) and a VTK XML image data format for spatial parameter information. The latter format was chosen due to its ubiquity in transferring and viewing spatial scientific data. The script outputs a vessel volume fraction distribution at a specified frequency in the form of VTK XML image data.

```
<simulation>
<name>VasculatureSimulation</name>
<numSteps>100</numSteps>
<timeIncrement>0.1</timeIncrement>
<outputFrequency>10</outputFrequency>
<grid>
<spacing>1.0</spacing>
<numX>3</numX>
<numY>3</numY>
<numZ>2</numZ>
</grid>
<parameters>
<vMax>1.0</vMax>
<vEq>0.5</vEq>
<rMax>0.1</rMax>
<rEq>0.1</rEq>
</parameters>
<initialConditionFile></initialConditionFile>
<coexecutionFile></coexecutionFile>
<coexecutionWait>100.0</coexecutionWait>
</simulation>
```

Fig. A3 Sample input file for non-spatial parameters in the vasculature component model.

Fig. A4 shows sample results for a standalone run of the vasculature component for 2D and 3D cases. A constant distribution of growth factor is specified and an initial vessel density (or volume fraction) of 0.1. It can be seen in Fig. A4 that vessel density reaches an equilibrium value (V_{eq}) of 0.5 in regions where the factor concentration is less than the specified threshold value (f_{th}) of 0.5 and a higher value of 0.75 elsewhere.

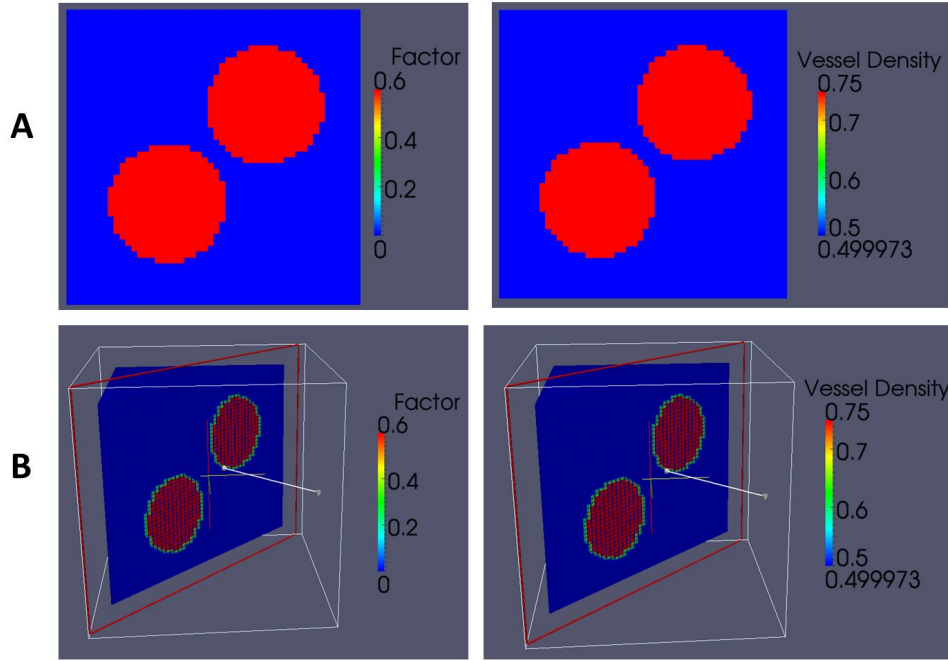


Fig. A4 Sample simulation results showing input growth factor distributions and resulting vessel density distributions for (A) 2D and (B) 3D domains.

A3. Standalone Testing

For a given growth factor distribution the simple evolution models in Eqn. (A1) can be written analytically at a point as:

$$V(t) = \begin{cases} (V_{eq} - (V_{eq} - V_0)e^{-r_{eq}t}), & f < f_{th}, t > 0; \\ \frac{r_s(V_{max} - (V_{max} - V_0)e^{-(r_s+r_{eq})t}) + r_{eq}(V_{eq} - (V_{eq} - V_0)e^{-(r_s+r_{eq})t})}{(r_s + r_{eq})}, & f \geq f_{th}, t > 0 \end{cases} \quad (A3)$$

where V_0 is the vessel volume fraction at $t = 0$. As is evident in Eqn. (A3) the model will give values of V between 0 and V_{max} provided that at least one of r_s and r_{eq} are given and that these rate parameters have positive values. For the case of the growth factor concentration passing through the threshold at time $t = t_1$ the concentration is given as:

$$V(t) = \begin{cases} (V_{eq} - (V_{eq} - V_0)e^{-r_{eq}t}), & 0 < t < t_1; \\ \frac{r_s(V_{max} - (V_{max} - A)e^{-(r_s+r_{eq})(t-t_1)}) + r_{eq}(V_{eq} - (V_{eq} - A)e^{-(r_s+r_{eq})(t-t_1)})}{(r_s + r_{eq})}, & t \geq t_1 \end{cases} \quad (A4)$$

where:

$$A = (V_{eq} - (V_{eq} - V_0)e^{-r_{eq}t_1}) \quad (A5)$$

It is noted that this function is continuous at $t = t_1$.

To test the overall implementation of the vasculature component the model's predicted average vessel volume fraction over the whole spatial domain is compared to the analytical result in Eqn. (A3) for cases with growth factor concentration above and below the specified threshold. Results are shown in Fig. A5.A for a case with V_0 of 0.05 and $f > f_{th}$ and in Fig. A5.B for a case with V_0 of 0.95 and $f < f_{th}$ with a time step of 0.1T. In addition to the analytical model the results of a stand-alone numerical integration of Eqn. (A1) are also included in Fig. A5 to account for differences due to errors introduced in using the forward difference scheme.

It is noted that the primary purpose of this test is to demonstrate the performance of the code as a whole, given that during a simulation data is exchanged between a number of formats and external libraries. The presented testing is not intended to characterise the behaviour of the time integration scheme, which may require modification depending on eventual values of input parameters used.

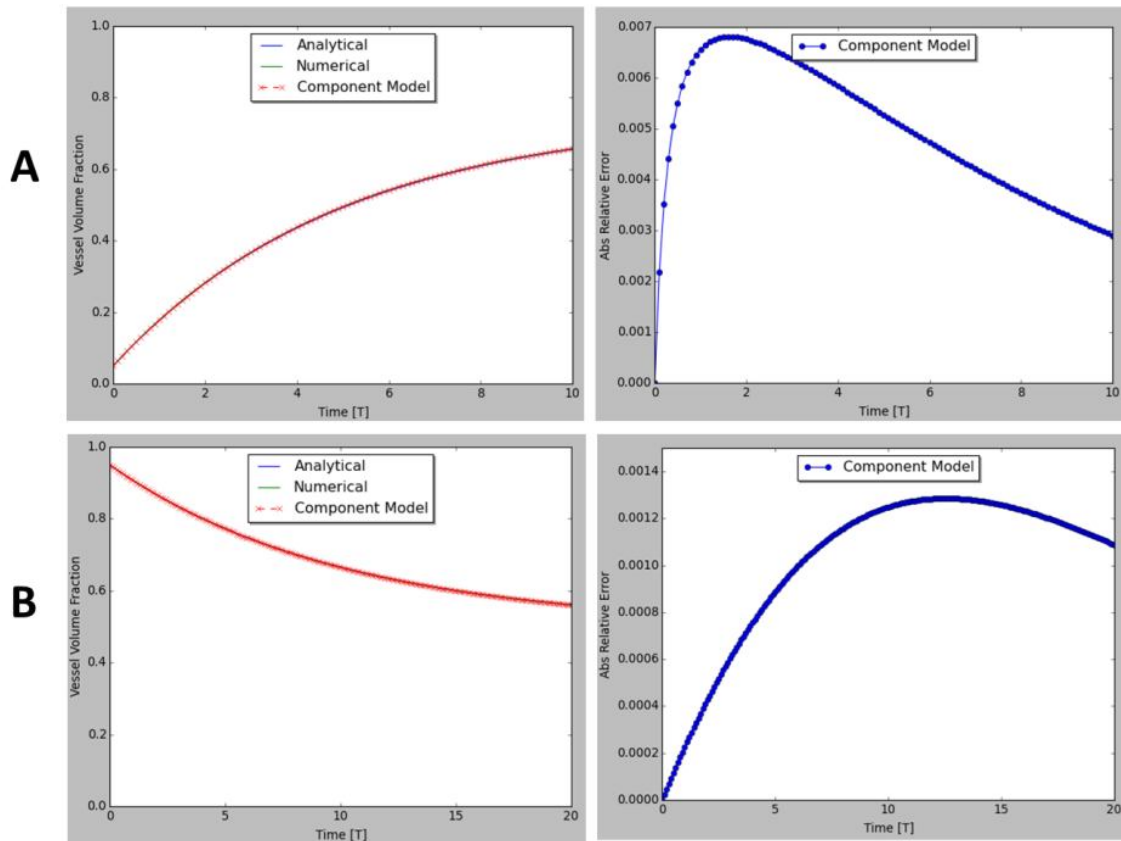


Fig. A5 Comparisons between Eqn. (A3) (Analytical), a stand-alone numerical integration (Numerical) and the component model predictions for two sets of parameter values (A) and (B). Absolute values of relative error are between the Analytical and Component Model solutions.

A4. Integration

Fig. A1 shows the integration of the vasculature hypomodel in the lung cancer hypermodel framework. To test the integration of the vasculature component simple versions of the Link 1 component and the ICCS component were developed. Fig. A6 shows a schematic of the models. The components are each written in Python and the hypermodel can be executed by running each component individually for each time step and exchanging data through VTK files or through importing each as a Python module and exchanging data in memory. A third mechanism in which each component executes concurrently and communicates through file updates and listeners using the Python 'watchdog' package (<https://pypi.python.org/pypi/watchdog>) has been coded but not yet fully tested.

The operation of these additional components is described in brief here, however it is noted that they have not yet been fully tested and shown results are only to demonstrate the ability of the different components to communicate. The chemical component takes a vessel volume fraction (V) from the vasculature component and fractions of proliferating (P) and quiescent (G_0) cells from the cell component. A steady-state distribution of nutrient (e.g. oxygen) (c) is then calculated in the domain according to:

$$D_c \nabla^2 c - \lambda c(P + G_0) + \rho V(c_{vess} - c) = 0 \quad (A6)$$

where D_c is the diffusivity of the nutrient, λ is a constant reflecting the rate of consumption of nutrients by cells, ρ is a constant related to vessel permeability and c_{vess} is the concentration of nutrient in the vessels. Reaction-diffusion equations of this type are widely used in the literature for modelling nutrient delivery by vasculature and uptake by cells, for an example see Owen et al. (2009).

Similarly, a steady-state distribution of growth factor (f) can be calculated according to:

$$D_f \nabla^2 f + k(G_0) - \mu f = 0 \quad (A7)$$

where k is a constant controlling the rate of factor release by quiescent cells and μ is a rate of natural decay of the factor. This equation is similar to that used in Owen et al. (2009) for modelling extracellular concentrations of VEGF, however in this case uptake by the vasculature is neglected. The governing PDEs are solved using the FEniCS finite element solver (Logg et al., 2012) in the chemical component.

The cell component takes the nutrient concentration (c) from the chemical component, which in turn controls rates of transition from cells in the M phase of their cycle to the G_0 phase and the rate of apoptosis. The cell cycle presented in Fig. A6 is solved in GCs corresponding exactly to those used in the vasculature component, however for the cell component if a critical cell density is reached its cells are redistributed to neighbouring GCs. The direction of transfer is determined using the distance to the tumour boundary, which serves as a simple approximation of likely pressure gradients. The cell cycle model used is a simplification of that of the ICCS component and again can be updated through the use of SBML definitions, in particular more detailed models such as those of Tyson and Novak (2001) or Alarcon et al. (2004) could be implemented here.

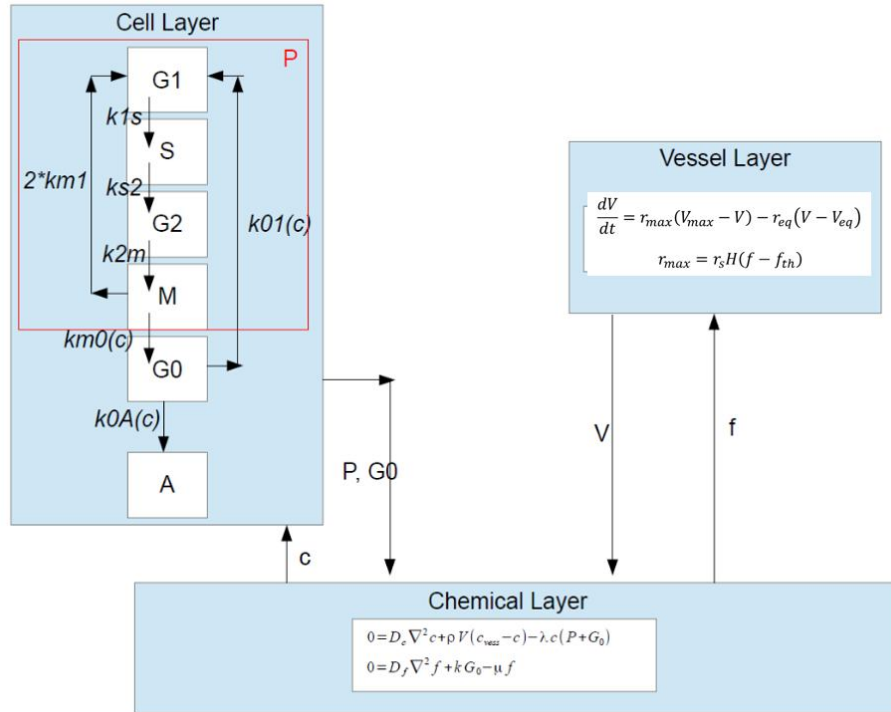


Fig. A6 Linking of the models developed for integration testing of the vasculature component.

Fig. A7 and Fig. A8 show the results of simulating the cell, vessel and chemical hypomodels concurrently, i.e. executing a hypermodel in 2D and 3D respectively. As shown in Fig. A7, cells are initially seeded in two circular regions with uniform initial distributions of vessels, nutrients and growth factors. As the simulation progresses the cell populations merge while vessel density increases in response to the release of growth factor. Dirichlet boundary conditions for nutrient and growth factor are imposed on the domain boundaries. Fig. A8 shows the evolution of a single cell population (tumour) and resulting development of regions with low tissue oxygenation and increased vessel density.

It is noted that the shown results are very much illustrative as the cell and chemical components have only been developed for the purposes of testing and demonstrating the integration of the vasculature component and are not thoroughly tested themselves. Further efforts will be required in linking the actual component models, in particular attention to data transfer and synchronisation of time-stepping will be important and challenging.

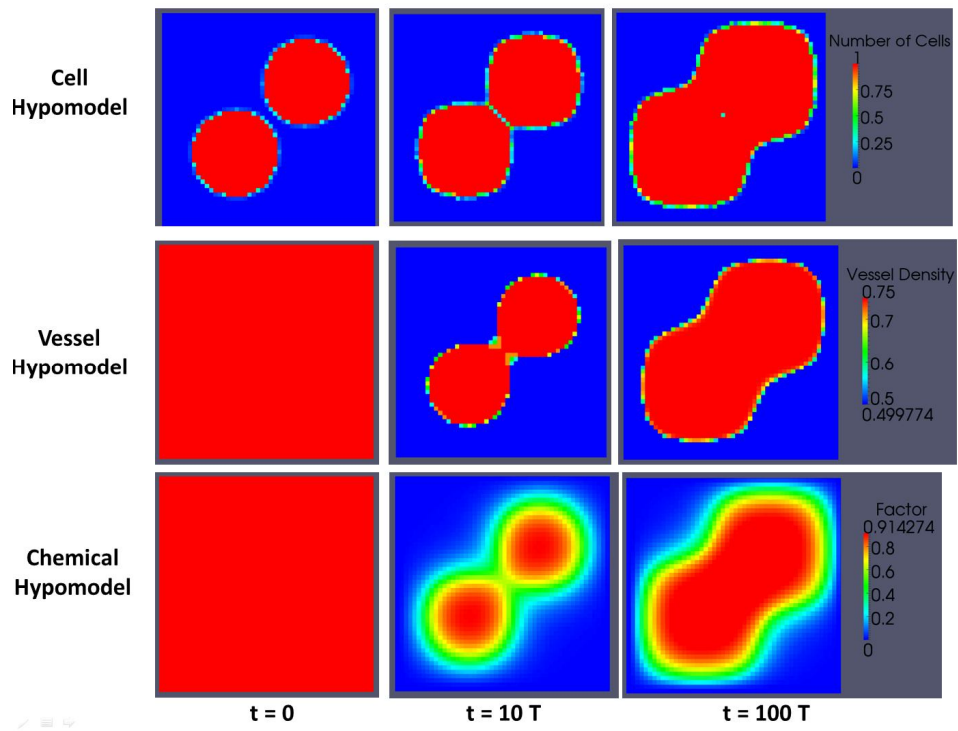


Fig. A7 Combined results for a concurrent execution of the cell, vessel and chemical hypomodels for a 2D case.

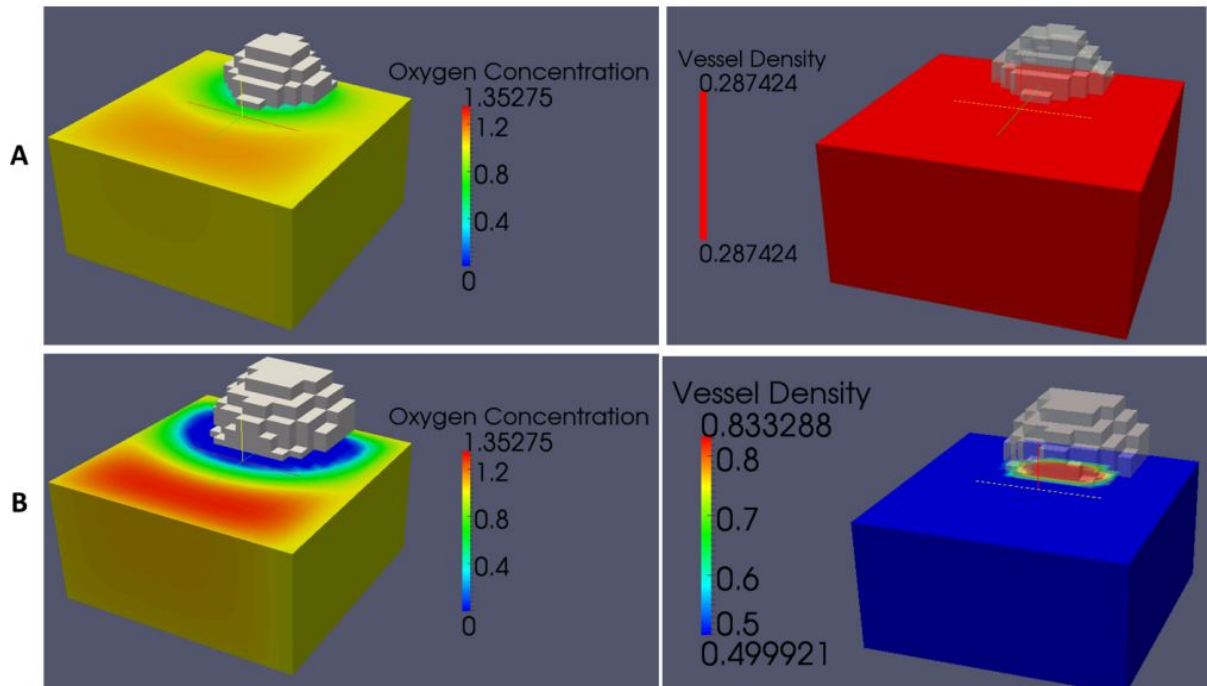


Fig. A8 Combined results for a concurrent execution of the cell, vessel and chemical hypomodels for a 3D case at: (A) $t = 10T$ and (B) $t = 100T$.

A5. Further Details

Model scripts and sample input and output files for the vasculature component are available for immediate use (contact grogan@maths.ox.ac.uk). The code is written in Python and uses only open source libraries. The cell and chemical component codes are also available, however further testing and development is required for both.

A6. References

- Alarcon, T., Byrne, H.M., Maini, P.K. (2004) A mathematical model of the effects of hypoxia on the cell-cycle of normal and cancer cells. *Journal of Theoretical Biology*, 229(3):395-411.
- Bornstein, B. J., Keating, S. M., Jouraku, A., Hucka, M. (2008) LibSBML: An API Library for SBML. *Bioinformatics*, 24(6):880–881.
- Hahnfeldt, P., Panigrahy, D., Folkman, J., Hlatky, L. (1999) Tumour development under angiogenic signaling: a dynamical theory of tumour growth, treatment response, and postvascular dormancy, *Cancer Res*, 59: 4770-4775.

Hubbard, M.E., Byrne, H.M. (2013) Multiphase modelling of vascular tumour growth in two spatial dimensions, *Journal of Theoretical Biology*, 316(7):70-89.

Logg A., Mardal K.A., Wells G.N. (2012) *Automated Solution of Differential Equations by the Finite Element Method*, Springer.

Owen, M.R., Alarcon, T., Maini, P.K., Byrne, H.M. (2009) Angiogenesis and vascular remodelling in normal and cancerous tissues, *Journal of Mathematical Biology*, 58:689-721.

Poleszczuk, J., Bodnar, M., Foryś, U. (2011) New approach to modelling of antiangiogenic treatment on the basis of Hahnfeldt et al. model, *Mathematical Biosciences and Engineering* 8(2):591-603.

Stamatakis, G.S., Kolokotroni, E.A., Dionysiou, D.D., Georgiadi, ECh., Desmedt, C. (2010) An advanced discrete state-discrete event multiscale simulation model of the response of a solid tumour to chemotherapy: Mimicking a clinical study. *Journal of Theoretical Biology*, 266(1):124-39.

Takizawa, H., Nakamura, K., Tabira, A., Chikahara, Y., Matsui, T., Hiroi, N., Funahashi, A. (2013) LibSBMLSim: a reference implementation of fully functional SBML simulator. *Bioinformatics*, 29(11), 1474–1476.

Tyson, J.J., Novak, B. (2001) Regulation of the eukaryotic cell cycle: molecular antagonism, hysteresis, and irreversible transitions. *Journal of Theoretical Biology*, 210(2):249-63.

A7. Description of the The Vascular/Angiogenesis Component Model (A) through the 13 Perspectives

TABLE "A-13P" (FIRST PART)		
PERSPECTIVE CODE NUMBER	PERSPECTIVE TITLE	PERSPECTIVE VALUE(S)
I	TUMOUR-AFFECTED NORMAL TISSUE MODELLING	tumour normal tissue
II	SPATIAL SCALE(S) OF THE MANIFESTATION OF LIFE	cellular tissue organ body system
III	TEMPORAL SCALE(S) OF THE MANIFESTATION OF LIFE	h d
IV	BIOMECHANISM(S) ADDRESSED	angiogenesis oxygenation metabolism
V	TUMOUR TYPE(S) ADDRESSED	lung cancer other solid tumours
VI	TREATMENT MODALITY(-IES) ADDRESSED	no treatment consideration

TABLE "A-13P" (SECOND PART)		
PERSPECTIVE CODE NUMBER	PERSPECTIVE TITLE	PERSPECTIVE VALUE(S)
VII	GENERIC CANCER BIOLOGY – CLINICALLY DRIVEN CHARACTER OF THE MODELLING APPROACH	generic cancer biology clinically driven
VIII	ORDER OF ADDRESSING DIFFERENT SPATIAL SCALES	bottom-up top-down
IX	ORDER OF ADDRESSING DIFFERENT TEMPORAL SCALES	short periods → longer periods
X	MECHANISTIC-STATISTICAL CHARACTER OF THE MODELLING APPROACH	mechanistic
XI	DETERMINISTIC-STOCHASTIC CHARACTER OF THE MODELLING APPROACH	deterministic
XII	CONTINUOUS-FINITE-DISCRETE CHARACTER OF THE MATHEMATICS INVOLVED	continuous finite (finitized continuous)
XIII	CLOSED FORM SOLUTION – ALGORITHMIC SIMULATION MODELLING APPROACH	algorithmic simulation

AA. An Alternative Vascular / Angiogenesis Component Model

AA1. Introduction

This section provides the overview of a hypo-model simulating vascular tumour growth under anti-angiogenic treatment that has been developed by (Poleszczuk et al. 2011) and extended via the inclusion of bevacizumab pharmacokinetics by (Argyri et al. 2012). The following figure illustrates the information flow inside the model simulating the antitumour effect of bevacizumab i.e. the most popular representative of the wider family of antiangiogenic agents in current clinical practice, on a vascularized tumour.

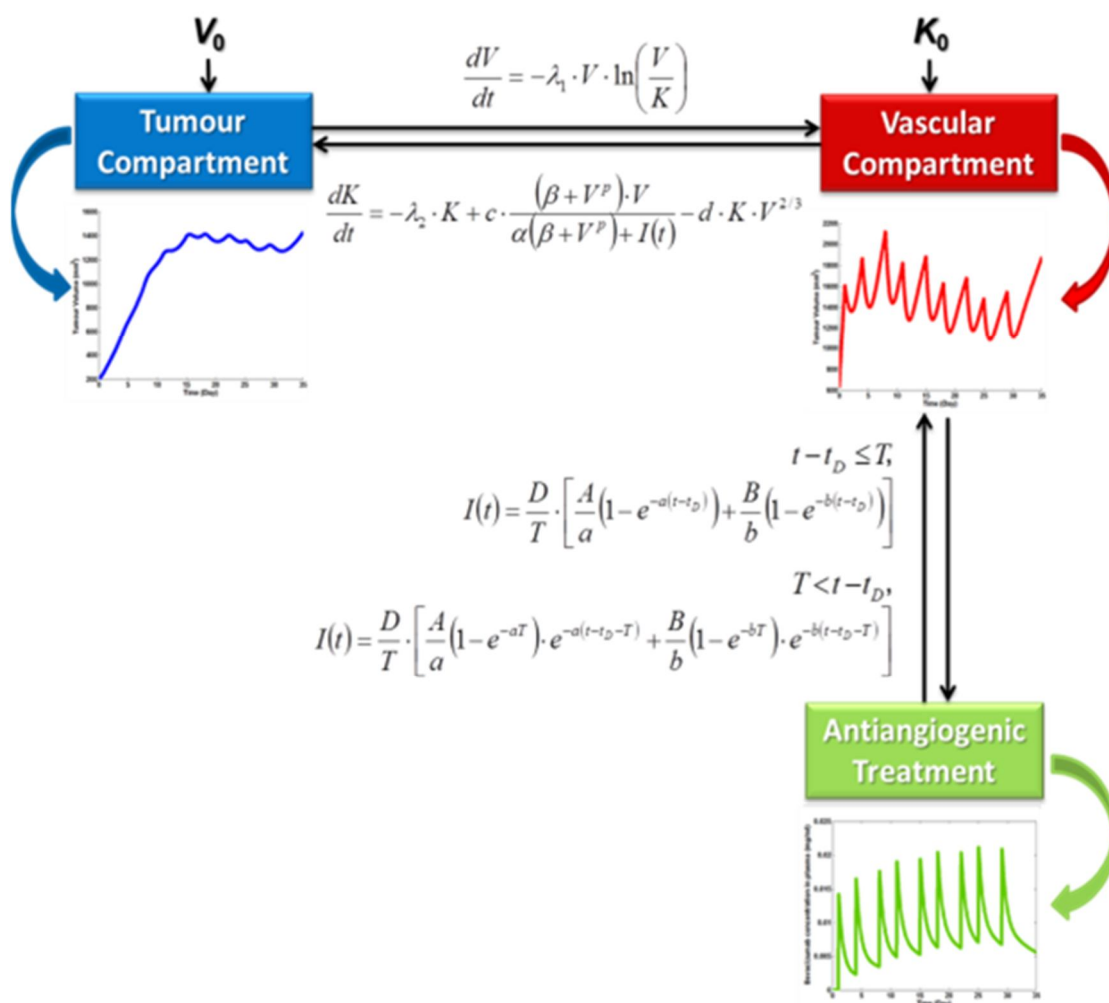


Fig. AA1: Information flow among the compartments of the vascular tumour growth under anti-angiogenic treatment hypomodel. V : time-dependent tumour volume, K : time-dependent carrying capacity (maximal tumour volume that can be supported by the given vasculature), V_0 : initial value for tumour volume, K_0 : initial value for carrying capacity, I : time-dependent bevacizumab concentration in host's plasma. Parameters involved in the model are explained in Table AA-1 and Table AA-2 (with use of Eqs.(AA5)-(AA8)).

The hypomodel has been implemented in MATLAB. Experiments concerning free tumour growth as well as tumour growth under intermittent bevacizumab treatment have been performed on a desktop computer with an AMD Phenom(tm) II X6 1055T Processor 2.80 GHz, 8.00GB RAM in Windows 7 with 64 – bit operating system and that the code execution time is of the order of a few seconds.

AA2. Basic Features of the Component Model

AA2.1 Vascular Tumour Growth under Anti-angiogenic Treatment

The dynamical system is governed by a pair of ordinary differential equations (ODEs) which reflect the interplay between tumour volume (V) and carrying capacity (K), i.e. the maximal tumour volume that can be supported by the given vasculature. The first ODE involved in the dynamical system under study describes the rate of change of the tumour volume V and assumes Gompertzian growth.

$$\frac{dV}{dt} = -\lambda_1 \cdot V \cdot \ln\left(\frac{V}{K}\right) \quad (\text{AA1})$$

The second ODE that is involved in the specific dynamical system monitors the temporal evolution of the carrying capacity of cancer cell population.

$$\frac{dK}{dt} = -\lambda_2 \cdot K + c \cdot \frac{(\beta + V^p) \cdot V}{\alpha(\beta + V^p) + I(t)} - d \cdot K \cdot V^{2/3} \quad (\text{AA2})$$

with non-negative coefficients. Parameters and variables involved in the equations of the vascular tumour growth model are explained in Table AA-1.

TABLE AA-1: DESCRIPTION OF THE VARIABLES AND PARAMETERS USED IN THE VASCULAR TUMOUR GROWTH MODEL.

	Mathematical Symbol	Units	Description
Independent variable	t	days	time
Dependent Variable	V	mm^3	tumour volume
Dependent Variable	K	mm^3	tumour carrying capacity
Parameter	λ_1	day^{-1}	Gompertzian growth constant
Parameter	λ_2	day^{-1}	proportionality constant related to the natural mortality of endothelial cells
Parameter	c	$\text{mg}/(\text{ml} \cdot \text{day} \cdot \text{mm}^{3p})$	proportionality constant related to the term reflecting endogenous stimulation of the tumour upon the vasculature
Parameter	d	$1/(\text{day} \cdot \text{mm}^2)$	proportionality constant related to the term reflecting endogenous inhibition of tumour vasculature
Parameter	α	$\text{mg}/(\text{mm}^{3p} \cdot \text{ml})$	constant related to the total amount of stimulators inside the tumour
Parameter	β	mm^{3p}	constant related to the total amount of stimulators inside the tumour
Parameter	p	≥ 0	Hill coefficient
Parameter	I	mg/kg	drug concentration in plasma

AA2.2 Bevacizumab Pharmacokinetic Model

This section outlines the computation of concentration $I(t)$ of the specific anti-angiogenic agent at a given time-point t in host's plasma. This function is involved in the right-hand side of Eq. (AA2) and more specifically, in the term reflecting the angiogenic stimulatory capacity of the tumour. A two – compartmental model assuming first-order elimination has been implemented in order to incorporate the pharmacokinetic properties of bevacizumab. Taking into account that the specific anti-angiogenic agent is administered via the intravenous route, the case of intravenous infusion has been addressed by applying zero-order absorption, reflecting steady drug delivery into patient's systemic circulation.

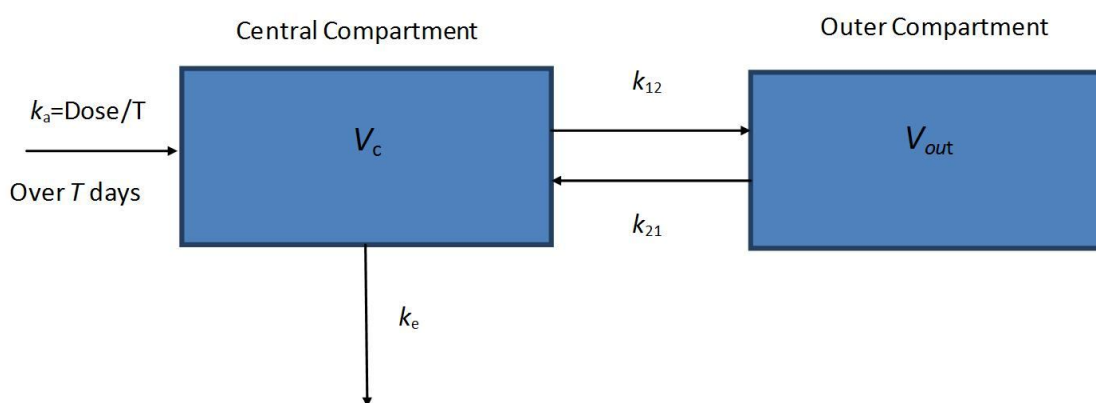


Fig. AA2: Schematic representation of a two – compartmental pharmacokinetic model. k_a absorption rate constant for the case of intravenous route of administration (i.v. infusion); V_c , volume of distribution of central compartment; V_{out} , volume of distribution of outer compartment; k_{12} , distribution rate constant from central compartment to outer compartment; k_{21} , distribution rate constant from outer compartment to central compartment; k_e , elimination rate constant;

The central compartment represents blood and all highly perfused tissues, i.e. vital organs that are in rapid equilibrium with blood such as lungs, kidney and liver. Drug elimination is assumed to occur from the central compartment according to the first order transfer rate k_e since kidney and liver are the two most important clearing organs. The outer compartment corresponds to poorly perfused tissues.

Given the fact that the drug concentration cannot usually be measured at the effector site, the concentration of drug in plasma is typically assumed to represent the concentration in the target tissue. Hence, the equation characterizing the central compartment is the one to be exploited by the vascular tumour growth model.

Thus, if T stands for the duration of infusion, D for the administered dose and t_D for the time-point of drug administration, the function that describes bevacizumab concentration $I(t)$ at a given time-point t in plasma, following a single drug infusion, is mathematically formulated as below:

While the infusion takes place, i.e. while $t - t_D \leq T$:

$$I(t) = \frac{D}{T} \cdot \left[\frac{A}{a} \left(1 - e^{-a(t-t_D)} \right) + \frac{B}{b} \left(1 - e^{-b(t-t_D)} \right) \right] \quad (\text{AA3})$$

During the post-infusion period, namely while $T < t - t_D$:

$$I(t) = \frac{D}{T} \cdot \left[\frac{A}{a} \left(1 - e^{-aT} \right) \cdot e^{-a(t-t_D-T)} + \frac{B}{b} \left(1 - e^{-bT} \right) \cdot e^{-b(t-t_D-T)} \right] \quad (\text{AA4})$$

where,

$$a = \frac{k_{21} \cdot k_e}{b} \quad (\text{AA5})$$

$$b = 0.5 \cdot \left(k_{12} + k_{21} + k_e - \sqrt{(k_{12} + k_{21} + k_e)^2 - 4k_{21} \cdot k_e} \right) \quad (\text{AA6})$$

$$A = \frac{1}{V_c} \frac{a - k_{21}}{a - b} \quad (\text{AA7})$$

$$B = \frac{1}{V_c} \frac{b - k_{21}}{b - a} \quad (\text{AA8})$$

More information on the model's assumptions and governing equations can be found in (Hacker et al. 2009). Parameters and variables involved in the pharmacokinetic model are explained in Table AA-2.

TABLE AA-2: DESCRIPTION OF THE VARIABLES AND PARAMETERS USED IN THE TWO-COMPARTMENTAL PHARMACOKINETIC BEVACIZUMAB MODEL.

	Mathematical Symbols	Units	Description
Independent variable	t	day	time-point
Dependent variable	I	mg/ml	bevacizumab concentration in plasma
Parameter	n	-	number of infusions to be administered
Parameter	D	mg	dose
Parameter	T	day	infusion duration
Parameter	V_c	ml	volume of central compartment
Parameter	k_{12}	day ⁻¹	transfer constant from central to peripheral compartment
Parameter	k_{21}	day ⁻¹	transfer constant from peripheral to central compartment
Parameter	k_e	day ⁻¹	rate of elimination
Parameter	d	mg/kg	dosage
Parameter	w	kg	host's weight
Parameter	t_D	day	administration time-point of anti-angiogenic treatment

AA2.3 Indicative Results

In order to study the qualitative behaviour of the hypo-model, numerous sets of code executions have been conducted testing the code with different parameter values, simulation time span, initial values and code module (free growth, constant treatment, intermittent treatment). Having adopted the classical graph representation, the following indicative results are presented so as to illustrate several points of interest concerning the dynamics of the model.

In the context of the current work, we have focused on the case of host – mouse due to the availability of reference values (Hahnfeldt et al. 1999; Poleszczuk et al. 2011) as well as the abundance of relevant experimental data extracted from published work (Higgins et al. 2007; Hoang et al. 2012; Selvakumaran et al. 2008).

AA2.4 Free Growth

The time course of the tumour volume and carrying capacity for the free growth of a tumour characterized by the parameter values used by Hahnfeldt et al. (1999) is demonstrated in Fig. AA3. Given that the volume of a spheroid is computed according to the formula $V = \frac{4}{3}\pi r^3$ and that the initial tumour volume is taken as equal to 200 mm^3 , the time-point 0 corresponds to a tumour radius equal to 3.63 mm and thus, to a vascularized tumour. The growth slowdown is obvious and the asymptotic limit obtained is approximately equal to 17346 mm^3 , a value consistent with the results in Hahnfeldt et al. (1999).

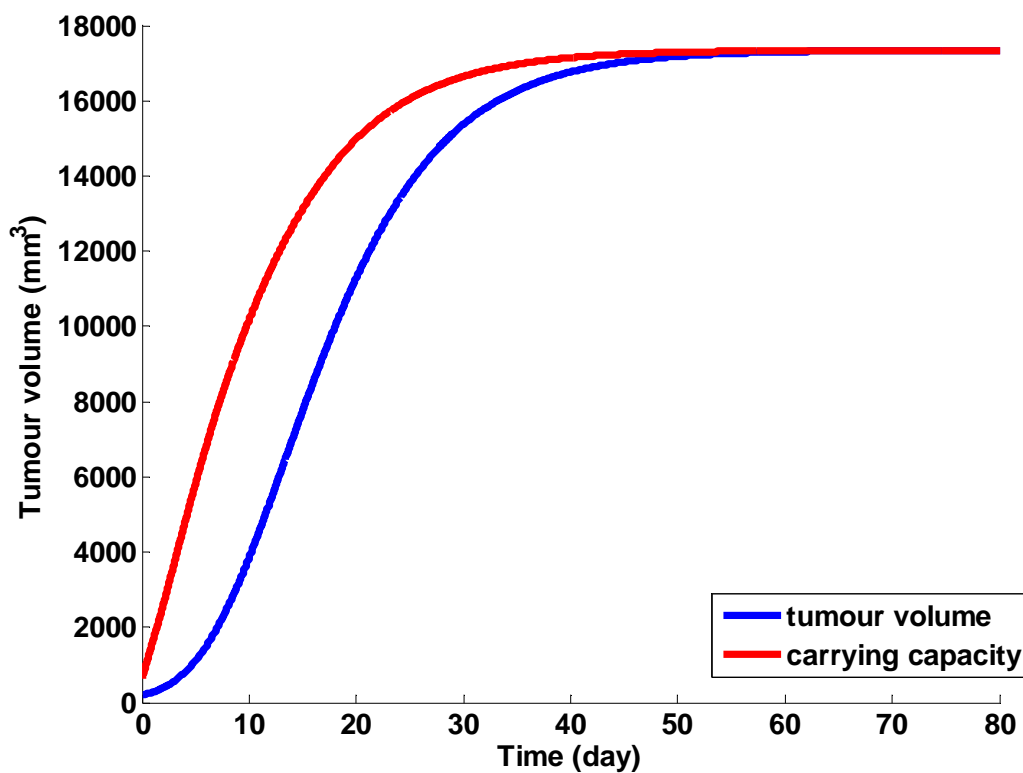


Fig. AA3: Simulation results for an untreated tumour characterized by the parameter values shown in Table AA-3.

AA2.5 Tumour Growth under Bevacizumab Monotherapy

In order to demonstrate the qualitative behaviour of the hypo-model in the context of the treatment module (Fig.AA4, Fig.AA5), we proceeded with simulating the effect of the application of a bevacizumab monotherapy treatment scheme to a mouse weighing 25 g, bearing a tumour characterized by the parameter values extracted from (Poleszczuk et al. 2011), except for parameter d where the value was adopted from (Hahnfeldt et al., 1999). The simulated scheme consists of the administration of 5 mg/kg of bevacizumab as a single-agent, twice weekly for a total of 9 doses. The specific treatment scheme details such as dosage, number and frequency of infusions, have been used in the context of various *in vivo* experiments in mice (Hoang et al. 2012; Salaun et al. 2010;

Higgins et al. 2007). The values of the parameters involved in the two – compartmental pharmacokinetic model have been extracted from (Wu et al. 2012) and are also only applicable for the case of host – mouse.

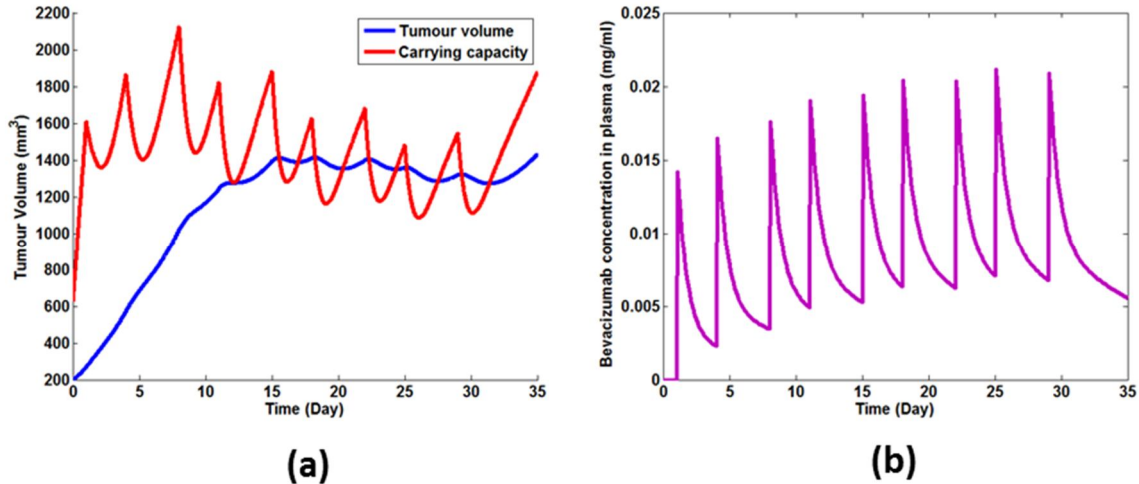


Fig. AA4: (a) Simulation results for a tumour treated with bevacizumab according to a scheme used in the context of various *in vivo* experiments in mice (Hoang et al. 2012; Salaun et al. 2010; Higgins et al. 2007) and characterized by the parameter values shown in Table AA-3. (b) The time course of bevacizumab concentration in plasma for the simulated treatment scheme, the details of which are shown in Table AA-3. Values of parameters involved in the pharmacokinetic model for the case of host-mouse were extracted from (Wu et al. 2012)

Treatment begins on the 1st day, when the tumour size has already grown to a volume equal to 269 mm^3 , i.e. when the radius of the tumour is approximately equal to 4 mm, assuming spheroid shape. Taking into account that time-point 0 corresponds to a tumour of 200 mm^3 , it can be observed that an initial overshoot of tumour volume (V) occurs, due to the fact that the tumour has been so far untreated. With the start of the regimen administration, a sharp decrease of tumour capacity is obvious and then the response of tumour volume follows, reflecting the fact that anti-angiogenic treatment targets directly the vascular compartment and following that, the tumour compartment responds. A closer inspection of Fig. AA4.a, reveals that each time the curve $K(t)$ intersects curve $V(t)$, the monotonicity of the function $V(t)$ alters. This is reasonable if the fact that tumour capacity is actually defined as the maximal tumour volume that the current vascular system can support, is taken under consideration. In Fig. AA4.b, the time evolution of bevacizumab concentration in plasma as computed via the two-compartmental pharmacokinetic model is shown.

TABLE AA-3: PARAMETER VALUES USED IN THE DEMONSTRATED CODE EXECUTIONS IN THE CONTEXT OF PRESENTATION OF INDICATIVE RESULTS

Parameters	Parameter values: Free growth	Parameter values: Intermittent bevacizumab monotherapy	Units	Reference
λ_1	0.192	0.192	day ⁻¹	(Hahnfeldt et al., 1999; Poleszczuk et al., 2011)
λ_2	0	0	day ⁻¹	(Hahnfeldt et al. 1999; Poleszczuk et al. 2011)
c	5.85	5.85	mg/(ml·day)	(Hahnfeldt et al. 1999; Poleszczuk et al. 2011)
d	0.00873	0.00873	1/(day · mm ²)	(Hahnfeldt et al. 1999)
α	n/a	1	mg /ml	(Poleszczuk et al. 2011)
β	n/a	1	-	(Poleszczuk et al. 2011)
p	0	0	-	(Poleszczuk et al. 2011)
Therapy – Related Parameters				
k_{12}	n/a	0.7536	day ⁻¹	(Wu et al. 2012)
k_{21}	n/a	0.3144	day ⁻¹	(Wu et al. 2012)
k_e	n/a	0.3888	day ⁻¹	(Wu et al. 2012)
V_c	n/a	7.975	ml	(Wu et al. 2012)
D	n/a	dosage*weight	mg	
T	n/a	1/48	day	-
dosage	n/a	5	mg/kg	(Hoang et al. 2012; Damiano et al. 2007; Higgins et al., 2007)
weight	n/a	0.025	kg	(Wu et al. 2012; Higgins et al. 2007)
number of infusions	n/a	9		(Hoang et al. 2012)
administration time-points	n/a	t ₁ =1 t ₂ =4 t ₃ =8 t ₄ =11 t ₅ =15 t ₆ =18 t ₇ =22 t ₈ =25 t ₉ =29	day	-

AA3. Reproducing a Series of *In Vivo* Experiments in Mice Treated with Bevacizumab

Eight *in vivo* experiments conducted in mice bearing breast (KPL-4), lung (H226), head and neck (SCC1) as well as colon (HCT116, HT29, HCP40 and HP40) tumour xenografts have been selected from relevant literature (Higgins et al. 2007; Hoang et al. 2012; Selvakumaran et al. 2008) in order to fit the specific modeling approach to actual experimental data. These experiments aimed at examining the anti-tumour activity of bevacizumab mono-therapy and combination treatment. Of course, in the latter case, only datasets corresponding to unperturbed tumour growth and bevacizumab monotherapy were exploitable by the hypo-model.

For the needs of the adaptation of the hypo-model to actual experimental data, two extra m-files have been implemented. Specifically, a cost function has been defined as the difference between the model's prediction and the actual value of the tumour volume, for the available instances of experimental data. The goal of the adaptation process is to minimize the objective function, in order to obtain the most accurate estimation of the variables under study. Hence, a script file has been implemented so as to specify the parameter values that minimize the squared value of the objective function of each data-point, with the use of Matlab function `lsqnonlin` in conjunction with the trust region reflective algorithm implemented in Matlab.

In order to quantify the experimental data obtained through relevant literature (Higgins et al. 2007; Hoang et al. 2012; Selvakumaran et al. 2008), the PlotDigitizer software has been used, which allows the extraction of the data (mean value \pm standard deviation) via its digitization. The fitting process for each experimental dataset (control group and treatment group) has been conducted in two steps: fitting the free growth module to the control group data and based on the result of the parameter estimation, fitting the bevacizumab monotherapy module to the treatment group data.

AA3.1 Description of a Subset of the Simulated Experiments and Respective Local Fitting Results

AA3.1.1 Experiment 1

In the context of a monotherapy antitumour efficacy study, twenty mice bearing KPL-4 human estrogen receptor-negative breast adenocarcinoma xenografts were divided into a vehicle and a treatment group dosed with bevacizumab at 5 mg/kg twice weekly intraperitoneally (Higgins et al. 2007). The results of the local fitting are presented in Table AA-4 and Fig. AA5.

AA3.1.2 Experiment 2

In the context of a combination treatment antitumour efficacy study, twenty mice bearing KPL-4 human estrogen receptor-negative breast adenocarcinoma xenografts were divided into a vehicle and a treatment group dosed with bevacizumab at 5 mg/kg twice weekly intraperitoneally (Higgins et al. 2007). The results of the local fitting are presented in Table AA-4 and Fig. AA5.

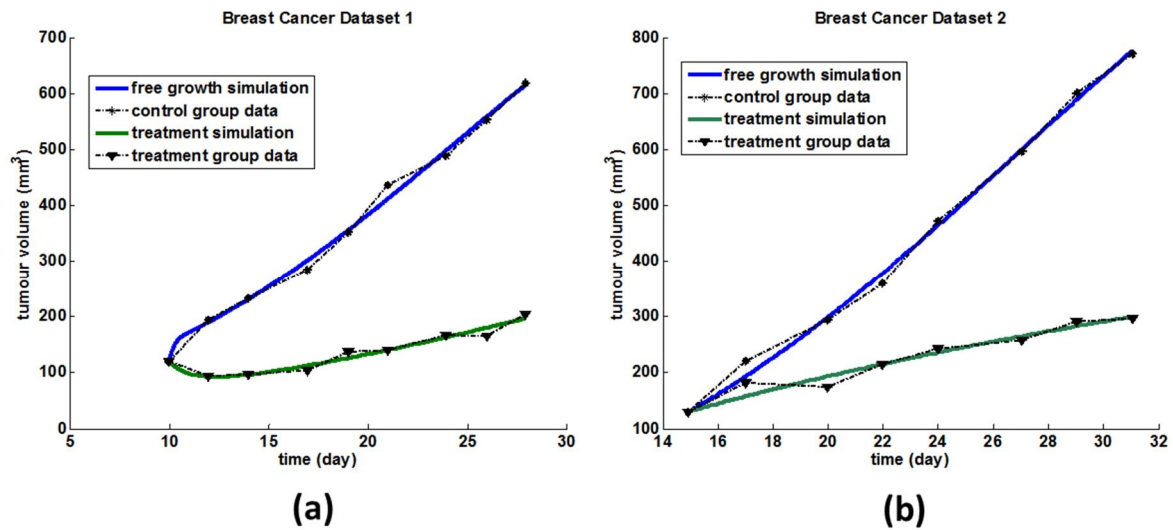


Fig. AA5: Graphical representation of the fitting results of the vascular tumour growth and response to bevacizumab treatment model to experimental data concerning KPL-4 human estrogen receptor-negative breast adenocarcinoma xenografts that were extracted from (Higgins et al. 2008): **(a)** In the context of a bevacizumab monotherapy study, **(b)** In the context of a bevacizumab combination treatment study

TABLE AA-4: PARAMETER VALUES THAT HAVE BEEN SPECIFIED BY LOCALLY FITTING THE VASCULAR TUMOUR GROWTH AND RESPONSE TREATMENT MODEL TO EXPERIMENTAL DATA EXTRACTED FROM (HIGGINS ET AL. 2007)

STUDY	EXPERIMENTAL GROUP	λ_1	c	d	β	p	K_0	RMSE	FOO
DATASET 1	CONTROL	4.883	0.149	0.001	-	-	159.48	10.833	$9.66 \cdot 10^{-3}$
		5	8	4			83	7	
	TREATMENT (5 mg/kg)	0.682	0.095	0.001	1	4.9993	76.463	7	$9.46 \cdot 10^{-4}$
DATASET 2	CONTROL	0.133	0.524	0.008	-	-	650	13.308	$6.79 \cdot 10^{-5}$
		8	1	8				6	
	TREATMENT (5 mg/kg)	0.104	0.524	0.008	1	3.8923	358.20	11.770	$2.68 \cdot 10^{-3}$
		8	1	8			54	3	

AA3.1.3 Experiment 3

Four groups of athymic mice bearing H226 xenografts (lung cancer cells) were treated with IgG (control) or 3 dose levels of bevacizumab (1, 5 and 25 mg/kg intraperitoneally) twice weekly for a total of 9 doses (3 mice per group) (Hoang et al. 2012). The results of the local fitting are presented in Table AA-5 and Fig. AA6.

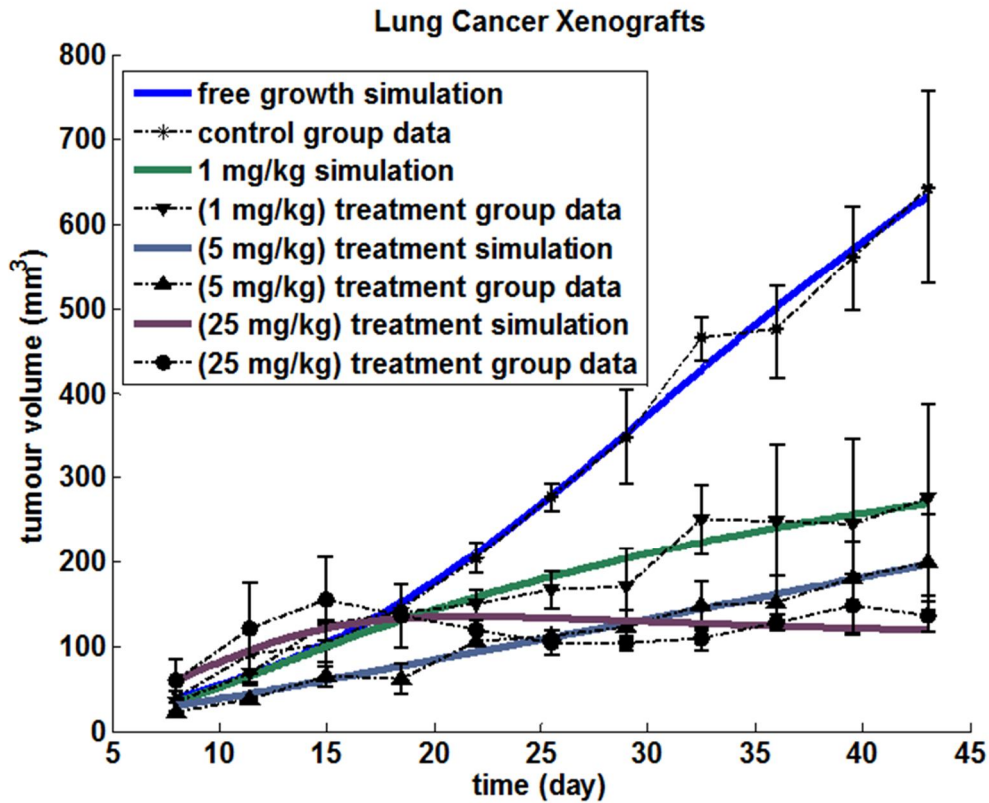


Fig. AA6: Graphical representation of the fitting results of the vascular tumour growth and response to bevacizumab treatment model to experimental data concerning lung tumour xenografts (Selvakumaran et al. 2008)

TABLE AA-5: PARAMETER VALUES THAT HAVE BEEN SPECIFIED BY LOCALLY FITTING THE VASCULAR TUMOUR GROWTH MODEL TO EXPERIMENTAL DATA EXTRACTED FROM (HOANG ET AL. 2012)

CELL LINE	EXPERIMENTAL GROUP	λ_1	c	d	β	p	K_0	RMSE	FOO
H226 (lung cancer cells)	CONTROL	0.1022	3.2431	0.0075	-	-	208.6161	16.7275	$2.38 \cdot 10^{-3}$
	TREATMENT 1 (1 mg/kg)	0.1022	0.3605	0.0075	1	6.9942	320.2175	17.1804	$3.50 \cdot 10^{-4}$

TREATMENT 2 (5 mg/kg)	0.0495	0.4377	0.0075	1	10	350	7.8339	$3.63 \cdot 10^{-6}$
TREATMENT 3 (25 mg/kg)	0.1022	0.1721	0.0075	1	10	334.0558	21.1411	$7.10 \cdot 10^{-5}$

The results produced by the hypo-model have been thoroughly studied and reveal significant qualitative similarities with relevant experimental observations. An initial exploratory parametric analysis has been conducted, in order to gain insight into the behaviour of the model for an untreated vascularized tumour. The reproduction of the results of a series of in vivo experiments in mice treated with bevacizumab and the good agreement of simulation results with experimental data lend support to the underlying model.

A future extension of the model will be its coupling with a discrete entity – discrete event model of tumour growth (Stamatakis 2011).

AA4. References

Argyri K, Dionysiou D, Stamatakis G Modeling the interplay between pathological angiogenesis and solid tumour growth: The anti-angiogenic treatment effect. Advanced Research Workshop on In Silico Oncology and Cancer Investigation - The TUMOUR Project Workshop (IARWISOCI), 2012 5th International , vol., no., pp.1,4, 22-23 Oct. 2012

Damiano V, Caputo R, Garofalo S, Bianco R, Rosa R, Merola G, Gelardi T, Racioppi L, Fontanini G, De Placido S, Kandimalla ER, Agrawal S, Ciardiello F, Tortora G (2007) TLR9 agonist acts by different mechanisms synergizing with bevacizumab in sensitive and cetuximab-resistant colon cancer xenografts. Proc Natl Acad Sci USA 104(30):12468–12473

Hacker, Miles P., William S. Messer, and Kenneth A. Bachmann. 2009. *Pharmacology principles and practice*. London: Academic Press.

Hahnfeldt P, Panigrahy D, Folkman, Hlatky L (1999) Tumour development under angiogenic signaling: A dynamical theory of tumour growth, treatment response and postvascular dormancy. Cancer Res 59: 4770-4775.

Higgins B, Kolinsky K, Linn M, et al. (2007) Antitumour activity of capecitabine and bevacizumab combination in a human estrogen receptor-negative breast adenocarcinoma xenograft model. Anticancer Res 27:2279–87
Hoang T, Huang S, Armstrong E, Eickhoff JC, Harari PM (2012) Enhancement of radiation response with bevacizumab. J Exp Clin Cancer Res, 31 (37)

Poleszczuk J, Bodnar M, Forys U (2011) New approach to modelling of antiangiogenic treatment on the basis of Hahnfeldt et al. model. Math Biosci Eng 8(2):591-603. doi: 10.3934/mbe.2011.8.591

Salaun PY, Bodet-Milin C, Frampas E, Oudoux A, Sai-Maurel C, Faivre-Chauvet A, Barbet J, Paris F, Kraeber-Bodere F (2010) Toxicity and efficacy of combined radioimmunotherapy and bevacizumab in a mouse model of medullary thyroid carcinoma Cancer. 116(4 Suppl):1053–1058.

Selvakumaran M, Yao KS, Feldman MD et al. (2008) Antitumour effect of the angiogenesis inhibitor bevacizumab is dependent on susceptibility of tumours to hypoxia-induced apoptosis. Biochem Pharmacol, 75: 627–638

G.Stamatakis "In Silico Oncology Part I: Clinically Oriented Cancer Multilevel Modeling Based on Discrete Event Simulation" In T.Deisboeck and G. Stamatakis Eds 407-436 2011-01-01 CRC Press, Print ISBN: 978-1-4398-1440-6 eBook ISBN: 978-1-4398-1442-0 DOI: 10.1201/b10407-19 Boca Raton, Florida, USA, 2011

Wu F, Tamhane M, Morris M (2012) Pharmacokinetics, Lymph Node Uptake, and Mechanistic PK Model of Near-Infrared Dye-Labeled Bevacizumab After IV and SC Administration in Mice. The AAPS Journal 14: 252-261

AA5. Description of the Alternative Vascular / Angiogenesis Component Model (AA) through the 13 Perspectives

TABLE "AA-13P" (FIRST PART)		
PERSPECTIVE CODE NUMBER	PERSPECTIVE TITLE	EXAMPLES OF POSSIBLE CATEGORIES PER PERSPECTIVE
I	TUMOUR-AFFECTED NORMAL TISSUE MODELLING	tumour normal tissue
II	SPATIAL SCALE(S) OF THE MANIFESTATION OF LIFE	cellular tissue organ body system
III	TEMPORAL SCALE(S) OF THE MANIFESTATION OF LIFE	h d
IV	BIOMECHANISM(S) ADDRESSED	angiogenesis oxygenation metabolism
V	TUMOUR TYPE(S) ADDRESSED	lung cancer other solid tumours
VI	TREATMENT MODALITY(-IES) ADDRESSED	no treatment consideration targeted therapy

TABLE "AA-13P" (SECOND PART)		
PERSPECTIVE CODE NUMBER	PERSPECTIVE TITLE	EXAMPLES OF POSSIBLE CATEGORIES PER PERSPECTIVE
VII	GENERIC CANCER BIOLOGY – CLINICALLY DRIVEN CHARACTER OF THE MODELLING APPROACH	generic cancer biology clinically driven
VIII	ORDER OF ADDRESSING DIFFERENT SPATIAL SCALES	bottom-up top-down
IX	ORDER OF ADDRESSING DIFFERENT TEMPORAL SCALES	short periods → longer periods
X	MECHANISTIC-STATISTICAL CHARACTER OF THE MODELLING APPROACH	mechanistic
XI	DETERMINISTIC-STOCHASTIC CHARACTER OF THE MODELLING APPROACH	deterministic
XII	CONTINUOUS-FINITE-DISCRETE CHARACTER OF THE MATHEMATICS INVOLVED	continuous finite (finitized continuous)
XIII	CLOSED FORM SOLUTION – ALGORITHMIC SIMULATION MODELLING APPROACH	algorithmic simulation

B. The Tumour Growth Biomechanics Component Model

B1. Introduction

Biomechanics is an important aspect of tumour growth especially when the shape of the growing or shrinking tumour is of interest [B1-B48]. The tumour growth biomechanics model being developed by UBERN focuses on the development of a hypomodel describing the biomechanical aspects of tumour growth, and on its integration with a micro-scale cellular-level simulator.

This chapter presents a first tested version of the biomechanical model and details its interaction with the cellular-level growth model developed by ICCS. A simulator, coupling both models, has been constructed based on imaging, biological, histopathological, in-vitro and in-vivo data of individual patients: The cellular-level solver provides the biomechanical simulator with tumour cell numbers and concentration map, while the macro-scale biomechanical solver feeds back preferred directions for cell proliferation. An open-source FEM solver, modified for the purposes of this project, is used to simulate the mechanical effects of tumour growth and the diffusion-based invasion of tumour cells into surrounding tissue.

We studied the growth of a realistic asymmetric small tumour inside the lung and demonstrated the stress distribution and displacements of the healthy tissue as a result of tumour growth.

B2. Scientific Background

B2.1 Lung Cancer

Lung cancers are, statistically, the leading type of cancer for both genders according to the United States National Cancer Institute (NCI), although prostate and breast cancers are the most prevalent ones among men and women, respectively [B1, B2].

Survival rates (1 and 5-year) for lung cancer, however, differ considerable from survival rates of prostate and breast cancers: While survival rates for latters are near 100 % if diagnosed at early stages, lung cancer cases diagnosed during 2003 to 2009 reached survival rates of only 43% (1 year) and 17% (5 year). Only 15 % of lung cancers are diagnosed at a localized stage, for which 5-year survival at 54 % is reported [B1].

Lung cancer is categorized into two different classes of (a) non-small-cell and (b) small-cell types. Current best treatment practice for lung cancer include surgery, radiation therapy, chemotherapy and targeted therapies, or a combination of these. The choice of treatment method depends on the type of cancer, its stage and the biological characteristics of cancer cells [B1]. Their efficiency is affected by targeting of the cancerous tumours, and limited by undesired treatment side-effects in the healthy lung tissue.

Numerical simulations provide a proven approach towards enhancing accuracy and efficacy of therapeutic methods .

B2.2 Lung Biomechanical Models

The parenchymal tissue of the lung is a complex network of collagen and elastin fibres connecting the vasculature, airways and the pulmonary interstitium. Thus, precise estimation of material properties of this composite organ and determining its unique mechanical behaviour are still active fields of research [B6, B7]. In addition, pathologic progression of parenchymal diseases tremendously affect the macroscopic material properties of lung tissue [B7-B10].

Different methods have been applied to determine material properties and mechanical behaviour of the lung. For instance, ex-vivo measurements have been performed by applying predetermined forces to tissue strips, performing pressure-volume perturbation experiments, or inflating a post mortem lung [B9, B11-B13]. Imaging modalities have also been used extensively to study the mechanics of the lung in-vivo. Four-dimensional computed tomography (4-D CT) is used to monitor the deformation of the lung, and by comparing its results to finite element analysis, the patient-specific mechanical properties have been optimized to replicate realistic lung movement. Furthermore, magnetic resonance imaging (MRI) can be used to study the regional motion of the lung [B2, B14-B16]. MRI grid tagging, despite its limiting low resolution, has been employed for tracking the three-dimensional lung deformation and directly measuring a displacement map of the lung [17, 18]. Registration of lung images and calculation of its movement are of great importance in radiation therapy, as this can be used to minimize the dose given to healthy lung tissue by adapting dose delivery to the motion of the tumour throughout the breathing cycle [B5, B19, B20].

Various material models have been used extensively to simulate the mechanical behaviour of the lungs by Finite Element Methods (FEM). These investigations employed a variety of material properties for the lung tissues [B21], including hyper-elastic material properties [B4]. FEM has been proven to be an effective tool to aid image-guided radiotherapy with increasing interest in its usage, see [B3, B22] for recent examples.

B2.3 Biomechanical Models of Tumour Growth

Other than radiation-therapy guidance, FEM is used to predict the mechanical forces on the outer boundary of the lung, as well as on the border between lung and tumour. Precise calculation of these forces and the stress distribution in the vicinity of tumour boundaries could significantly enhance therapeutic scenarios and interventional methods. As the patterns of respiratory and tumour-related displacements are uniquely associated with individuals, patient specific FEM analysis is expected to lead to more realistic patterns and highly effective treatments [B23].

The effect of a pressure force on the outer boundary of the tumour has already been modelled to simulate tumour growth inside the brain and lung [B24]. Despite effectively matching the final shape of the tumour to its actual boundaries in the organ, these models do not take into account cancerous-cell diffusion and resulting biomechanical effects. Most investigations in literature considered either pure diffusion/reaction of tumour cells and its biomechanical effect [B25-B27], or the outward growth of the tumour and its mechanical interaction with the organ (so called mass effect) [B24, B28-B30]. Recently, there have been attempts to combine diffusion/reaction model and mechanical growth to enhance the physiological accuracy of FEM simulations [B31, B32]. These models predict the deformation of surrounding tissue as a result of tumour growth, cancerous cell diffusion and therapeutic regimens over relevant time scales.

The accuracy of FEM simulations depends on two main factors: appropriate modelling of the physiological features of the organ, and the accuracy to which material properties and mechanics are approximated. As these factors are highly patient-dependent, well-planned experimental campaigns are necessary [B33, B34].

The model presented here addresses the combined effect of cell diffusion and mechanical growth, taking into account cell proliferation and cellular response to therapeutic interventions. Mechanical stresses resulting from tumour-tissue interaction are expected to result in asymmetric growth of the tumour.

B3. Coupled Model for Realistic Tumour Growth

The multi-scale hyper modelling scenario which is being developed in this project combines sub-cellular processes related to cell proliferation and cellular response to therapeutic agents, as well as macroscopic processes such as diffusion of tumour cells into the surrounding tissue and biomechanical interaction between healthy tissue and tumour. As these processes occur on different spatial and time scales, they are represented by distinct models, Fig. B1:

1. Micro-scale cellular model for simulating cell proliferation and response to therapeutic agents.
2. Macro-scale biomechanics model for simulating diffusion processes and tumour mass effect.

Tissue boundaries and material properties for the initialization of the Biomechanics Simulator are provided through Finite Element Models which can be generated automatically from segmented volumetric images. Initial tumour volume and geometry for the Cell Simulator may likewise be inferred from volumetric images, or be initialised as simple geometric shapes.

The microscopic cell-level model [B47,B48] provides the macroscopic biomechanical model with changes in cell population, whereas the macroscopic model simulates the mechanical stresses caused by the tumour growing within the organ. Iterative evaluation of both models allows tumour growth and shrinkage to be modelled. Both models and their joint application have been tested successfully for brain tumour simulation [B43].

The following Section B4 provides a detailed description of the biomechanical and diffusion model, as well as of the interaction between Biomechanics Simulator and Cell Simulator.

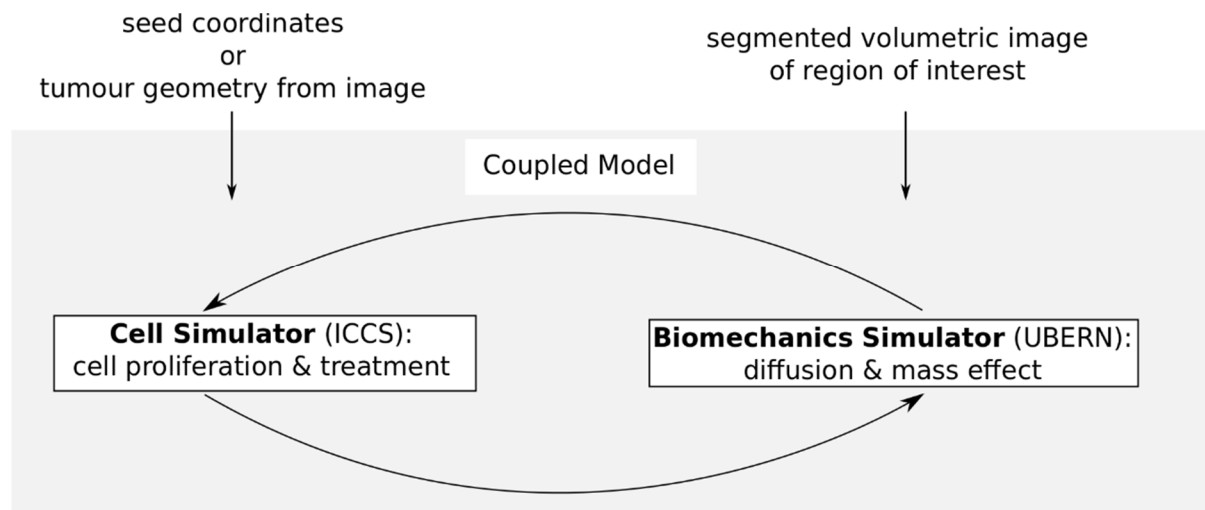


Fig.B1 Coupled model for realistic simulation of tumour growth.

B4. Biomechanical and Diffusion Modelling

In this section, we introduce the combined biomechanical and reaction/diffusion model and the finite element solver employed by the simulation module. Its interaction and data exchanged with the cell growth simulator are described.

B4.1 Model

The developed model aims at supporting realistic simulation of tumour growth and shrinkage by modelling the effects of cell diffusion from the bulk tumour into surrounding healthy tissue, and of mechanical constraints on growth direction, respectively.

After a computational model of the patient-specific anatomy has been generated, two effects of tumour-tissue interaction are simulated using the finite element method; the cellular infiltration in the neighbouring tissues and mass effect.

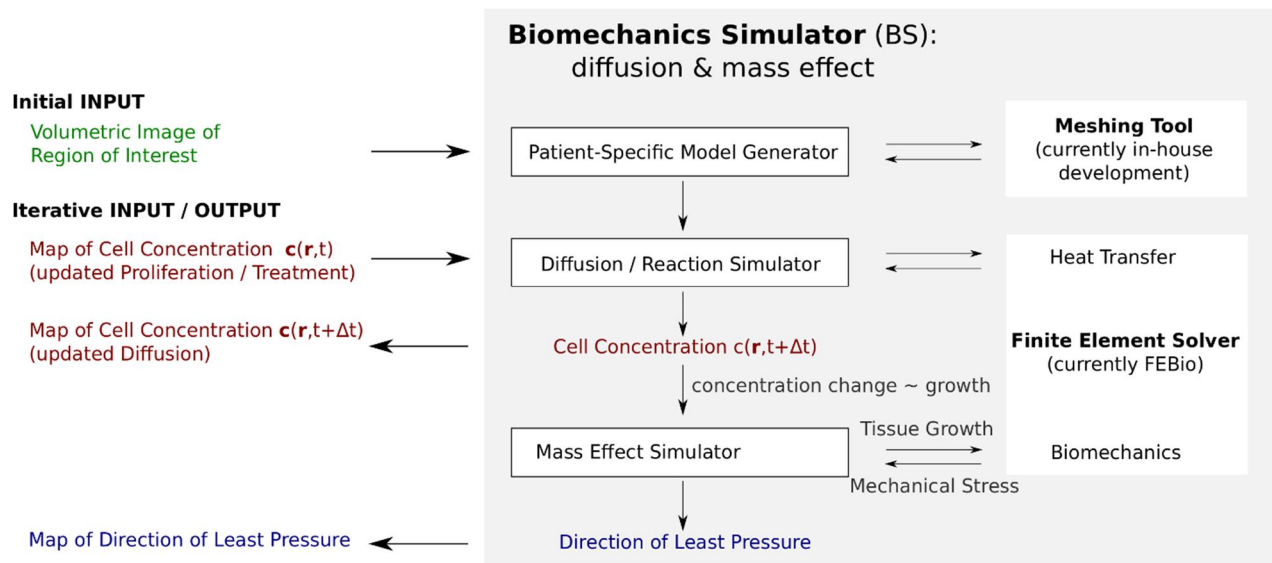


Fig.B2 Processes, inputs & outputs of biomechanics simulator

A given initial distribution of tumour cell concentrations $\mathbf{c}(\mathbf{r}, t)$, changes over a specified time interval Δt into an updated concentration $\mathbf{c}'(\mathbf{r}, t + \Delta t)$ according to the reaction/diffusion equation [B32]:

$$\frac{\partial c}{\partial t} = \text{div}(D_t \nabla c) + S(c, t) - T(c, t) \quad (\text{B1})$$

Where D_t is the diffusion tensor indicating the preferential direction of diffusion in the tissue, and $S(c, t)$ and $T(c, t)$ are the source and sink terms. These are obtained from the biological model of the Cell Simulator and reflect tumour cell proliferation and therapy-related cell death, respectively.

Cell concentrations above (below) an initial reference concentration value c_{init} are linked to volumetric increase (decrease) of the respective geometrical cell. A growth factor for this tissue segment (tumour) is defined according to following relation:

$$Growth = \sqrt[3]{\left(\frac{c}{c_{init}}\right)} - 1 \quad (B2)$$

Based on this information, the distribution of mechanical stress is computed in the region of interest, following general mechanics principles as reviewed in the Appendix B7.1. Assuming that cells will follow the direction of least pressure in order to balance this mechanical stress, the directionality of tumour growth/shrinkage can be inferred from the mechanical stress distribution.

Simulating tumour growth/shrinkage over an extended period of time, thus requires iteration between this biomechanical model and a biological model that simulates cell proliferation, spatial redistribution and response to therapeutic agents.

Internally, the Biomechanics Simulator employs validated open source tools for the creation of a finite element model of the region of interest and for solving diffusion and mechanical equations on this computational grid. In order to decouple the Biomechanics Simulator from the evolution of these tools, cross compilation is avoided and only binary executables are invoked instead. Data exchange between the Biomechanics Simulator and these tools takes place through temporary files which will be further detailed in Section B4.4

The following Section B4.2 introduces the finite element solver that is being used in the current implementation of the Biomechanics Simulator.

B4.2 Open-Source Finite Element Solver: FEBio

Originally developed at the University of Utah and now supported by the University of Utah and the Musculoskeletal Biomechanics Laboratory at Columbia University, FEBio is an open-source software for solving nonlinear large deformation problems in solid biomechanics and biophysics using the finite element methods [B39]. It provides appropriate constitutive models, efficient numerical solvers and diverse initial and boundary conditions.

In order to model the growth of tumour regions, we have created a new *growing* material as run-time plugin in FEBio, which calculates stress distribution and element displacement. This material is initiated with the Young's modulus and Poisson ratio of the tumour, as well as a growth factor that is computed from the volume change during the previous time-step according to Equation (B2).

As indicated in Fig. B2, the diffusion of the tumour cells can also be modelled in FEBio, using its heat transfer feature: Diffusion of cells is considered in analogy to the diffusion of heat, and the final concentration could be determined by computing the temperature. Since FEBio's functionalities for coupling mechanical and thermal models are limited, both simulation steps will be computed sequentially.

FEBio executables and source code are freely available for non-commercial use, including academic research and teaching applications.

Its non-commercial license is available at http://mrldata.sci.utah.edu/data/FEBio_EULA.pdf.

B4.3 Execution Workflow and Coupling between Simulators

In this section we explain how a patient-specific biomechanical-biological model is generated, and how the macroscopic Biomechanics Simulator is coupled to the microscopic cellular solver.

B4.3.1 Generation of Computational Grid

An automatic smooth mesh generator, developed in our group, is used to generate a finite element model from a volumetric image of the region of interest. The image-based voxel-mesh algorithm used to generate the computational domain provides a fully automated and robust method. However, in order to avoid the occurrence of jagged edges on boundaries, which is associated with this method [B36, B37], a smoothing step was added to the procedure.

In this approach, distorted elements are split into prisms, which significantly improves the quality of the near-boundary mesh at comparably low computational cost. Although the resulting mesh resembles hexahedral elements, as a result of smoothing near the boundaries, voxel-based meshes can reach an accuracy equivalent to more complex tetrahedron models. To smooth the mesh, the outer surface of the mesh is extracted and smoothed according to the geometric signal processing approach of Taubin [B38]. The algorithm is based on a Fourier-like decomposition of the geometry, calculated from the Laplacian operator. The degree of smoothing (defined here as smoothing frequency, k) is mainly limited by the fact that inverted elements might appear with extensive smoothing.

B4.3.2 Execution of Coupled Simulator

The derived computational mesh is used to generate an initial input file for the Finite Element Solver. Currently, FEBio is used, requiring a FEBio compatible xml format as input. This input file will be frequently updated during the simulations on pre-defined time steps to recompute diffusion and stress field based on updated concentration maps.

The process work flow, shown in Fig. B2 starts with the diffusion/reaction step. In this step the tumourous cells obtained from the Cell Simulator (updated by the rate of their generation and elimination due to therapy) invade healthy tissue. To simulate this process, the concentration distribution is calculated based on the diffusion coefficient of tumour cells within the organ. The concentration map is then exported to the mass effect simulator, where the growth of the tumour is modelled and its biomechanical interaction with healthy lung tissue is simulated. Cell concentrations (updated by diffusion) are also mapped back to the cellular-level mesh to compute the biological processes in the next time interval based on updated concentration values. The displacement values and stress tensor are stored to determine the preferred direction of cell growth which is also passed to the cell simulator.

B4.3.3 Coupling between Cell and Biomechanics Simulator

After completion of a biological simulation time step, updated values of cell concentrations for the next biomechanical iteration step are provided by the Cell Simulator [B44].

Currently, data exchange between Cell & Biomechanical Simulator is facilitated by an integration class, Fig. B3: The cellular-level model requires the direction, along which cell proliferation and thus tumour growth will take place. The biomechanical simulator provides this information by computing the direction against which the cells sense a minimum pressure [B45, B46]. In return, the biomechanical solver needs information on cell concentrations inside each geometric cell to calculate the stress distribution resulting from tumour growth. The biological microscopic model provides this concentration information to the biomechanical solver [B45].

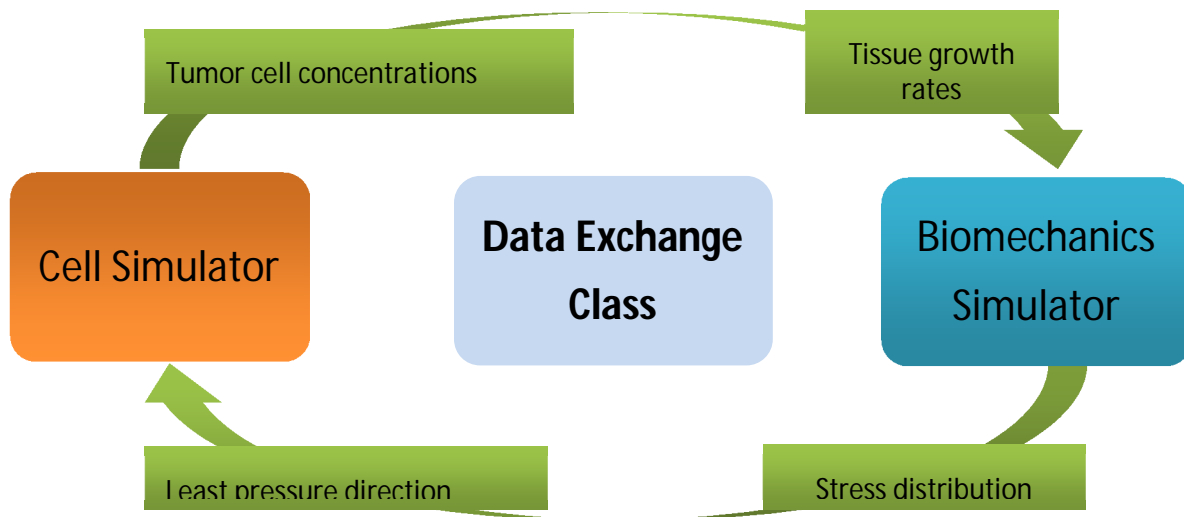


Fig.B3 Current Implementation of Biomechanics Simulator

As both models operate on different computational meshes, information for solving the concerned equations must be transferred between those representations. In particular, accurate modelling of diffusion effects requires an efficient data exchange and interpolation method between both Simulators.

A looser coupling between both simulation engines is envisaged, and the required data exchange capabilities are detailed in the following Section B4.4.

B4.4 Model Inputs & Outputs

The following Table B-1 lists input and output of the Biomechanics Simulator (BS) and its data exchange with the Cell Simulator (CS).

TABLE B-1. BIOMECHANICS SIMULATOR: INPUTS & OUTPUTS

	Description	Format	Producer	Consumer
INPUT	Volumetric segmented image of region of interest	Currently any ITK supported image format	imaging	BS (meshing tool)
	Simulation Parameters	xml	researcher / configuration wizard	BS
	Map of tumour cell concentrations (updated after cell proliferation & treatment)	To be defined with ICCS	CS	BS
OUTPUT	Map of tumour cell concentrations (updated after diffusion)	To be defined with ICCS	BS	CS
	Map of directions of least pressure	To be defined with ICCS	BS	CS

As both simulation engines operate on distinct computational meshes, mapping tools will be needed that transform the output of the Biomechanical Simulator into a representation that is suitable for further processing by the Cell Simulator, and vice versa. This mapping includes

- Coordinate transformation between BS and CS coordinate systems.
- Bidirectional interpolation properties (i.e. cell number/concentration) of geometric cells (CS) to nodes in the computational grid (BS).

In addition to the model input listed in Table B-1, parameters for this mapping will need to be supplied to the computational service that invokes the coupled biological/biomechanical simulator.

Internally, the Biomechanics Simulator employs validated open source tools as described in Section B4.1 Data exchange between the Biomechanics Simulator and these tools takes place through the temporary files listed in Table B-2. The Biomechanics Simulator will therefore require read and write access on a temporary scratch space that may be deleted after termination of the coupled simulator.

TABLE B-2 DATA EXCHANGE FILES BETWEEN BIOMECHANICS SIMULATOR AND COMPUTATION TOOLS USED INTERNALLY.

	Description	Format	Producer	Consumer
INTERNAL	FEM of region of interest (initial geometry and material properties)	Currently FEBio compatible mesh specification [XML according to .feb schema]	BS (meshing tool)	BS (FEM solver)

	FEM of region of interest (updated material properties)	Currently FEBio compatible mesh specification [XML according to .feb schema]	BS	BS (FEM solver)
	Stress map	CSV	BS (FEM solver)	BS
	Displacement map	CSV	BS (FEM solver)	BS

B5. Application to Lung Cancer

We applied the approach introduced in Sections B3 and B4 to the modelling of lung cancer.

B5.1 Creation of Patient-Specific Lung Model

The Lung Image Database Consortium image collection (LIDC-IDRI) was used to construct the lung model with 512x512x133 voxels size [B35], which was then segmented with the NIH-C1DI lung segmentation tool. The tumour was excluded from the lung model so that a patient-specific tumour model could be used for the simulation. This patient-specific model was obtained from patient datasets (CT scan) and allowed initialisation of the Cell Simulator with a 'realistic' tumour shape, instead of an 'artificial' spherical tumour randomly placed in the tissue.

The segmented mask includes the lung tissue as well as trabecula, while the latter is excluded in the process of mesh generation.

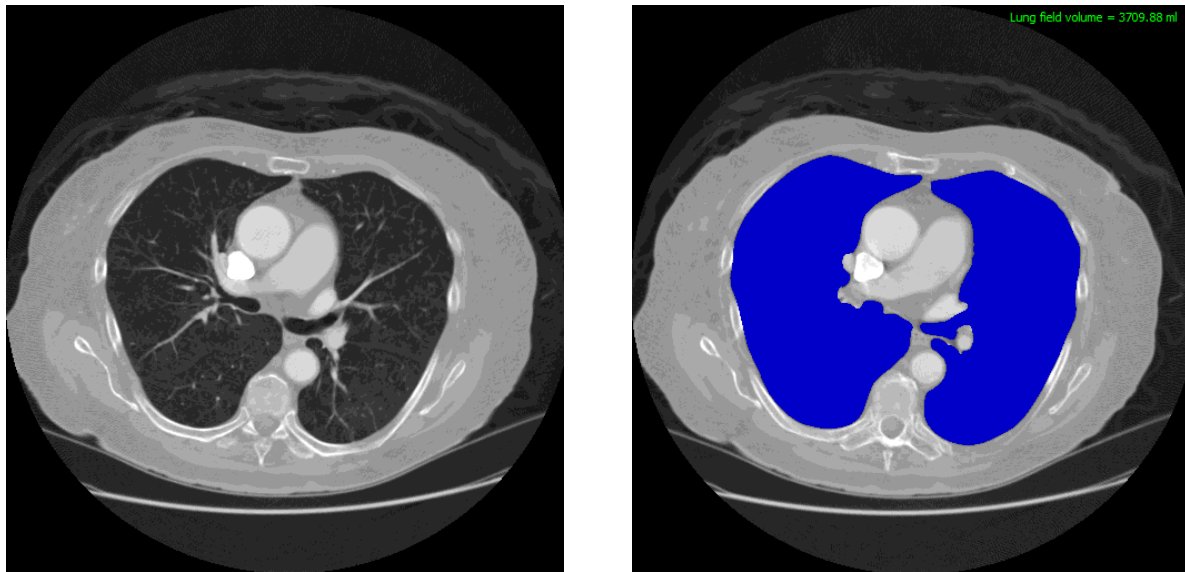


Fig. B4: (Left) The lung atlas used for the generation of the model. (Right) Segmented atlas using the NIH-CIDR lung segmentation tool.

The segmented mask of the image was exported as 'hdr' file to the open-source software 'ITK-Snap' and converted into the 'mha' format for further processing. The segmented stack of the lung was then resampled with a factor of 4 to limit computational cost, and was processed by the mesh generation tool described in Section B3 using a smoothing factor $k = 0.03$ which was found as optimal trade-off between mesh quality and model accuracy.

The resulting model consisted of 264128 nodes and 253356 elements, of which 198469 elements are hexahedral and the rest wedge elements. 1380 elements were removed from the original mesh because of their negative Jacobians. However, since most of them were located close to the outer boundary and distanced from the tumour, this will not influence the final results of the simulation. The creation of the mesh took roughly 4 minutes on a Pentium 4/2.4GHz CPU with 2GB of RAM and was fully automatic.

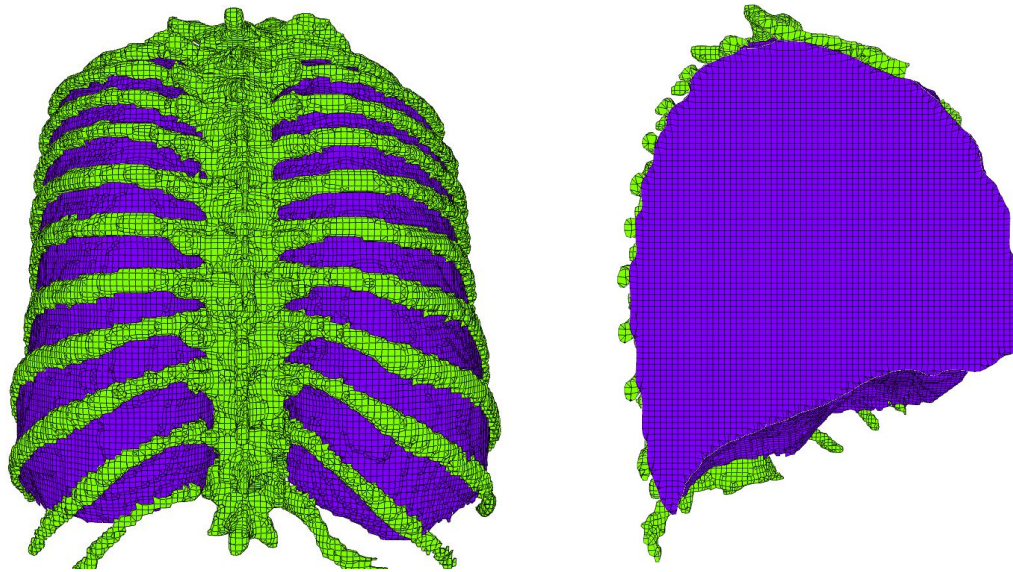


Fig.B5 Finite element model of the brain used for the simulation of the tumour growth. The different colours represent the different anatomical structures used for the simulation

B5.2 Model Parameters and Boundary Conditions

Parameters for diffusion model, Equation (B1), and mechanics model, Appendix B7.1 , were identified from literature and are presented in this section.

B5.2.1 Diffusion

The average diffusivity properties of the lung tissues were selected from articles [B40, B41]. In addition, the bone was considered as a non-diffusive material. Table B-3 lists the respective values.

TABLE B-3 DIFFUSIVITY COEFFICIENT OF LUNG MODEL

	Diffusivity ($10^{-3}\text{mm}^2\text{s}^{-1}$)
Lung tissue	1.00
Bone	0

No diffusion boundary was considered for the outer surface of the lung tissue (Neumann boundary condition). The concentration of tumour cells obtained from cellular simulation on the tumour boundary and inside the lung tissue was applied as an initial boundary condition for the simulation. The original tumour was constrained so as to have a constant concentration of cells ($1\text{e}+6\text{Cells.mm}^3$).

B5.2.2 Mechanics

Material properties of the linear elastic lung were taken from [B42]. Due to the lack of information for a variety of lung tumours, we have considered the tumour to have material properties identical to healthy lung tissue, Table B-4.

TABLE B-4 8: MECHANICAL PROPERTIES OF ELASTIC LUNG

	Young's modulus (Pa)	Poisson ratio
Lung tissue	961	0.4
Bone	1E10	0.3
Tumour	961	0.4

The long time-scale of the biomechanical simulation allowed respiratory and vascular motion to be neglected. To apply the boundary condition, the outer surface of the mesh was fully constrained.

B5.3 Biomechanics Results

Mechanical stress and displacement magnitude are shown in Fig. B4 for a realistic tumour inside the lung, solved merely for the mass effect. In this simulation, the effect of the tumorous cell diffusion is neglected and only the effect of mechanical interaction between tumour growth and healthy lung tissue is studied.

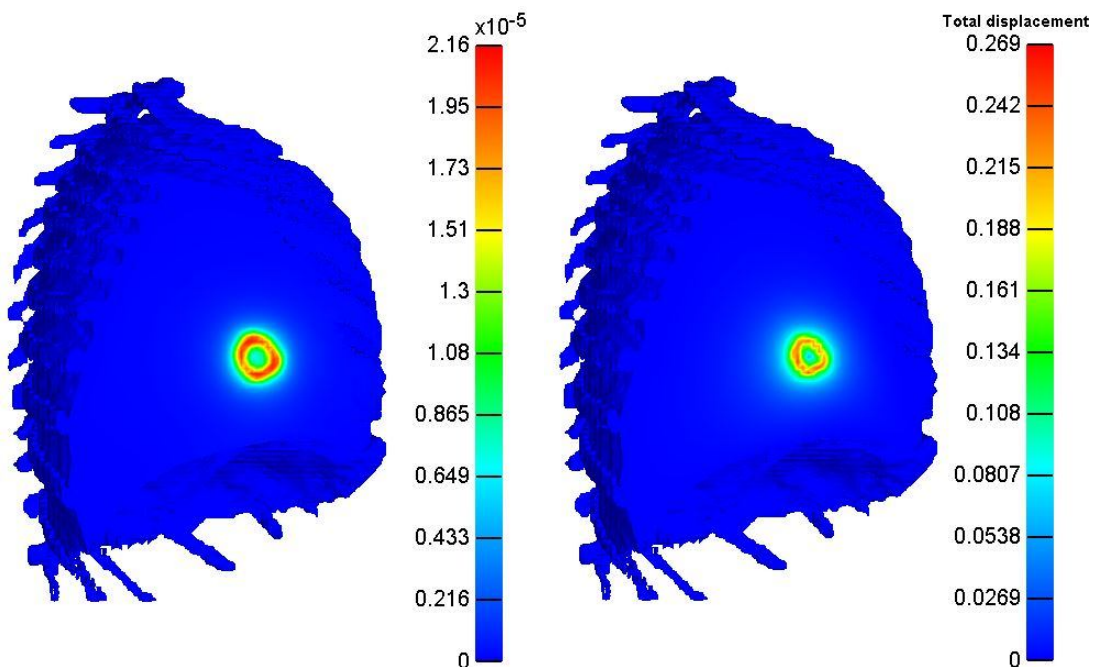


Fig. B6 Stress distribution [mpa] (left) and magnitude of displacement [mm](right) due to the growth of the tumour inside the lung

Compare the results of mechanical interaction of tumour growth inside a healthy lung with the growth in brain tissue (shown in Fig. B5), more symmetric distribution of variables are observed in the lung. This is expected due to uniformity of the lung tissue and due to the large distance between the location of tumour growth and the boundaries. On the other hand, inside the brain, stress and displacement magnitudes are very asymmetric due to differing material properties of grey and white matter, as well as ventricles filled with cerebrospinal fluid (CSF). Tumour growth is sensitive to boundaries and changes in material properties in its proximity, so that a non-spherical tumour shape is expected in that body region.

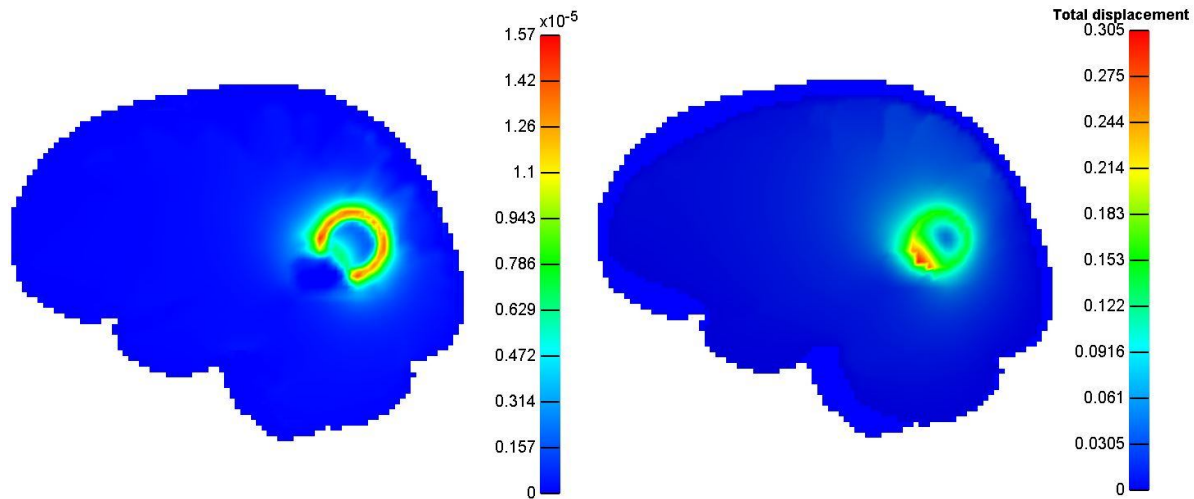


Fig.B7 : stress distribution [mpa] (left) and magnitude of displacement [mm] (right) due to the growth of the tumour inside the brain. the y are more asymmetric due to non-uniformity of the domain and proximity of the boundaries

B6. Conclusions

A generic Biomechanical and Diffusion model has been developed to simulate effects of the interaction of tumour and healthy tissue. In combination with a sub-cellular biological model of cell proliferation and cellular response to therapeutic agents, in-situ tumour development can be simulated.

An initial prototype of the biomechanical model was implemented as 'Biomechanical Simulator', employing a well-established Finite Element Solver as computational back-end. This solver was modified to consider the mass effect as a result of tumour growth in the material property, so that its mechanical effect on the healthy tissue can be simulated. The Biomechanical Simulator was coupled to an initial version of the ICCS cellular growth simulator and tested on realistic brain and lung tumours.

Patient-specific computational models of the region of interest were created automatically using an in-house developed meshing tool. Based on these models, biomechanical effects of tumour growth were compared for these two anatomical locations. First results indicate that displacement and stress distribution maps caused by tumours in the lung are more symmetric than those caused by tumours in the brain due to higher tissue homogeneity in the proximity of the tumour and a larger

distance to constraining boundaries. Growth under those conditions is expected to result in more symmetric geometrical shapes.

B6.1 Future Work

Full simulation of the effects of diffusion on tumour growth requires the distribution map of cellular concentrations to be updated by both Biomechanics and Cell Simulator and to be exchanged between them, as indicated in Fig. B2. We plan to be working towards the development of a suitable mapping approach and tool in close collaboration with ICCS. Considering the recurring nature of coordinate and element property mappings between inputs and outputs of distinct computational models, a generic solution may be envisaged with support of WP7. Likewise, other interfaces of the Biomechanics Simulator tool to hypomodel-simulators within EU-CHIC and to validated third-party computational engines will require further standardisation.

B7. Appendix

B7.1 Mechanics

As the material law is based on the theory of finite elasticity, a preliminary introduction of this theory is presented here.

When an elastic body is deformed by an external force, the work done by the force is stored in the form of strain energy within the body. When the material undergoes a small strain, the Kirchhoff-St Venant hyper-elastic model can be considered. The function of energy density for this model, W , is presented in equation (BI)

$$W = \frac{\lambda}{2} \text{Trace}(\mathbf{E})^2 + \mu \text{Trace}(\mathbf{E}^2) \quad (\text{BI})$$

Where \mathbf{E} is the Lagrange-Green strain tensor, and λ and μ are the Lamé constants which represent the mechanical properties of the material. These constants are directly related to the relevantly-used material-dependent constants named the Young's modulus (E) and Poisson ratio (ν) as presented in equation (BII) .

$$\lambda = \frac{\nu E}{(1 + \nu)(1 - 2\nu)} , \quad \mu = \frac{E}{2(1 + \nu)} \quad (\text{BII})$$

For an isotropic linear elastic body, the stress vector, as a derivative of energy density function with respect to Lagrange-Green strain tensor, is defined by the known Hook's law. This yields to the following stress/strain relationship:

$$\mathbf{S} = \lambda \text{Trace}(\mathbf{E})\mathbf{I} + 2\mu\mathbf{E} \quad (\text{BIII})$$

Writing this equation in more explicit way using a matrix format gives:

$$\begin{pmatrix} \mathbf{S}_{xx} \\ \mathbf{S}_{yy} \\ \mathbf{S}_{zz} \\ \mathbf{S}_{xy} \\ \mathbf{S}_{yz} \\ \mathbf{S}_{xz} \end{pmatrix} = \frac{E}{(1+\nu)(1-2\nu)} \begin{pmatrix} 1-\nu & \nu & \nu & 0 & 0 & 0 \\ \nu & 1-\nu & \nu & 0 & 0 & 0 \\ \nu & \nu & 1-\nu & 0 & 0 & 0 \\ 0 & 0 & 0 & \frac{(1-2\nu)}{2} & 0 & 0 \\ 0 & 0 & 0 & 0 & \frac{(1-2\nu)}{2} & 0 \\ 0 & 0 & 0 & 0 & 0 & \frac{(1-2\nu)}{2} \end{pmatrix} \begin{pmatrix} \mathbf{E}_{xx} \\ \mathbf{E}_{yy} \\ \mathbf{E}_{zz} \\ 2\mathbf{E}_{xy} \\ 2\mathbf{E}_{yz} \\ 2\mathbf{E}_{xz} \end{pmatrix} \quad (\text{BIV})$$

Where \mathbf{E}_{xx} , \mathbf{E}_{yy} and \mathbf{E}_{zz} are the three normal components of the strain, and \mathbf{E}_{xy} , \mathbf{E}_{yz} and \mathbf{E}_{xz} are the shear components. Similarly, \mathbf{S}_{xx} , \mathbf{S}_{yy} and \mathbf{S}_{zz} are normal stress components and \mathbf{S}_{xy} , \mathbf{S}_{yz} and \mathbf{S}_{xz} are the remaining three shear components of the stress vector.

To model the growth, the volume change is considered to be a uniform-and-isentropic strain added in the normal direction of elastic formulation for each element. The growth could be interpreted as an internal pressure of the tissue. The strain formulation is updated as in equation (BV)

$$\mathbf{E} = \mathbf{E}_{\text{MECH}} - \mathbf{E}_{\text{GROWTH}} \quad (\text{BV})$$

Where \mathbf{E}_{MECH} and $\mathbf{E}_{\text{GROWTH}}$ are the mechanical and growth component of the strain vector, respectively. The mass effect is then simulated modifying the stress tensor, which is presented in equation (BVI).

$$\text{Trace } \mathbf{E} = \mathbf{E}_{xx} + \mathbf{E}_{yy} + \mathbf{E}_{zz} - (3 * \mathbf{E}_{\text{GROWTH}}) \quad (\text{BVI})$$

Updating the stress tensor, the strain energy function leads to the following constitutive equations:

$$\begin{aligned} \mathbf{S}_{xx} &= \lambda * \text{tr} \mathbf{E} + 2 * \mu * (\mathbf{E}_{xx} - \mathbf{E}_{\text{growth}}) \\ \mathbf{S}_{yy} &= \lambda * \text{tr} \mathbf{E} + 2 * \mu * (\mathbf{E}_{yy} - \mathbf{E}_{\text{growth}}) \\ \mathbf{S}_{zz} &= \lambda * \text{tr} \mathbf{E} + 2 * \mu * (\mathbf{E}_{zz} - \mathbf{E}_{\text{growth}}) \\ \mathbf{S}_{xy} &= 2 * \mu * (\mathbf{E}_{xy}) \\ \mathbf{S}_{yz} &= 2 * \mu * (\mathbf{E}_{yz}) \\ \mathbf{S}_{xz} &= 2 * \mu * (\mathbf{E}_{xz}) \end{aligned} \quad (\text{BVII})$$

B8. References

- B1. American, Cancer, and Society, *Cancer Facts & Figures 2014*. Atlanta: American Cancer Society, 2014.
- B2. A. Jemal, F. Bray, M. M. Center, J. Ferlay, E. Ward, and D. Forman, "Global cancer statistics," *CA: A Cancer Journal for Clinicians*, vol. 61, no. 2, pp. 69–90, Mar. 2011.
- B3. R. Werner, J. Ehrhardt, R. Schmidt, and H. Handels, "Patient-specific finite element modeling of respiratory lung motion using 4D CT image data," *Med Phys*, vol. 36, no. 5, pp. 1500–1511, May 2009.
- B4. A. Al-Mayah, J. Moseley, M. Velec, and K. K. Brock, "Sliding characteristic and material compressibility of human lung: Parametric study and verification," *Medical Physics*, vol. 36, no. 10, pp. 4625–4633, Oct. 2009.
- B5. Li, G., D. Citrin, K. Camphausen, B. Mueller, C. Burman, B. Mychalczak, R. W. Miller, and Y. Song. "Advances in 4D Medical Imaging and 4D Radiation Therapy." *Technology in Cancer Research & Treatment* 7, no. 1 (February 2008): 67–81.
- B6. T. A. Sundaram and J. C. Gee, "Towards a model of lung biomechanics: pulmonary kinematics via registration of serial lung images," *Med Image Anal*, vol. 9, no. 6, pp. 524–537, Dec. 2005.
- B7. B. Suki and J. H. T. Bates, "Lung tissue mechanics as an emergent phenomenon," *J. Appl. Physiol.*, vol. 110, no. 4, pp. 1111–1118, Apr. 2011.
- B8. A. Baydur, "Pulmonary physiology in interstitial lung disease: recent developments in diagnostic and prognostic implications," *Curr Opin Pulm Med*, vol. 2, no. 5, pp. 370–375, Sep. 1996.
- B9. J. H. T. Bates, G. S. Davis, A. Majumdar, K. J. Butnor, and B. Suki, "Linking parenchymal disease progression to changes in lung mechanical function by percolation," *Am. J. Respir. Crit. Care Med.*, vol. 176, no. 6, pp. 617–623, Sep. 2007.
- B10. S. E. Gay, E. A. Kazerooni, G. B. Toews, J. P. Lynch, B. H. Gross, P. N. Cascade, D. L. Spitzarny, A. Flint, M. A. Schork, R. I. Whyte, J. Popovich, R. Hyzy, and F. J. Martinez, "Idiopathic pulmonary fibrosis: predicting response to therapy and survival," *Am. J. Respir. Crit. Care Med.*, vol. 157, no. 4 Pt 1, pp. 1063–1072, Apr. 1998.
- B11. S. J. Lai-Fook and R. E. Hyatt, "Effects of age on elastic moduli of human lungs," *J. Appl. Physiol.*, vol. 89, no. 1, pp. 163–168, Jul. 2000.
- B12. S. Liu, S. S. Margulies, and T. A. Wilson, "Deformation of the dog lung in the chest wall," *J. Appl. Physiol.*, vol. 68, no. 5, pp. 1979–1987, May 1990.
- B13. R. De Wilde, J. Clément, J. M. Hellemans, M. Decramer, M. Demedts, R. Boving, and K. P. Van de Woestijne, "Model of elasticity of the human lung," *J Appl Physiol Respir Environ Exerc Physiol*, vol. 51, no. 2, pp. 254–261, Aug. 1981.
- B14. K. Suga, T. Tsukuda, H. Awaya, K. Takano, S. Koike, N. Matsunaga, K. Sugi, and K. Esato, "Impaired respiratory mechanics in pulmonary emphysema: evaluation with dynamic breathing MRI," *J Magn Reson Imaging*, vol. 10, no. 4, pp. 510–520, Oct. 1999.
- B15. M. Paiva, S. Verbanck, M. Estenne, B. Poncelet, C. Segebarth, and P. T. Macklem, "Mechanical implications of in vivo human diaphragm shape," *J. Appl. Physiol.*, vol. 72, no. 4, pp. 1407–1412, Apr. 1992.

- B16. J. Mead, T. Takishima, and D. Leith, "Stress distribution in lungs: a model of pulmonary elasticity.," *Journal of Applied Physiology*, vol. 28, no. 5, pp. 596–608, May 1970.
- B17. V. J. Napadow, V. Mai, A. Bankier, R. J. Gilbert, R. Edelman, and Q. Chen, "Determination of regional pulmonary parenchymal strain during normal respiration using spin inversion tagged magnetization MRI," *J Magn Reson Imaging*, vol. 13, no. 3, pp. 467–474, Mar. 2001.
- B18. J. Cai, K. Sheng, S. H. Benedict, P. W. Read, J. M. Larner, J. P. Mugler, E. E. de Lange, G. D. Cates, and G. W. Miller, "Dynamic MRI of grid-tagged hyperpolarized helium-3 for the assessment of lung motion during breathing," *Int. J. Radiat. Oncol. Biol. Phys.*, vol. 75, no. 1, pp. 276–284, Sep. 2009.
- B19. Murphy, B. van Ginneken, J. M. Reinhardt, S. Kabus, K. Ding, X. Deng, K. Cao, K. Du, G. E. Christensen, V. Garcia, T. Vercauteren, N. Ayache, O. Commowick, G. Malandain, B. Glocker, N. Paragios, N. Navab, V. Gorbunova, J. Sporring, M. de Bruijne, X. Han, M. P. Heinrich, J. A. Schnabel, M. Jenkinson, C. Lorenz, M. Modat, J. R. McClelland, S. Ourselin, S. E. A. Muenzing, M. A. Viergever, D. De Nigris, D. L. Collins, T. Arbel, M. Peroni, R. Li, G. C. Sharp, A. Schmidt-Richberg, J. Ehrhardt, R. Werner, D. Smeets, D. Loeckx, G. Song, N. Tustison, B. Avants, J. C. Gee, M. Staring, S. Klein, B. C. Stoel, M. Urschler, M. Werlberger, J. Vandemeulebroucke, S. Rit, D. Sarrut, and J. P. W. Pluim, "Evaluation of registration methods on thoracic CT: the EMPIRE10 challenge," *IEEE Trans Med Imaging*, vol. 30, no. 11, pp. 1901–1920, Nov. 2011.
- B20. B. Fuerst, T. Mansi, P. Khurd, J. Zhang, J. Declerck, T. Boettger, N. Navab, J. Bayouth, and A. Kamen, "Patient-specific finite-element simulation of respiratory mechanics for radiotherapy guidance, a first evaluation study," in *2012 9th IEEE International Symposium on Biomedical Imaging (ISBI)*, 2012, pp. 1212–1215.
- B21. R. Werner, J. Ehrhardt, A. Schmidt-Richberg, and H. Handels, "Validation and comparison of a biophysical modeling approach and non-linear registration for estimation of lung motion fields in thoracic 4D CT data," 2009, p. 8.
- B22. P. Villard, M. Beuve, B. Shariat, V. Baudet, and F. Jalliet, "Simulation of lung behaviour with finite elements: influence of bio-mechanical parameters," in *Third International Conference on Medical Information Visualisation - Biomedical Visualisation*, 2005. (MediVis 2005). Proceedings, 2005, pp. 9–14.
- B23. P. J. Keall, G. S. Mageras, J. M. Balter, R. S. Emery, K. M. Forster, S. B. Jiang, J. M. Kapatoes, D. A. Low, M. J. Murphy, B. R. Murray, C. R. Ramsey, M. B. Van Herk, S. S. Vedam, J. W. Wong, and E. Yorke, "The management of respiratory motion in radiation oncology report of AAPM Task Group 76," *Med Phys*, vol. 33, no. 10, pp. 3874–3900, Oct. 2006.
- B24. A. Mohamed and C. Davatzikos, "Finite Element Modeling of Brain Tumour Mass-Effect from 3D Medical Images," in *Medical Image Computing and Computer-Assisted Intervention – MICCAI 2005*, J. S. Duncan and G. Gerig, Eds. Springer Berlin Heidelberg, 2005, pp. 400–408.
- B25. S. P. Chakrabarty and F. B. Hanson, "Distributed parameters deterministic model for treatment of brain tumours using Galerkin finite element method," *Math Biosci*, vol. 219, no. 2, pp. 129–141, Jun. 2009.
- B26. F. B. Hanson and C. Tier, "A stochastic model of tumour growth," *Mathematical Biosciences*, vol. 61, no. 1, pp. 73–100, Sep. 1982.
- B27. P. Tracqui, "From passive diffusion to active cellular migration in mathematical models of tumour invasion," *Acta Biotheor.*, vol. 43, no. 4, pp. 443–464, Dec. 1995.

- B28. Z. Shirzadi, A. Sadeghi Naini, and A. Samani, "Lung tumour motion prediction during lung brachytherapy using finite element model," 2012, vol. 8316, p. 83160I–83160I–8.
- B29. S. K. Warfield, F. Talos, A. Tei, A. Bharatha, A. Nabavi, M. Ferrant, P. Mcl, F. A. Jolesz, and R. Kikinis, Real-Time Registration of Volumetric Brain MRI by Biomechanical Simulation of Deformation during Image Guided Neurosurgery. 2002.
- B30. C. Hogue, C. Davatzikos, and G. Biros, "An image-driven parameter estimation problem for a reaction-diffusion glioma growth model with mass effects," *J Math Biol*, vol. 56, no. 6, pp. 793–825, Jun. 2008.
- B31. R. Wasserman, R. Acharya, C. Sibata, and K. H. Shin, "A patient-specific in vivo tumour model," *Mathematical Biosciences*, vol. 136, no. 2, pp. 111–140, Sep. 1996.
- B32. O. Clatz, M. Sermesant, P.-Y. Bondiau, H. Delingette, S. K. Warfield, G. Malandain, and N. Ayache, "Realistic Simulation of the 3D Growth of Brain Tumours in MR Images Coupling Diffusion with Biomechanical Deformation," *IEEE Trans Med Imaging*, vol. 24, no. 10, pp. 1334–1346, Oct. 2005.
- B33. E. Konukoglu, M. Sermesant, O. Clatz, J.-M. Peyrat, H. Delingette, and N. Ayache, "A Recursive Anisotropic Fast Marching Approach to Reaction Diffusion Equation: Application to Tumour Growth Modeling," in *Information Processing in Medical Imaging*, N. Karssemeijer and B. Lelieveldt, Eds. Springer Berlin Heidelberg, 2007, pp. 687–699.
- B34. A. H. Juffer, U. Marin, O. Niemitalo, and J. Koivukangas, "Computer modeling of brain tumour growth," *Mini Rev Med Chem*, vol. 8, no. 14, pp. 1494–1506, Dec. 2008.
- B35. S. G. Armato, G. McLennan, L. Bidaut, M. F. McNitt-Gray, C. R. Meyer, A. P. Reeves, B. Zhao, D. R. Aberle, C. I. Henschke, E. A. Hoffman, E. A. Kazerooni, H. MacMahon, E. J. R. Van Beeke, D. Yankelevitz, A. M. Biancardi, P. H. Bland, M. S. Brown, R. M. Engelmann, G. E. Laderach, D. Max, R. C. Pais, D. P. Y. Qing, R. Y. Roberts, A. R. Smith, A. Starkey, P. Batrah, P. Caligiuri, A. Farooqi, G. W. Gladish, C. M. Jude, R. F. Munden, I. Petkovska, L. E. Quint, L. H. Schwartz, B. Sundaram, L. E. Dodd, C. Fenimore, D. Gur, N. Petrick, J. Freymann, J. Kirby, B. Hughes, A. V. Castelee, S. Gupte, M. Sallamm, M. D. Heath, M. H. Kuhn, E. Dharaiya, R. Burns, D. S. Fryd, M. Salganicoff, V. Anand, U. Shreter, S. Vastagh, and B. Y. Croft, "The Lung Image Database Consortium (LIDC) and Image Database Resource Initiative (IDRI): a completed reference database of lung nodules on CT scans," *Med Phys*, vol. 38, no. 2, pp. 915–931, Feb. 2011.
- B36. S. J. Hollister and B. A. Riemer, "Digital-image-based finite element analysis for bone microstructure using conjugate gradient and Gaussian filter techniques," 1993, vol. 2035, pp. 95–106.
- B37. S. K. Boyd and R. Müller, "Smooth surface meshing for automated finite element model generation from 3D image data," *J Biomech*, vol. 39, no. 7, pp. 1287–1295, 2006.
- B38. G. Taubin, "A Signal Processing Approach to Fair Surface Design," in *Proceedings of the 22Nd Annual Conference on Computer Graphics and Interactive Techniques*, New York, NY, USA, 1995, pp. 351–358.
- B39. S. A. Maas, B. J. Ellis, G. A. Ateshian, and J. A. Weiss, "FEBio: finite elements for biomechanics," *J Biomech Eng*, vol. 134, no. 1, p. 011005, Jan. 2012.
- B40. L. Chen, J. Zhang, Y. Chen, W. Wang, X. Zhou, X. Yan, and J. Wang, "Relationship between Apparent Diffusion Coefficient and Tumour Cellularity in Lung Cancer," *PLoS ONE*, vol. 9, no. 6, p. e99865, Jun. 2014.

- B41. A. A. K. A. Razek, A. Fathy, and T. A. Gawad, "Correlation of apparent diffusion coefficient value with prognostic parameters of lung cancer," *J Comput Assist Tomogr*, vol. 35, no. 2, pp. 248–252, Apr. 2011.
- B42. S. Ganesan, K. E. Rouch, and S. J. Lai-Fook, "A finite element analysis of the effects of the abdomen on regional lung expansion," *Respir Physiol*, vol. 99, no. 3, pp. 341–353, Mar. 1995.
- B43. C. P. May, E. Kolokotroni, G. S. Stamatakis, and P. Büchler, "Coupling biomechanics to a cellular level model: an approach to patient-specific image driven multi-scale and multi-physics tumour simulation," *Prog. Biophys. Mol. Biol.*, vol. 107, no. 1, pp. 193–199, Oct. 2011.
- B44. K. Marias, D. Dionysiou, V. Sakkalis, N. Graf, R. M. Bohle, P. V. Coveney, S. Wan, A. Folarin, P. Büchler, M. Reyes, G. Clapworthy, E. Liu, J. Sabczynski, T. Bily, A. Roniotis, M. Tsiknakis, E. Kolokotroni, S. Giatili, C. Veith, E. Messe, H. Stenzhorn, Y.-J. Kim, S. Zasada, A. N. Haidar, C. May, S. Bauer, T. Wang, Y. Zhao, M. Karasek, R. Grewer, A. Franz, and G. Stamatakis, "Clinically driven design of multi-scale cancer models: the ContraCancrum project paradigm," *Interface Focus*, vol. 1, no. 3, pp. 450–461, Jun. 2011.
- B45. S. Bauer, C. May, D. Dionysiou, G. Stamatakis, P. Büchler, and M. Reyes, "Multiscale modeling for image analysis of brain tumour studies," *IEEE Trans Biomed Eng*, vol. 59, no. 1, pp. 25–29, Jan. 2012.
- B46. S. Bauer, H. Lu, C. P. May, L.-P. Nolte, P. Büchler, and M. Reyes, "Integrated segmentation of brain tumour images for radiotherapy and neurosurgery," *Int. J.*
- B47. G.S.Stamatakis, V.P.Antipas, and N.K. Uzunoglu , A spatiotemporal, patient individualized simulation model of solid tumor response to chemotherapy in vivo: the paradigm of glioblastoma multiforme treated by temozolomide , *IEEE Transactions on Biomedical Engineering* , 53(8) , 1467-1477 , 2006
- B48. G.Stamatakis "In Silico Oncology Part I: Clinically Oriented Cancer Multilevel Modeling Basedon Discrete Event Simulation" In T.Deisboeck and G. Stamatakis Eds 407-436 2011-01-01 CRC Press, Print ISBN: 978-1-4398-1440-6 eBook ISBN: 978-1-4398-1442-0 DOI: 10.1201/b10407-19 Boca Raton, Florida, USA, 2011

B9. Description of the The Tumour Growth Biomechanics Component Model (B) through the 13 Perspectives

TABLE "B-13P" (FIRST PART)		
PERSPECTIVE CODE NUMBER	PERSPECTIVE TITLE	PERSPECTIVE VALUE(S)
I	TUMOUR-AFFECTED NORMAL TISSUE MODELLING	tumour normal tissue
II	SPATIAL SCALE(S) OF THE MANIFESTATION OF LIFE	tissue organ
III	TEMPORAL SCALE(S) OF THE MANIFESTATION OF LIFE	h d
IV	BIOMECHANISM(S) ADDRESSED	tissue mechanics tissue deformation
V	TUMOUR TYPE(S) ADDRESSED	lung cance other solid tumours
VI	TREATMENT MODALITY(-IES) ADDRESSED	no treatment consideration

TABLE "B-13P" (SECOND PART)		
PERSPECTIVE CODE NUMBER	PERSPECTIVE TITLE	PERSPECTIVE VALUE(S)
VII	GENERIC CANCER BIOLOGY – CLINICALLY DRIVEN CHARACTER OF THE MODELLING APPROACH	generic cancer biology clinically driven
VIII	ORDER OF ADDRESSING DIFFERENT SPATIAL SCALES	bottom-up top-down
IX	ORDER OF ADDRESSING DIFFERENT TEMPORAL SCALES	short periods → longer periods,
X	MECHANISTIC-STATISTICAL CHARACTER OF THE MODELLING APPROACH	mechanistic
XI	DETERMINISTIC-STOCHASTIC CHARACTER OF THE MODELLING APPROACH	deterministic
XII	CONTINUOUS-FINITE-DISCRETE CHARACTER OF THE MATHEMATICS INVOLVED	continuous finite (finitized continuous)
XIII	CLOSED FORM SOLUTION – ALGORITHMIC SIMULATION MODELLING APPROACH	algorithmic simulation

M. The Subcellular (Atomistic and Molecular) Component Models

M1. Introduction

The grand challenge in bridging cancer genomics with oncology is to customize individual patient therapy to the genomic status of the patient (such as the presence of mutations or copy number variations). With the objective of linking the mutational status of oncogenic proteins (such as the epidermal growth factor receptor or EGFR, anaplastic lymphoma kinase or Alk, etc.) to the efficacy of small molecule inhibition of these proteins, a series of subcellular models have been developed at UPENN (see Fig. M1 and Table M-1). These subcellular component models from UPENN will connect with the other components of the multi-modeller through the determination of how drug concentration and mutational status of the oncogenic protein EGFR impact the cell kill rate. A brief schematic of the sub-cellular components is provided below (with details discussed later in the text) along with a summary of the input and output from these models described in Table M-1. The sub-cellular component is integrated as three distinct hyper-models (levels), which then get integrated with the multi-modeller hyper model through an integration layer, see Fig. M1.

M2. Layer 1

Level 1 or the Structural Atomistic Level is based on molecular modeling and dynamics simulations. Highlights of what has been achieved by modeling at this level are: (1) based on the crystal structure of the protein and homology modeling, we constructed a solvated model of the receptor (EGFR dimer) and carried out molecular dynamics and metadynamics simulations of various mutants of EGFR. (2) Through an analysis of hydrogen bonding and hydrophobic interactions, we have devised an activation-score for predicting the propensity of activation of the kinase for a given mutant. The input to this model is the crystal structure and the force-field parameters, and the output are the trajectories and the activation scores for each mutant analyzed. (3) We also carry out molecular docking simulations to investigate the effect of mutations on drug binding affinity.

M3. Layer 2

Level 2 or the Molecular Association Level comprises of a machine learning and predictive algorithm for profiling benign and oncogenic mutations in signaling proteins. Highlights of what has been achieved in this level include: (1) based on support vector machine and partial least square regression, we have developed a machine learning algorithm that takes as input the activation scores and the trajectories. The output or prediction includes: (2) a correlated kinetics parameter k_{cat}/K_M that reflects the activity of a given mutant; (3) the likelihood of activation a particular mutation in a given protein across the human kinome.

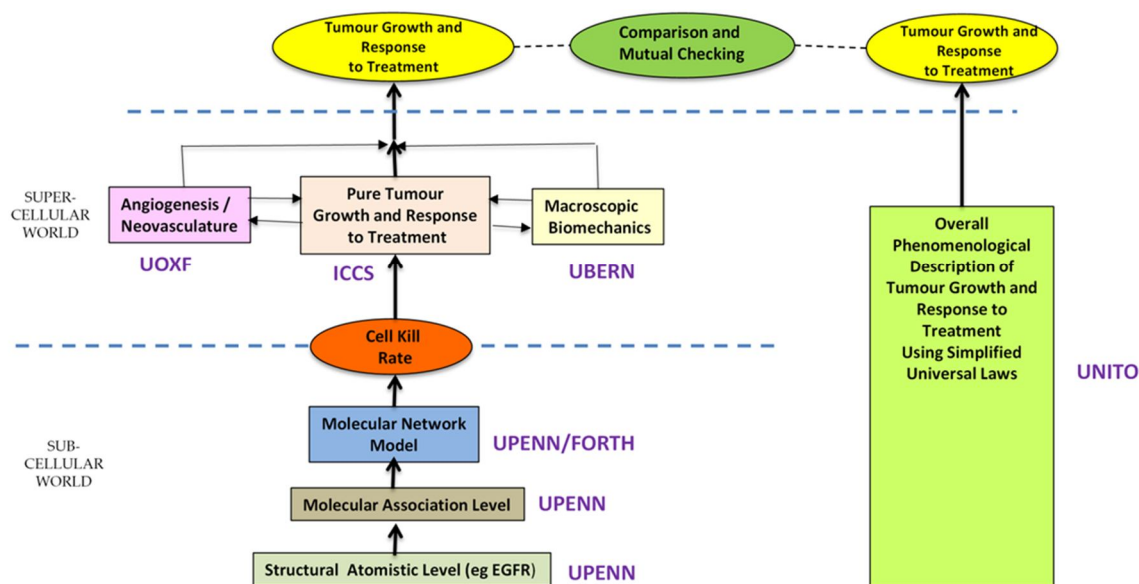
M4. Layer 3

Level 3 or the Molecular Network Level establishes network models for EGFR signaling that are specific to each mutant. The input to the layer is an SBML file with topology and parameters of the EGFR mediated signal transduction including the Erk, Akt, Stat, and EGFR-trafficking pathways. In each case, modifying the activation, dimerization, drug binding, and trafficking characteristics of the mutant, we constructed a mutant specific signaling pathway. The input to these modifications is generated through a combination of experiments and molecular modeling (such as protein-drug

docking simulations). The output of the network model is the activation of Erk/Akt ratio and Erk/Stat ratio for each EGFR mutant and as a function of drug concentration. These ratios are utilized to make a prediction on cell kill rate.

M5. Integration Layer

Integration Layer to predict Cell-Kill-Rate: This layer serves as an interface between the three subcellular level and the overall multi modeler, see Fig M1. It utilizes a partial-least-squares model developed at MIT (published and available for use) that takes as input the Erk/Akt and Erk/Stat ratios from level 3 and provides as output the normalized propensity of cell apoptosis for a given mutant and a given drug concentration.



CHIC WP6 MASTER TOPOLOGY OF THE LUNG CANCER
MULTI-MODELLER HYPERMODEL

Fig. M1 Schematic of the multi-modeller hyper model.

M6. Testing, Implementation, and Integration of the Subcellular Models

TABLE M-1 SUMMARY OF TESTING, IMPLEMENTATION, AND INTEGRATION OF THE SUBCELLULAR MODELS

	Input	Output	Connection to multi-modeller hyper model	Reference where model has been tested
Layer 1 or Structural Atomistic Level: Molecular Model (UPENN)	Structure, Force-field parameters	Trajectories, activation score (specific kinase, mutant); binding free energy of drug with mutant proteins	Layer 1 feeds Layer 2	(a-i)
<p>a. Molecular Dynamics Analysis of Conserved Hydrophobic and Hydrophilic Bond Interaction Networks in ErbB Family Kinases, A. Shih, S. E. Telesco, S. H. Choi, M. A. Lemmon, R. Radhakrishnan, <i>Biochemical Journal</i>, 2011, 436(2), 241-251.</p> <p>b. Analysis of Somatic Mutations in Cancer: Molecular Mechanisms of Activation in the ErbB family of Receptor Tyrosine Kinases, A. J. Shih, S. E. Telesco, R. Radhakrishnan, <i>Cancers</i>, 2011, 3(1), 1195-1231; doi:10.3390/cancers3011195. Pubmed ID: 21701703.</p> <p>c. Erlotinib binds both inactive and active conformations of the EGFR tyrosine kinase domain, J. H. Park¹, Y. Liu¹, M. A. Lemmon*, R. Radhakrishnan*, <i>Biochem J.</i>, 2012, 448(3), 417-423; 1. Equal contribution, * co-corresponding authors. (DOI: 10.1042/BJ20121513). (Pubmed ID: 23101586)</p> <p>d. The ErbB3/HER3 Intracellular Domain is Competent to Bind ATP and Catalyze Autophosphorylation, F. Shi, S. E. Telesco, Y. Liu, R. Radhakrishnan*, M. A. Lemmon*, <i>Proceedings of the National Academy of Sciences</i>, 107, 7692-7697, 2010. Pubmed ID: 20351256; *Co-corresponding authors.</p> <p>e. Erlotinib binds both inactive and active conformations of the EGFR tyrosine kinase domain, J. H. Park¹, Y. Liu¹, M. A. Lemmon*, R. Radhakrishnan*, <i>Biochem J.</i>, 2012, 448(3), 417-423; 1. Equal contribution, * co-corresponding authors. (DOI: 10.1042/BJ20121513). (Pubmed ID: 23101586)</p> <p>f. A molecular docking study of the binding of ruthenium complex compounds to PIM1, GSK3, and CDK2 protein kinases, Y. Liu, N. J. Agrawal, R. Radhakrishnan, <i>J. Molecular Modeling</i>, 2013, 19, 371-382. DOI 10.1007/s00894-012-1555-4.</p> <p>g. Computational Delineation of Tyrosyl-Substrate Recognition and Catalytic Landscapes in the Epidermal Growth Factor Receptor Tyrosine Kinase Domain, Y. Liu, R. Radhakrishnan, <i>Molecular Biosystems</i>, 2014, 10, 1890-1904. DOI: 10.1039/C3MB70620F</p> <p>h. Integrative functional assessment of ALK mutations for therapeutic stratification in neuroblastoma, D. Weiser, S. Bressler, P. J. Huwe, R. Radhakrishnan, M. A. Lemmon, Y. Mosse, <i>Cancer Cell</i>, 2014, 26, 682-694. DOI: 10.1016/j.ccell.2014.09.019.</p> <p>i. Computational Methodology for Mechanistic Profiling of Kinase Domain Mutations in Cancers, P. J. Huwe, and R. Radhakrishnan, <i>Proceedings of the IEEE, 5th International Advanced Research Workshop on In Silico Oncology and Cancer Investigation</i>, Eds. G. S. Stamatakis, D. D. Dionysiou, 2013, pp1-4. Print ISBN: 978-1-4673-5024-2. An open access version of the article is also available at http://www.5th-iarwisoci.iccs.ntua.gr/ and through IEEE Xplore library, http://ieeexplore.ieee.org/xpl/tocresult.jsp?reload=true&isnumber=6397169.</p>				
Layer 2 or Molecular Association Level: Machine Learning Algorithm (UPENN)	Activation score from molecular model, literature data on protein sequence (Uniprot database,	Activation score (all kinases, mutants), kcat (kinetics constant) for specific kinase, mutant	Layer 2 accepts input from Layer 1 and feeds Layer 3.	(j)

	COSMIC database, TCGA database)			
j. Machine learning predictions of cancer driver mutations, E. Jordan, R. Radhakrishnan, IEEE Proceedings of the 6 th International Advanced Research Workshop on In Silico Oncology and Cancer Investigation, 2014, in press.				
Layer 3 or Molecular Network Level: Network Model (UPENN)	Protein interaction topology, binding and kinetic parameters including those altered due to mutations obtained from machine learning algorithm	Time course for protein activation, ERK/Akt; ERK/STAT activation ratio	Layer 3 accepts input from Layer 2 and feeds the integration Layer. The main output to the integration layer is the cell proliferation rate for each mutation examined in molecular model	(k-p)
k. Role of Network Branching in Eliciting Differential Short-Term Signaling Responses in the Hyper-Sensitive Epidermal Growth Factor Receptor Mutants Implicated in Lung Cancer, J. Purvis, V. Ilango, R. Radhakrishnan, <u>Biotechnology Progress</u> , 24: 540-553, 2008.				
l. Highlight Article: Molecular Systems Biology of ErbB1 Signaling: Bridging the Gap through Multiscale Modeling and High-Performance Computing, Andrew Shih, Jeremy Purvis, R. Radhakrishnan, <u>Molecular Biosystems</u> (A Royal Society of Chemistry Journal), 4: 1151-1159, 2008.				
m. A Multiscale Modeling Approach to Investigate Molecular Mechanisms of Pseudokinase Activation and Drug Resistance in the HER3/ErbB3 Receptor Tyrosine Kinase Signaling Network, S. E. Telesco, A. J. Shih, F. Jia, R. Radhakrishnan, <u>Molecular Biosystems (RSC Journal)</u> , 2011, 7 (6), 2066 - 2080. DOI: 10.1039/c0mb00345j.				
n. Structural Systems Biology and Multiscale Signaling Models, S. E. Telesco, R. Radhakrishnan, <u>Annals of Biomedical Engineering</u> , 2012, 40(11), 2295–2306. Pubmed ID: 22539148.				
o. Linking oncogenic signaling to molecular structure, <u>Multiscale Cancer Modeling</u> , J. Purvis, A. Shih, Y. Liu, R. Radhakrishnan, Eds. T.S. Deisboeck, G. Stamatakis, Chapman & Hall-CRC Mathematical and Computational Biology Series, 2011, pp31-43.				
p. Molecular Modeling of the ErbB4/HER4 Kinase in the Context of the HER4 Signaling Network Helps Rationalize the Effects of Clinically Identified HER4 Somatic Mutations on the Cell Phenotype, S. E. Telesco, R. Vadigepalli, R. Radhakrishnan, <u>Biotechnology Journal</u> , 2013, 8, 1452-1464. (Also featured in Editorial and “In this Issue” segments). DOI: 10.1002/biot.201300022				
Integration Layer: Partial least square regression model (MIT). This model is available in the literature	Erk/Akt ratio	Cell kill rate with chemotherapeutic alone and in combination of chemotherapeutic with targeted drug	The integration layer accepts input from Layer 3 and outputs Cell Kill Rate for each mutant examined in molecular model	(q)
q. Sequential Application of Anticancer Drugs Enhances Cell Death by Rewiring Apoptotic Signaling Networks, M. J. Lee1, A. S. Ye, A. K. Gardino, A. M. Heijink, P. K. Sorger, G. MacBeath, M. B. Yaffe, <u>Cell</u> 149(4), 780–794, 2012				

M7. Detailed Description and Implementation of the Subcellular Components:

Level 1 or Structural Atomistic Level: Deregulation and mutation of receptor tyrosine kinases (RTKs) have been correlated with cancer almost immediately after their discovery and purification in the early 1980s. We developed a simulation approach to delineate molecular-level mechanisms of activation of protein receptor tyrosine kinases and describe clinical implications of mutations in the Anaplastic Lymphoma Kinase (ALK) receptor tyrosine kinase in pediatric neuroblastoma and the epidermal growth factor receptor (EGFR) mutations in non-small-cell lung cancer. Our approach sheds molecular-level insight into the various mechanisms governing such transforming mutations at the level of kinase activity and are remarkably predictive of experimental observations. We expect that the current study on ALK and EGFR with suitable validation will transform our computational approach to enable future predictions of driver oncogenic mutations with low false-positive rates, and can hence serve an important in silico tool toward personalized cancer therapy.

Computational methodologies offer a powerful, quantitative, and complimentary alternative for the study of intracellular kinase domains, which if utilized correctly can predict effects of mutations on RTK activation mechanisms. With the focus on the discovery and exploitation of oncogenic driver mutations, current approaches typically involve collaborative partnership between cancer geneticists, structural, computational and cellular biologists, drug development experts, and clinical trials experts. The different facets of research activities include:

- (1) Genomics- access to thousands of patient genotypic samples;
- (2) Patients- large developmental therapeutics team with referrals from multiple nations;
- (3) Samples- investment in the collection of patient samples including thousands of tumor, DNA, RNA and protein samples, all with rich clinical annotation and outcomes data. This includes a rich bank of dozens of human and murine derived cancer cell lines;
- (4) Clinical trials infrastructure;
- (5) Structural Biology- structure elucidation of proteins and computational elucidations of enzymatic mechanisms and studies of signal transduction.

We focused on the delineation of activation mechanisms using computational techniques and the central problem of oncogenic mutations in RTKs as key mediators of human cancer. Development of computational tools necessary to understand the structural consequences of genetic mutations in cancer will facilitate our quest for molecular-level insight into rational mechanisms for drug development and for combating drug resistance. Current outlook on the receptor tyrosine kinase ALK especially provides an important illustration of how this approach can revolutionize cancer treatment. Namely, oncogenic driver mutations were identified in several cancer patients, and shown to cause activation of the receptor – immediately indicating the use of existing kinase inhibitors in this patient population. Individual ALK-activating mutations show different inhibitor sensitivities, creating an urgent need to understand the structural basis for their effects in order to guide treatment choice. Emergence of resistance mutations, as also seen with kinase-targeted inhibitors of ABL (in Chronic Myelogenous Leukemia) and EGFR (in Non-Small-Cell Lung Cancer) creates a need to understand their spectrum and the origin of their effects through our integrated approach.

METHODS: Molecular dynamics simulations followed by hydrogen bond and solvent accessible surface area analyses were carried out on structures of wildtype and mutant kinase proteins. Hydrogen bond (H-bond) analysis was performed on the last 1000 frames (20 ns) of trajectory. The

occupancies (Y) for each residue-to-residue hydrogen bond range from 0% to 100% across the last 20 ns of trajectory in each system. A scoring function was created to analyze how active-like the hydrogen bond networks were for each system. The scoring process is outlined below.

(1) For each hydrogen bond, calculate the difference in occupancies between the active (A) wildtype (WT) and inactive (I) WT systems ($\Delta_{WT} = Y_{IWT} - Y_{AWT}$).

(2) For each bond, if $|\Delta_{WT}| > 40.0\%$, calculate the difference in occupancies between the active WT and inactive mutant (MUT) for each mutation ($\Delta_{MUT} = Y_{IWT} - Y_{AMUT}$).

(3) If $\Delta_{MUT}/\Delta_{WT} > 0.5$, then the bond receives a binary activation score of 1; otherwise, it receives a score of 0. The scores were tallied separately for the activation loop (A-loop) and the C-helix. Any bonds bridging the two were counted in both analyses. For the A-loop (comprising 15 H-bonds), a collective score of 9 or greater was considered to be activating the kinase. For the C-helix (comprising 7 H-bonds), a collective score of 4 or greater was considered activating. Solvent accessible surface area (SASA) values were calculated using a probe radius of 1.4 Å. The SASA was calculated on a per-residue basis for the residues forming the hydrophobic core. The SASA values (in units of Å²) were averaged over all steps of the MD trajectory, from which the mean SASA values were computed. Mutant systems were scored as activating as follows:

(1) SASA values were normalized using the expression $SASA(MUT,I) - SASA(WT,I) / SASA(WT,A) - SASA(WT,I)$;

(2) If the normalized SASA scores were less than -2.5 for at least two residues or more, the mutant system was scored as activating (with a score of 1);

(3) If the sum of the SASA scores of residues that showed a large difference between the active and inactive states in the WT were negative, the mutant was scored as activating;

(4) If the sum in (3) was positive but less than 1.0, but at least one of the residues had a score of <-4.0, the mutant was scored as activating.

Activation mechanism based on destabilizing the C-helix interactions in the inactive conformation: in recent computational work on kinase domains of ErbB receptors, we suggested that inactive and active conformations have distinct signatures of the hydrogen bond networks, particularly involving the residues of the C-Helix. A similar analysis was performed on various mutant systems of the ALK kinase domain, focusing on the C-Helix. A score in this category represents hydrogen-bonding patterns of C-helix residues showing the characteristics of the active-wild type conformation. The mutations were scored p (proximal) if the site of the mutation was part of the C-Helix or proximal (<6 Å) to the C-Helix residues; the choice of 6 Å represents proximity in terms of 1-2 amino acid residues. The mutations in this category are, not surprisingly, mostly clustered proximal to the C-Helix, A-loop, and the active site. However a small number of mutations in the C-lobe and the hydrophobic core are also featured in this category. A similar protocol was followed for activation based on A-loop interactions.

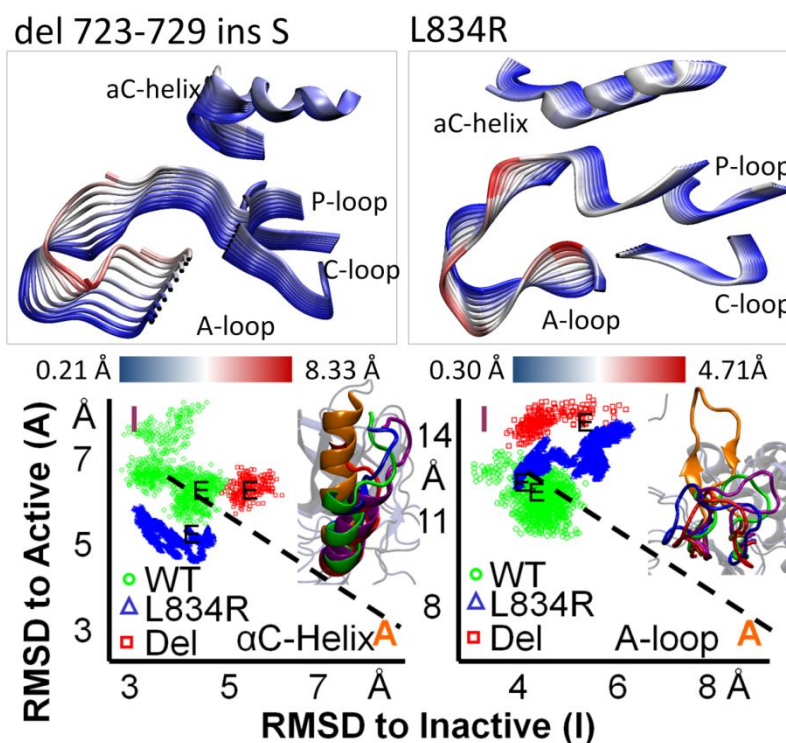


Fig. M2 Prediction of activation status of commonly observed mutations of EGFR using molecular modelling and dynamics. (Top) Principal components showing essential motion in protein domains; (Bottom) MD trajectories showing time-evolution of the conformation towards active and inactive conformations.

Predictions based on hydrophobic interactions: In our earlier computational work on ErbB kinase systems, we introduced a method to score hydrophobic interactions based on SASA analysis. A similar analysis on ALK mutant systems was carried out. There is a significant difference between the SASA of the residues of the hydrophobic core in the active and inactive conformations. The sum total of the SASA for these residues is significantly higher in the inactive conformation relative to active.

Results: We hypothesized that classifying mutations based on similarity in activation scores across different categories will reveal conserved mechanisms of kinase activation and regulation. Maris et al. have identified >25 mutations to the ALK-tyrosine kinase domain (TKD) in their neuroblastoma patients. Some of the mutants were known to be activating, while the role and significance of others were unclear. Our scoring function relies on the hypothesis that active and inactive states are differentially stabilized by molecular (hydrophilic and hydrophobic) interactions and that activating mutations alter the relative occupancy of these states by destabilizing the inactive or stabilizing the active state. Lemmon and co-workers have shown that the two most common mutants, R1275Q and F1174L, display increased tyrosine kinase activity compared to wild type controls both in vivo and in vitro. It remains unclear, however, exactly how these mutations functionally cause the kinase to be constitutively active.

Based on the MD simulations of each of the mutant systems in the inactive conformation, and the wildtype system in both active and inactive conformations (Fig.M2), we assigned activation scores for

the different mutants based on hydrogen bond analysis of activation loop and C-helix residues, based on global motion, and based on hydrophobic analysis; these scores enabled us to classify the different mutant systems “activating” or “inactivating”. Overall, in a double-blind comparison to experimental results of kinase activation, our computational results are remarkably accurate (>85%) in predicting the effect of mutations on the functional status of kinase activation (based on catalytic rate or *k_{cat}* values). We expect that the current study on ALK with suitable validation will transform our computational approach to enable future predictions of driver oncogenic mutations with low false-positive rates, and can hence serve an important *in silico* tool toward personalized cancer therapy.

Level 2 or Molecular Association Layer: Here, a method to predict the activation status of kinase domain mutations in cancer is developed. This method, which makes use of the machine learning technique support vector machines (SVM), has applications to cancer treatment, as well as numerous other diseases that involve kinase misregulation.

Sequencing efforts as well as the frequent failure of targeted therapies has lead to an increasingly well-recognized principle that not all mutations confer selective advantage on cancer cells. These mutations are known as passenger mutations while mutations that confer some advantage are commonly referred to as driver mutations, because they can be seen as driving cancer progression. The growing understanding of the importance of mutations on cancer progression is reflected in the rapid increase in available sequencing data via repositories such as The Catalog of Somatic Mutations in Cancer (COSMIC) and The Cancer Genome Atlas (TCGA). Coterminal with this increase in data has been an increase in efforts to computationally assess the effects of these mutations. These methods generally seek to use machine learning on large datasets of variants that are known to be (or not to be) deleterious. Features that are common among one class of known variants or the other are then used to predict what will be the effect of new variants.

The most popular technique used to classify mutations that are specific to cancer is a method from machine learning known as support vector machines (SVM). This essentially geometric method seeks to find combinations of features that are common to mutations of different classes so that mutations of unknown class (i.e. driver or passenger) can be classified. SVM has been used to develop classifiers that predict whether mutations across the whole genome as well as in a specific class of proteins, kinases. These methods report that they make accurate predictions, based on cross-validation, and that they have a high receiver operating characteristic area under the curve (AUC), or the probability of distinguishing between examples of different classes. However, they both suffer from a problem that is seemingly common in the literature whereby they make *a priori* decisions about which mutations belong in which class, instead of letting the data lead the way. This should make the results of these and any similarly constructed classifiers suspect.

Implementation: Our dataset was constructed via mining of uniprot and the literature for mutations in a subset of human kinases consisting of 468 kinase domain containing proteins. SVM Construction: the kinase dataset was converted into a feature vector using an in house perl script. The elements of the feature vector include: the wild type and mutant residue identity, the wild type and mutant residue chemistry (i.e. aliphatic, acidic, basic, polar, aromatic), change in Kyte-Doolittle hydrophathy from wild type to mutant as well as change of mutant from average Kyte-Doolittle hydrophathy at that position, similarly for free energy of solvation, change in van der Waals radius, change in charge, and change in polarity. Also included are the SIFT score, whether the mutation occurs in a functionally important region in the kinase domain such as the α C helix, the nucleotide binding loop, the activation loop, or the catalytic loop. Finally, the proportion of a specific mutant occurring at a

specific location relative to the total number of mutants in the whole kinase domain of the protein that a mutation occurs in was also included as a measure of oncogenicity. The performance of the algorithm prediction was evaluated via cross-validation. The datasets used for cross-validation were always balanced. Cross-validation was performed by taking 75% of the balanced dataset and using it for model training while using the remaining 25% of the data for testing.

Results: The method was seen to be fairly accurate and precise, though sensitivity is somewhat lacking. The area under the curve (AUC) was also very optimal. In comparison to MD based method, the SVM does quite well in terms of accuracy of prediction. The SVM method is shown to be fairly reliable at predicting the effect of kinase domain mutations, especially when a balanced dataset is used. It is also faster than recent efforts to use MD to predict the effect of kinase domain mutations, and does not make any a priori decisions about which mutations are driver mutations, as many recent machine learning efforts have.

Level 3 or the Molecular Network Layer translates the molecular mechanisms gleaned from levels 1 and 2 to infer clinical implications of oncogenic mutations through a multiscale network model of receptor signalling. For cellular homeostasis, pro-survival signals are balanced by pro-apoptotic signals, with both being triggered and balanced by a variety of interacting intracellular pathways.

Using a cellular model of mass-action reactions, we consider signaling through receptors by combining three canonical models and augmented by our own set of reactions: phosphorylation and docking reactions are modeled according to molecular dynamics predictions; the MAPK, PI3K/Akt, and JAK-Stat pathways are incorporated into the model through curated SBML models. We also resolve phosphorylation of the active receptors at tyrosine sites which, when phosphorylated, are binding sites for adaptors. Mutant specific kinase activation, dimer formation, ATP and inhibitor binding, and trafficking allow us to tune the network for each mutant system. We hypothesized that the resulting systems model of receptor signalling encodes mechanisms of inhibitor sensitivity and resistance in a context dependent fashion for the different mutant systems (see Fig. M3).

Results: Previous experimental studies have demonstrated that ErbB3/HER3 is a key mediator of resistance to various tyrosine kinase inhibitors (TKIs) currently in use. Some postulated mechanisms include leaky ErbB2-catalyzed phosphorylation of ErbB3, e.g., incomplete inhibition of ErbB2 catalytic activity by the TKI. Indeed, previous experimental studies have demonstrated that leaky ErbB2 phosphorylation of ErbB3 in TKI-bound ErbB2/3 heterodimers is amplified by additional resistance mechanisms, such as inhibition of cellular phosphatases by TKI-mediated production of reactive oxygen species (ROS), and increased expression of ErbB3 at the plasma membrane. However, we had recently shown the assumed inactive ErbB3 pseudokinase is, in fact, a weakly active kinase with ~1000 fold weaker phosphorylation than the canonical kinase members of the ErbB family. Therefore, though the ErbB2 kinase is a viable route of resistance, here we consider ErbB3 catalytic activity in the ErbB signaling network as a potential TKI resistance mechanism. To translate our observations of the weak, yet robust, activity of the ErbB3 kinase into a physiologically relevant context and investigate the implications of ErbB3 activation for ErbB signaling dynamics, we constructed a systems-level model for ErbB3 within the framework of the systems model described above. We modelled the stimulation of the ErbB signaling network through NRG-1 β , which signals through the ErbB2/ErbB3/ErbB4 kinases (though ErbB4 kinase is omitted from the model since ErbB4 signaling is weak or absent in many cancer cell lines). A parameter sensitivity analysis was performed, which identified the key proteins that direct signaling in our model of the ErbB network with respect to AKT activation via stimulation of NRG-1 β . ErbB3 and NRG-1 β represent the most sensitive species in the signaling network, followed by ErbB2 concentration. EGFR is not a strong determinant of the

extent of AKT phosphorylation, as expected from the weak ability of NRG-1 β to elicit EGFR dimers. PTEN (the PIP3 phosphatase) and the ErbB phosphatase exhibited a negative sensitivity in the analysis, as these phosphatases negatively regulate the signalling network through dephosphorylation of key molecular species. Upon incorporation of the TKI lapatinib, which inhibits EGFR and ErbB2 catalytic activity, into our model of ErbB3, the ErbB signaling network relies more heavily upon ErbB3 activity for AKT induction. With completely inhibited EGFR and ErbB2 signaling via introduction of lapatinib into the model, ErbB3 and AKT signals still persist at maximal inhibition by lapatinib. The results of pAKT sensitivity analysis of the lapatinib-treated model to those of the inhibitor-free model show that sensitivity to ErbB3 and NRG-1 β increases, whereas sensitivity to EGFR and ErbB2 decreases, as lapatinib sequesters EGFR and ErbB2 molecules. The negative normalized sensitivity to the ErbB phosphatase also increases, as the pool of ErbB dimers has diminished due to sequestration of EGFR and ErbB2 by lapatinib. Thus a single alteration to the signaling model (in this case, addition of lapatinib) significantly redefines the most perturbation-sensitive nodes in the network. Although the pAKT signal induced by ErbB3 phosphorylation in our *in silico* lapatinib-treated cell is relatively weak, in an actual physiological context, a tumor cell may employ several resistance mechanisms at once. One of the sensitive nodes of NRG-1 β -driven ErbB signaling is ErbB phosphatase levels, and simulations showed decreased activity of phosphatases resulted in an amplification of the level of AKT signaling induced by ErbB3. It has been demonstrated that in certain cases of TKI resistance, the tumor cell responds to the reduction in pAKT levels by upregulating vesicular transport of ErbB3 from the cytoplasm to the plasma membrane.

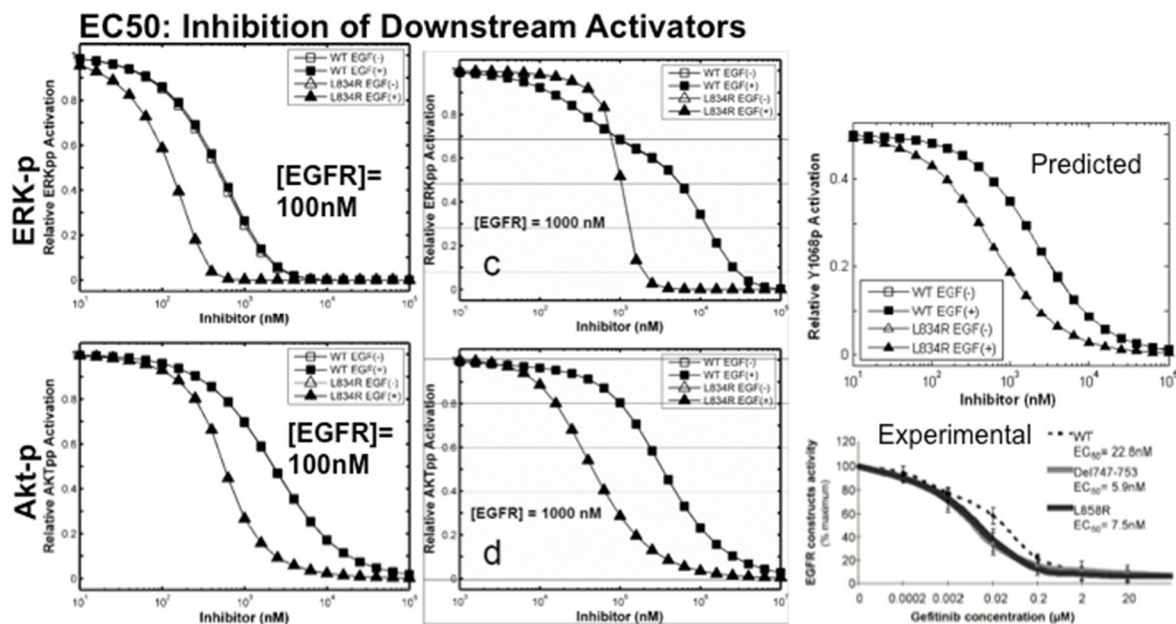


Fig. M3 Area under the curve inhibition characteristics: (left) MAPK and AKT inhibition at low EGFR expression; (middle) MAPK and AKT inhibition at high EGFR expression; (right) comparison between calculated and experimental measures of EGFR activation.

Our data parallels the experimental studies performed by Sergina and colleagues, which describe ErbB3-mediated resistance and pAKT signaling in various TKI-treated tumor cell lines as well as *in vivo*. Thus our model demonstrates that even a weak level of ErbB3 signalling, as suggested by our

previous results could be physiologically relevant in the context of an ErbB-driven tumor cell, and illustrates several routes through which ErbB3 signalling may be compounded by other previously postulated resistance mechanisms to generate TKI resistance. A similar study was conducted by us recently to delineate the effect of inactivating mutations of ErbB4/HER4 on cell proliferation.

M8. Conclusion

Understanding the activation mechanisms of the kinase mutants is important considering the crucial cell signaling pathways they control. Mutations of kinases have been revealed in mutational screens of multiple cancers. The regulation of the ErbB kinases is maintained through a flexible multiple-point network with multiple redundancies to ensure signal propagation. Here formulated a hierarchical multiscale model of kinases to investigate their activation mechanisms and the subsequent effects of kinase perturbation on their cell signalling network. The multiscale model we present is useful in examining atomic level protein characteristics and carrying them over into differential activity of cell signaling networks. The results we show have a striking correlation with highlighting perturbation sensitive regions with the regions mutated in clinically identified oncogenic kinase mutations: the hydrophobic core in the EGFR and ErbB4 as well as the α C- β 4 region in ErbB2. We have similar correlation with observed EGFR kinase mutations (L834R and del 723-729 ins S) affecting cell signaling pathways so that inhibition of the mutant kinase is a viable therapeutic strategy as well as the observed mechanisms of resistance to EGFR kinase inhibition. Furthermore, by examining the “inactive” pseudokinase ErbB3 and characterizing its weak activity, we justify an alternate means of resistance to ErbB TKI inhibition and propose that targeting of ErbB3 may represent a superior therapeutic strategy for certain ErbB-driven cancers. Therefore, multiscale modeling is a tool that can not only link kinase domain fluctuations with signaling effects to help contextualize mutations found in oncogenic cell lines, but also refine therapeutic strategies to target key perturbation sensitive regions of kinase signaling, at the molecular level as well as the cellular level. This framework was subjected to a double-blind test in the case of mutations in ALK where the model predictions were accurate >85% of the time in comparison to experiments. In order to translate these findings into the framework of the multi modeller framework within CHIC, we will utilize the partial least squares regression model that exists in the literature which relates ERK/AKT activation ratios to cell kill rate, as discussed briefly in the integration layer in Table M-1.

M9. Description of the Subcellular (Atomistic and Molecular) Component Models (M) through the 13 Perspectives

TABLE "M-13P" (FIRST PART)		
PERSPECTIVE CODE NUMBER	PERSPECTIVE TITLE	PERSPECTIVE VALUE(S)
I	TUMOUR-AFFECTED NORMAL TISSUE MODELLING	tumour
II	SPATIAL SCALE(S) OF THE MANIFESTATION OF LIFE	atomic molecular cellular
III	TEMPORAL SCALE(S) OF THE MANIFESTATION OF LIFE	nsec msec sec min h
IV	BIOMECHANISM(S) ADDRESSED	gene mutations protein mutations protein-protein interactions drug-protein interactions structural atomistic interactions molecular association interactions molecular network interactions molecular pathway interactions
V	TUMOUR TYPE(S) ADDRESSED	lung cancer other solid tumours
VI	TREATMENT MODALITY(-IES) ADDRESSED	chemotherapy radiotherapy targeted therapy

TABLE "M-13P" (SECOND PART)		
PERSPECTIVE CODE NUMBER	PERSPECTIVE TITLE	PERSPECTIVE VALUE(S)
VII	GENERIC CANCER BIOLOGY – CLINICALLY DRIVEN CHARACTER OF THE MODELLING APPROACH	generic cancer biology clinically driven
VIII	ORDER OF ADDRESSING DIFFERENT SPATIAL SCALES	Bottom-up
IX	ORDER OF ADDRESSING DIFFERENT TEMPORAL SCALES	short periods → longer periods,
X	MECHANISTIC-STATISTICAL CHARACTER OF THE MODELLING APPROACH	mechanistic statistical
XI	DETERMINISTIC-STOCHASTIC CHARACTER OF THE MODELLING APPROACH	deterministic stochastic
XII	CONTINUOUS-FINITE-DISCRETE CHARACTER OF THE MATHEMATICS INVOLVED	continuous finite (finitized continuous) discrete
XIII	CLOSED FORM SOLUTION – ALGORITHMIC SIMULATION MODELLING APPROACH	algorithmic simulation

N. Potential Addition of a Separate Metabolic Network

N1. A Brief Outline of the Potential Component Model

An extra future refinement at the molecular level (not foreseen in the Description of Work) will be a hypo-hypomodel focusing on metabolism. This is under development by FORTH. Since metabolism has already been taken into account at the cellular and supercellular levels/scales by the pure tumour growth and response to treatment component module (T), the present component model is not considered a fundamental part of the hypomodel under development but rather an extra, demonstration geared possible refinement. Therefore, only a very brief outline of the hypomodel under development is provided here.

This sub-cellular hypomodel describes the aberrant metabolism of cancer cells at the genome scale incorporating gene expression data into well-developed constrained-based methods such as the Flux Balance Analysis method [N1-N3].

Fig. N1 indicates the topological positioning of this extra hypomodel (grey broken line box) within the extended master topology of the lung cancer demonstrator. Table N-I provides a brief outline of the extra metabolic hypomodel in a tabular form.

The hypomodel has to be tested for its validity, which include

- i) its ability to capture the metabolic capabilities of glycolytic cells that are experimentally observed in lung cancer,
- ii) its sensitivity to the flux constraints imposed to the metabolic pathways, and
- iii) whether the predicted proliferation, uptake and secretion rates lie within the range of observed values.

The hypomodel is to be linked to the angiogenic neovasculature hypomodel and subsequently with the pure tumour growth model.

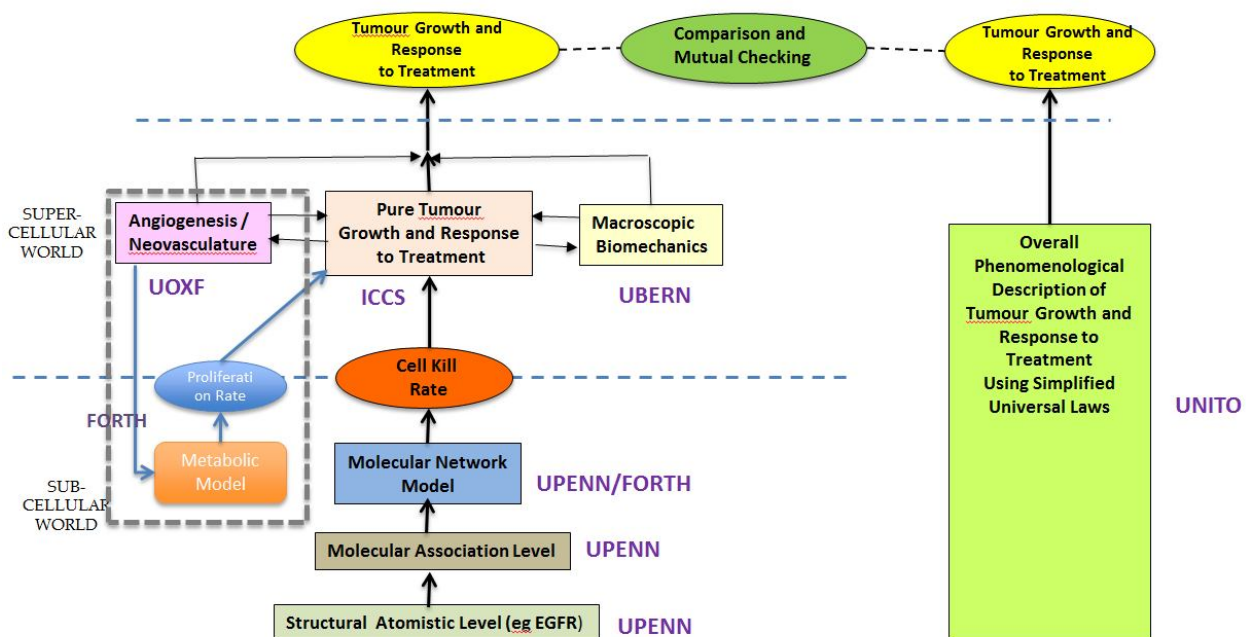


Fig. N1. Extended master topology of the lung cancer demonstrator including the extra metabolic component at the molecular level

TABLE N-I A BRIEF OUTLINE OF THE EXTRA METABOLIC HYPOMODEL

MODEL NUMBER	MODEL TITLE	BRIEF MODEL DESCRIPTION	MODEL INPUT PARAMETERS (SYMBOLS)	FULL NAME OF EACH MODEL INPUT PARAMETER	INPUT PARAMETER UNIT	MODEL OUTPUT PARAMETERS (SYMBOLS)	FULL NAME OF EACH MODEL OUTPUT PARAMETER	OUTPUT PARAMETER UNIT	CORE MATHEMATICAL METHODS UTILIZED	REFERENCES
3.	Sub-cellular level metabolic hypomodel	A sub-cellular hypomodel that describes the aberrant metabolism of cancer cells at genome scale incorporating gene expression data into well-developed constrained-based methods such as the Flux Balance Analysis method [N1, N3]. A genome-scale human metabolic network reconstruction [N2] is used in order to account for the interconnectivity of the metabolic reactions.	glc_uptake_Bound gln_uptake_Bound o2_uptake_Bound generxn_Lbound generxn_Ubound	glucose uptake bound glutamine uptake bound oxygen uptake bound Lowest reaction rate Highest reaction rate	umol/mgDW/h umol/mgDW/h umol/mgDW/h umol/mgDW/h umol/mgDW/h	growth_rate glc_uptake gln_uptake o2_uptake lac_intake	growth rate glucose uptake rate glutamine uptake rate oxygen uptake rate lactate secretion rate	1/h umol/mgDW/h umol/mgDW/h umol/mgDW/h umol/mgDW/h	A linear programming problem solved using the COBRA toolbox [N4,N5].	[N1-N5]



N2. References

[N1] T. Shlomi et al, "Genome-scale metabolic modeling elucidates the role of proliferative adaptation in causing the Warburg effect," PLoS Comput. Biol., vol. 7, no. 3, p. e1002018, Mar. 2011

[N2] N. C. Duarte, S. A. Becker, N. Jamshidi, I. Thiele, M. L. Mo, T. D. Vo, R. Srivas, and B. O. Palsson, "Global reconstruction of the human metabolic network based on genomic and bibliomic data," Proc Natl Acad Sci U S A, vol. 104, pp. 1777-82, Feb 6 2007.

[N3] E. Tzamali V. Sakkalis, and K. Marias, "The effects of near optimal growth solutions in genome-scale human cancer metabolic model," in Proc. IEEE BIBE 2013, Larnaca, Cyprus, 2012, pp. 626-631.

[N4] S. A. Becker, A. M. Feist, M. L. Mo, G. Hannum, B. O. Palsson, and M. J. Herrgard, "Quantitative prediction of cellular metabolism with constraint-based models: the COBRA Toolbox," Nat Protoc, vol. 2, pp. 727-38, 2007.

[N5] <http://www.gnu.org/software/glpk/glpk.html>, "GNU Linear Programming Kit."



N3. Description of the Potential Addition of a Metabolic Network (N) through the 13 Perspectives

TABLE "N-13P" (FIRST PART)		
PERSPECTIVE CODE NUMBER	PERSPECTIVE TITLE	PERSPECTIVE VALUE(S)
I	TUMOUR-AFFECTED NORMAL TISSUE MODELLING	tumour
II	SPATIAL SCALE(S) OF THE MANIFESTATION OF LIFE	molecular cellular tissue
III	TEMPORAL SCALE(S) OF THE MANIFESTATION OF LIFE	sec min h d
IV	BIOMECHANISM(S) ADDRESSED	metabolism molecular network interactions molecular pathway interactions
V	TUMOUR TYPE(S) ADDRESSED	lung cancer other solid tumours
VI	TREATMENT MODALITY(-IES) ADDRESSED	no treatment consideration

TABLE "N-13P" (SECOND PART)		
PERSPECTIVE CODE NUMBER	PERSPECTIVE TITLE	PERSPECTIVE VALUE(S)
VII	GENERIC CANCER BIOLOGY – CLINICALLY DRIVEN CHARACTER OF THE MODELLING APPROACH	generic cancer biology clinically driven
VIII	ORDER OF ADDRESSING DIFFERENT SPATIAL SCALES	Bottom-up
IX	ORDER OF ADDRESSING DIFFERENT TEMPORAL SCALES	short periods → longer periods
X	MECHANISTIC-STATISTICAL CHARACTER OF THE MODELLING APPROACH	mechanistic statistical
XI	DETERMINISTIC-STOCHASTIC CHARACTER OF THE MODELLING APPROACH	deterministic stochastic
XII	CONTINUOUS-FINITE-DISCRETE CHARACTER OF THE MATHEMATICS INVOLVED	continuous finite (finitized continuous) discrete
XIII	CLOSED FORM SOLUTION – ALGORITHMIC SIMULATION MODELLING APPROACH	algorithmic simulation

U. Gross Component Models Based on Simplified Universal Growth Laws

U1. Model Description

The general hyper-model recall a different hypo-model in response to different request of the user. Hypo-model available are:

- pure tumour growth model
- growth and mutation model
- growth and treatment model
- growth, mutation and treatment model

The mathematical basis of these hypo-models is a couple of ODEs (Ordinary Differential Equation) following the gompertzian growth law (in progress: hypo-models which use West growth law) which stand for two tumour cell populations, present in the cancer mass, with different behaviours (e.g. hypoxic and oxic cells).

The stage of the tumour and the choice of the therapy define the parameters of growth, mutation and death rate; the variability between different patients with same parameters is given by a different probability to internalize the drug.

The model returns the tumour volume during the simulated period, both as csv file and as graph.

U2. Model Input

- Stage of the tumour
- Mutation (numeric data):
 - 0 for no mutation
 - 1 for low mutation
 - 2 for high mutation
 - 3 for random mutation
- Therapies:
 - Number of treatments
 - kill rates of each treatment/drug
- Information about therapy's times
- CSV file with:
 - Numeric code of the patient
 - Time
 - Initial volume (and optionally others to compare simulated with real data)
 - 0 no treatment, 1 one treatment, 2 treatments

Example of the .csv file:

Patient number	Time	Volume	Treatment	Notes
1	0	100300	0	Initial tumor volume
1	5		1	After 5 days 1 drug is administered
1	10		2	After 10 days 2 drugs are administered
1	15		1	After 15 days 1 drug is administered
1	20	45000	0	Final volume after 20 days of therapy
2	0	100094	0	Initial tumor volume
2	5		1	After 5 days 1 drug is administered

U3. Model Output

- Evolution of the tumour volume during the time

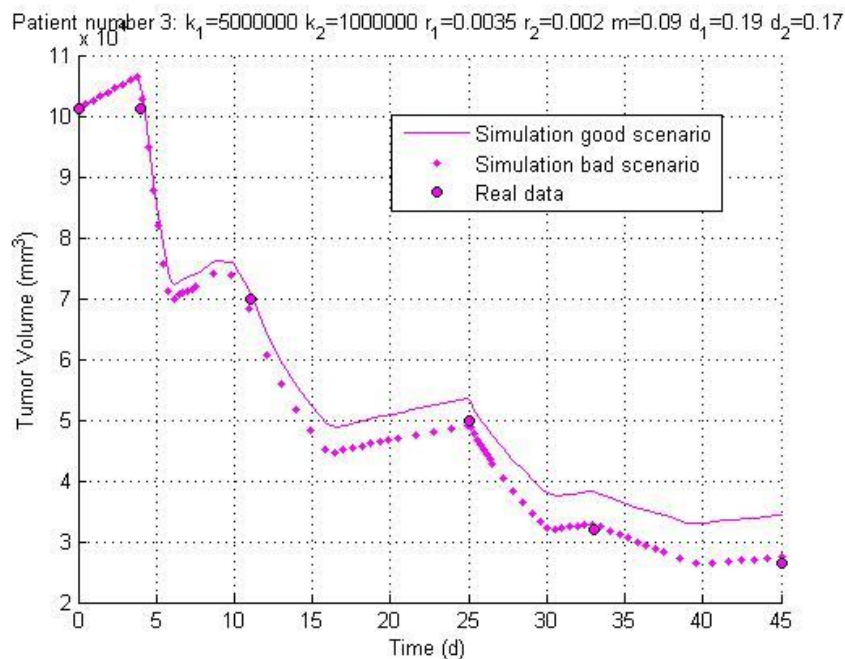


Fig.U1 graphical output of the hypermodel. Two simulations and real data of tumour volume in relation with time (days) are plotted in the same graph. In the top of the figure the used parameters are shown: carrying capacities (k), growth rates (r) and mutation rate (m) of the two cell populations and kill rates (d) of the two drugs

U4. Sensitivity Analysis

The ODE system of the hypo-models is:

$$\begin{aligned}\frac{dN_1(t)}{dt} &= -r_1 N_1 \log\left(\frac{N_1}{N_{\infty,1}}\right) - m N_1 - d_1 N_1 \\ \frac{dN_2(t)}{dt} &= -r_2 N_2 \log\left(\frac{N_2}{N_{\infty,2}}\right) + m N_1 - d_2 N_2\end{aligned}$$

where N_1 and N_2 are the two cell populations, N_{inf} is the carrying capacity, r is the growth rate, m the mutation rate and d the kill rate of the treatment.

The unique stable point ($N_{\text{inf}1}^*, N_{\text{inf}2}^*$) is independent to the initial point but is strictly dependent to the other parameters (see table below).

Parameters	Mutation case only	Treatment case only	Mutation with treatment case
$N_{\infty,1}^*$	$N_{\infty,1} e^{\frac{-m}{r_1}}$	$N_{\infty,1} e^{\frac{-d_1}{r_1}}$	$N_{\infty,1} e^{\frac{-(m+d_1)}{r_1}}$
$N_{\infty,2}^*$	$N_{\infty,2} e^{\frac{c+m}{r_2} \frac{N_1^*}{N_2^*}}$	$N_{\infty,2} e^{\frac{d_2-c}{r_2}}$	$N_{\infty,2} e^{\frac{d_2-c-m}{r_2} \frac{N_1^*}{N_2^*}}$

Changing the parameters, we observed a coherent behaviour with real cell populations; as shown in next graphs:

- if there is not mutation the two populations grow independently, otherwise, if mutation rate is very high, mutant population tends to disappear
- if the treatment is ineffective the populations grow normally, otherwise if the treatment is very effective the sensitive population tends to decrease drastically

U4.1 Only Tumour Growth

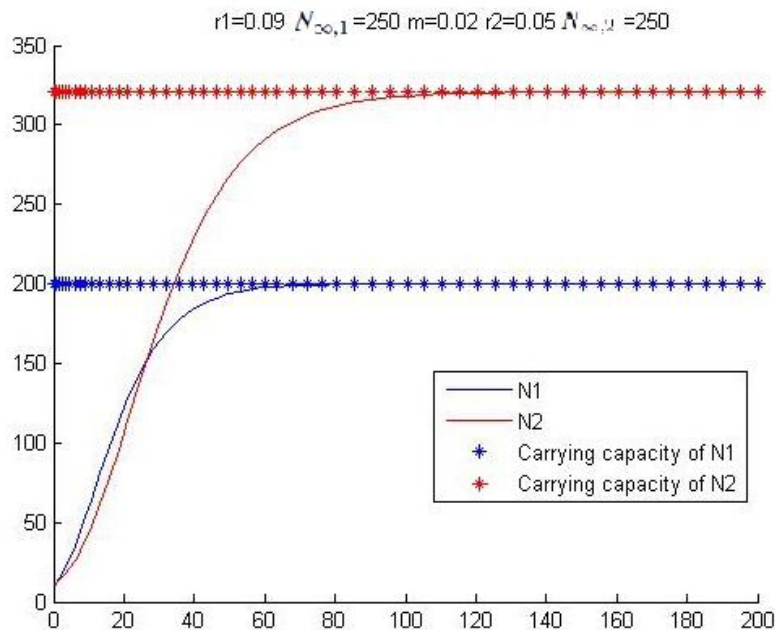


Fig.U2 graphical output of the hypomodel. The two curves are the volume of tumour cell population in relation with time (months) are plotted in the same graph. In the top of the figure the used parameters are shown: carrying capacities (N_{inf}), growth rates (r) and mutation rate (m) of the two cell populations

U4.2 Growth and Mutation

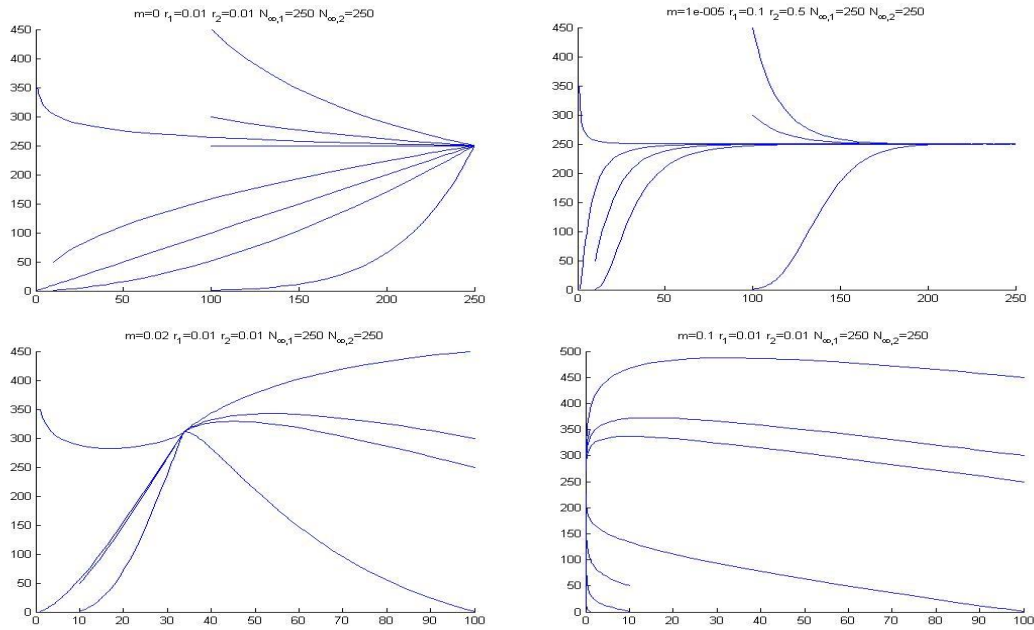


Fig.U3 Phase space graphs. In these figures we show the behaviours of the two populations (N_1 in the abscissa, N_2 in the ordinate) using different initial conditions. In the top of the figure the used parameters are shown: carrying capacities (N_{inf}), growth rates (r) and mutation rate (m) of the two cell population

U4.3 Growth and Treatment

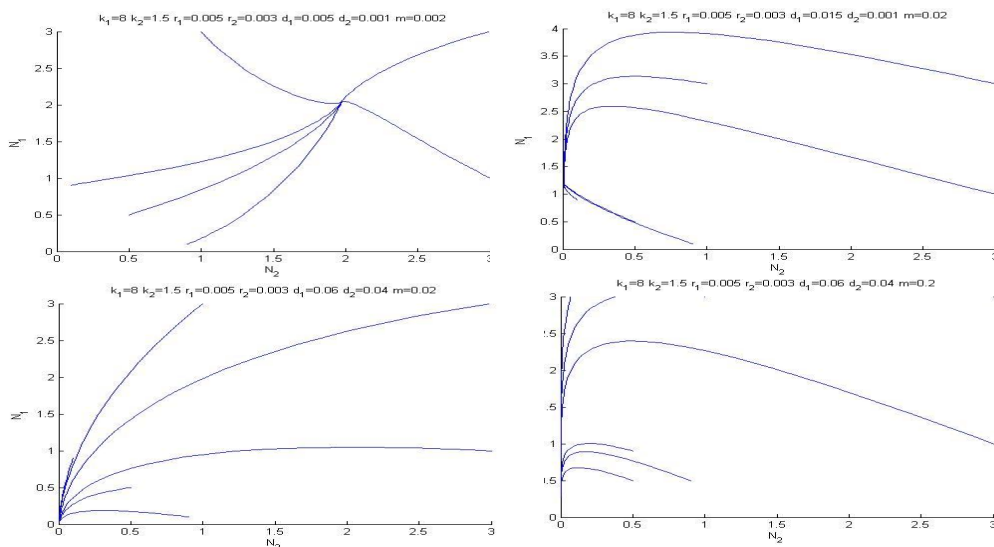


Fig. U4. Phase space graphs. In these figures we show the behaviours of the two populations (N_1 in the ordinate, N_2 in the abscissa) using different initial conditions. In the top of the figure the used parameters are shown: carrying capacities(k) and growth rates of the two cell populations and kill rates (d) of the two drugs

U4.4 Growth, Mutation and Treatment

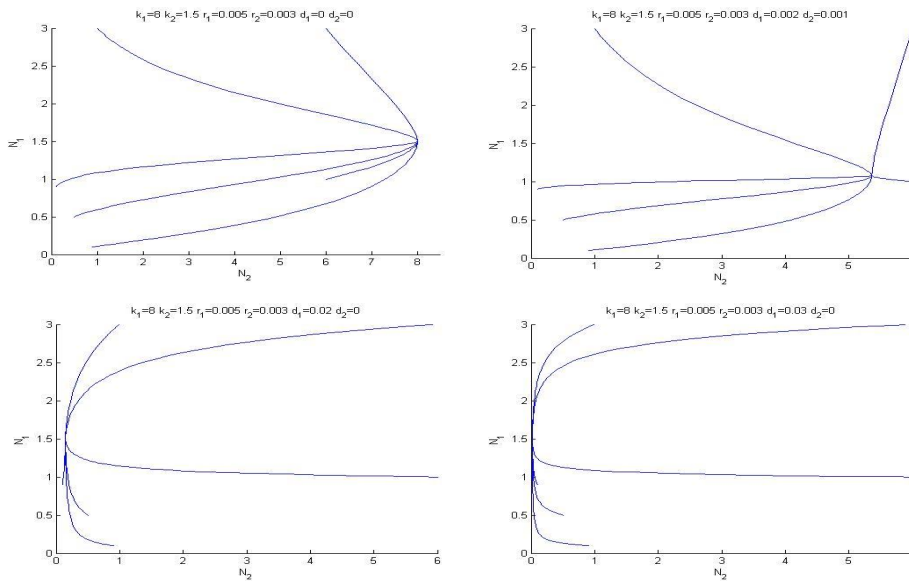


Fig.U5 Phase space graphs. In these figures we show the behaviours of the two populations (N_1 in the ordinate, N_2 in the abscissa) using different initial conditions. In the top of the figure the used parameters are shown: carrying capacities(k),growth rates (r) and mutation rate (m) of the two cell populations and kill rates (d) of the two drugs

We also investigated the relationships between the parameters. First, we fixed the growth rate and we varied the mutation rate (kill rate was supposed equal to zero): in agreement with the analytical results, we found that the mutant population tends to lapse if the mutation rate is about ten times bigger than the growth rate. Secondly, we set to zero the mutation rate and we varied kill rate: in this case also we found that the population tends to die if the kill rate is about ten times bigger than the growth rate. Finally, we varied both mutation and kill rate and we interestingly found that the population benefited from the mutation could lapse both in case of a high and a low mutation, so the kill rate term is 'stronger' than mutation ones.

U4.5 Varying the Mutation Rate

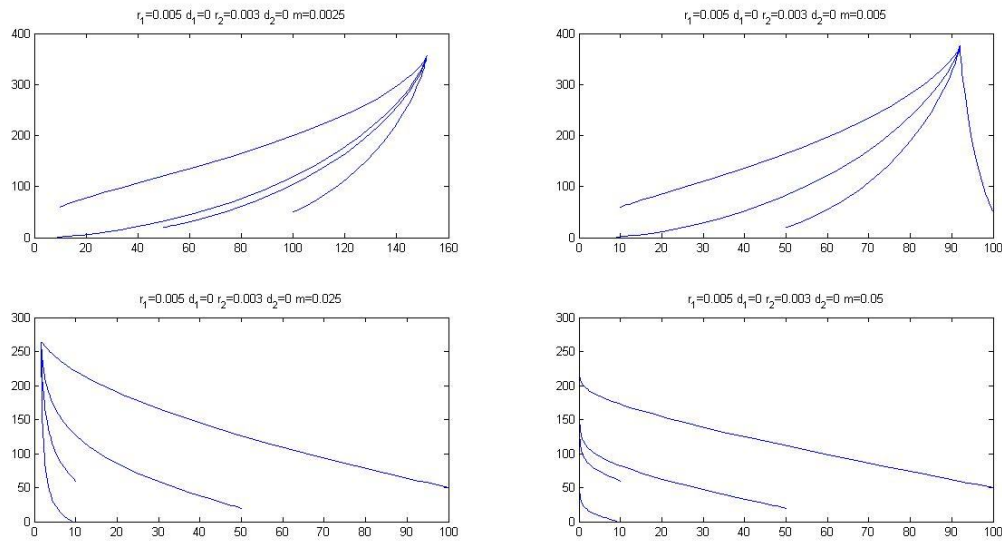


Fig.U6 Phase space graphs with different mutation rates. In these figures we show the behaviours of the two populations (N_1 in the ordinate, N_2 in the abscissa) using different initial conditions. In the top of the figure the used parameters are shown: mutation rate (m) of the two cell populations and kill rates (d) of the two drugs

U4.6 Varying the Kill Rate

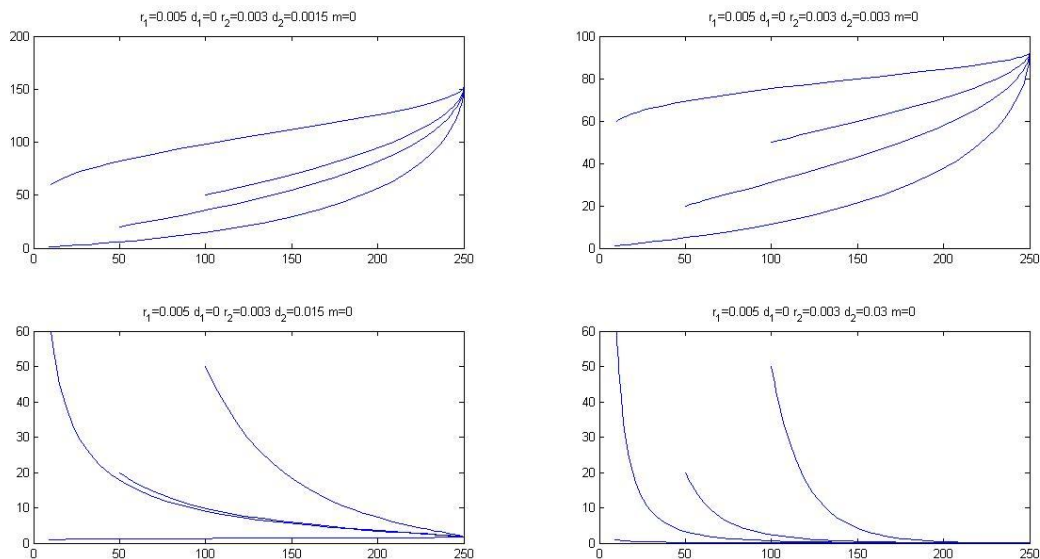


Fig.U7 Phase space graphs with different kill rates. In these figures we show the behaviours of the two populations (N_1 in the ordinate, N_2 in the abscissa) using different initial conditions. In the top of the figure the used parameters are shown: mutation rate (m) of the two cell populations and kill rates (d) of the two drugs

U4.7 Varying both the Mutation and the Kill Rate

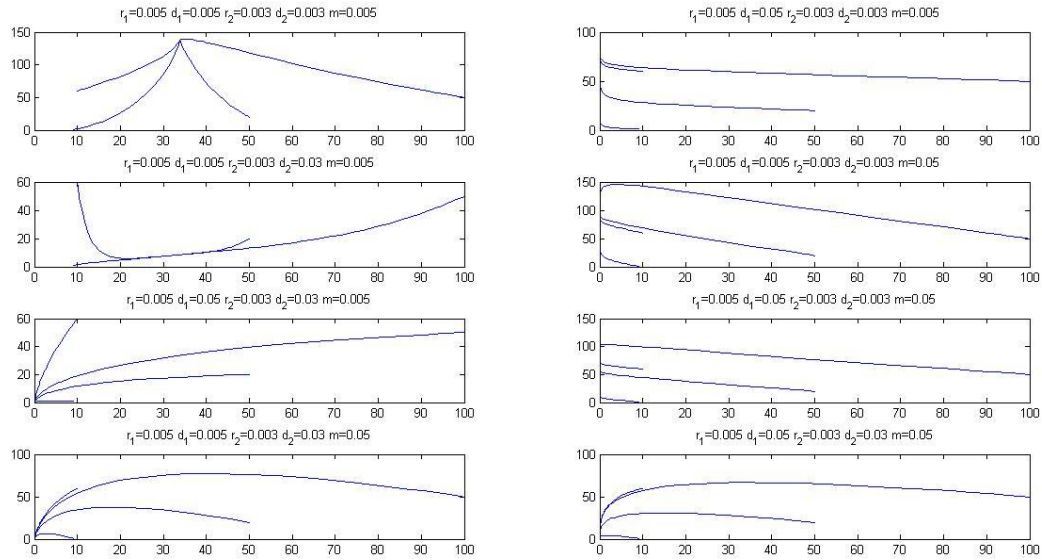
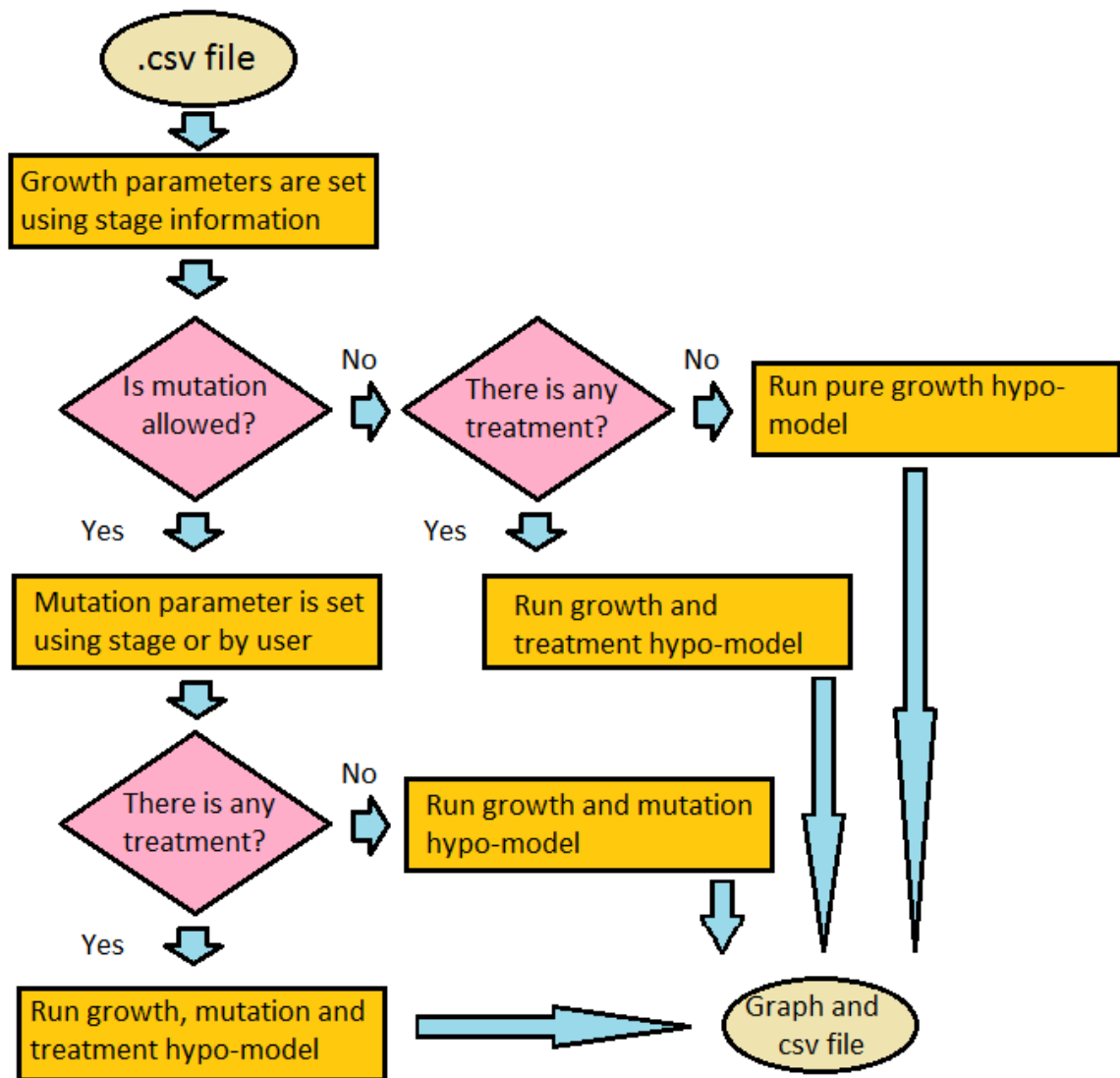


Fig.U8 Phase space graphs with different mutation and kill rates. In these figures we show the behaviours of the two populations (N_1 in the ordinate, N_2 in the abscissa) using different initial conditions. In the top of the figure the used parameters are shown: mutation rate (m) of the two cell populations and kill rates (d) of the two drugs

U5. Flowchart



U6. References

- C. Guiot et al., Does tumour growth follow a “universal law”?, *Journal of Theoretical Biology*, 225 (2003), 147-151
- L. Barberis, C.A. Condat, Describing interactive growth using vector universalities, *Ecological Modelling*, 227 (2012), 56-63

L. Barberis et al., Concurrent growth of phenotypic features: a phenomenological universalities approach, *Journal of Theoretical Biology*, 264 (2010), 123-129

P. Castorina et al., Tumour growth instability and its implications for chemotherapy, *Cancer Research*, 69 (2009), 8507-8515

G. Stamatakos et al., In silico oncology: exploiting clinical studies to clinically adapt and validate multiscale oncosimulators, 35th Annual International Conference of the IEEE EMBS, Osaka, Japan, 3-7 July 2013

U7. Description of the Gross Component Models Based on Simplified Universal Growth Laws through the 13 Perspectives

TABLE "U-13P" (FIRST PART)		
PERSPECTIVE CODE NUMBER	PERSPECTIVE TITLE	PERSPECTIVE VALUE(S)
I	TUMOUR-AFFECTED NORMAL TISSUE MODELLING	tumour normal tissue
II	SPATIAL SCALE(S) OF THE MANIFESTATION OF LIFE	molecular cellular tissue
III	TEMPORAL SCALE(S) OF THE MANIFESTATION OF LIFE	h d
IV	BIOMECHANISM(S) ADDRESSED	mutation mitosis necrosis apoptosis metabolism
V	TUMOUR TYPE(S) ADDRESSED	lung cancer other solid tumours
VI	TREATMENT MODALITY(-IES) ADDRESSED	chemotherapy radiotherapy targeted therapy

TABLE "U-13P" (SECOND PART)		
PERSPECTIVE CODE NUMBER	PERSPECTIVE TITLE	PERSPECTIVE VALUE(S)
VII	GENERIC CANCER BIOLOGY – CLINICALLY DRIVEN CHARACTER OF THE MODELLING APPROACH	generic cancer biology clinically driven
VIII	ORDER OF ADDRESSING DIFFERENT SPATIAL SCALES	bottom-up top-down
IX	ORDER OF ADDRESSING DIFFERENT TEMPORAL SCALES	short periods → longer periods
X	MECHANISTIC-STATISTICAL CHARACTER OF THE MODELLING APPROACH	mechanistic
XI	DETERMINISTIC-STOCHASTIC CHARACTER OF THE MODELLING APPROACH	deterministic
XII	CONTINUOUS-FINITE-DISCRETE CHARACTER OF THE MATHEMATICS INVOLVED	continuous finite (finitized continuous),
XIII	CLOSED FORM SOLUTION – ALGORITHMIC SIMULATION MODELLING APPROACH	closed form solution based modelling algorithmic simulation

A BRIEF INITIAL OUTLINE OF THE TWO ADDITIONAL MULTIMODELLER HYPERMODEL DEMONSTRATORS

In the following two chapters the initial architecture of the multimodeller hypermodels concerning the nephroblastoma and the glioblastoma multiforme scenarios of the CHIC project, currently under development and/or refinement, is briefly outlined. These two demonstrators will be developed in parallel with the clinical adaptation and partial clinical validation of the lung cancer demonstrator, as explained during the first annual review that took place in Brussels in September 2014.

W. The Wilms Tumour (Nephroblastoma) Demonstrator

W1. An initial Version of the Topology of the Nephroblastoma Multi-modeller Hyrermodel

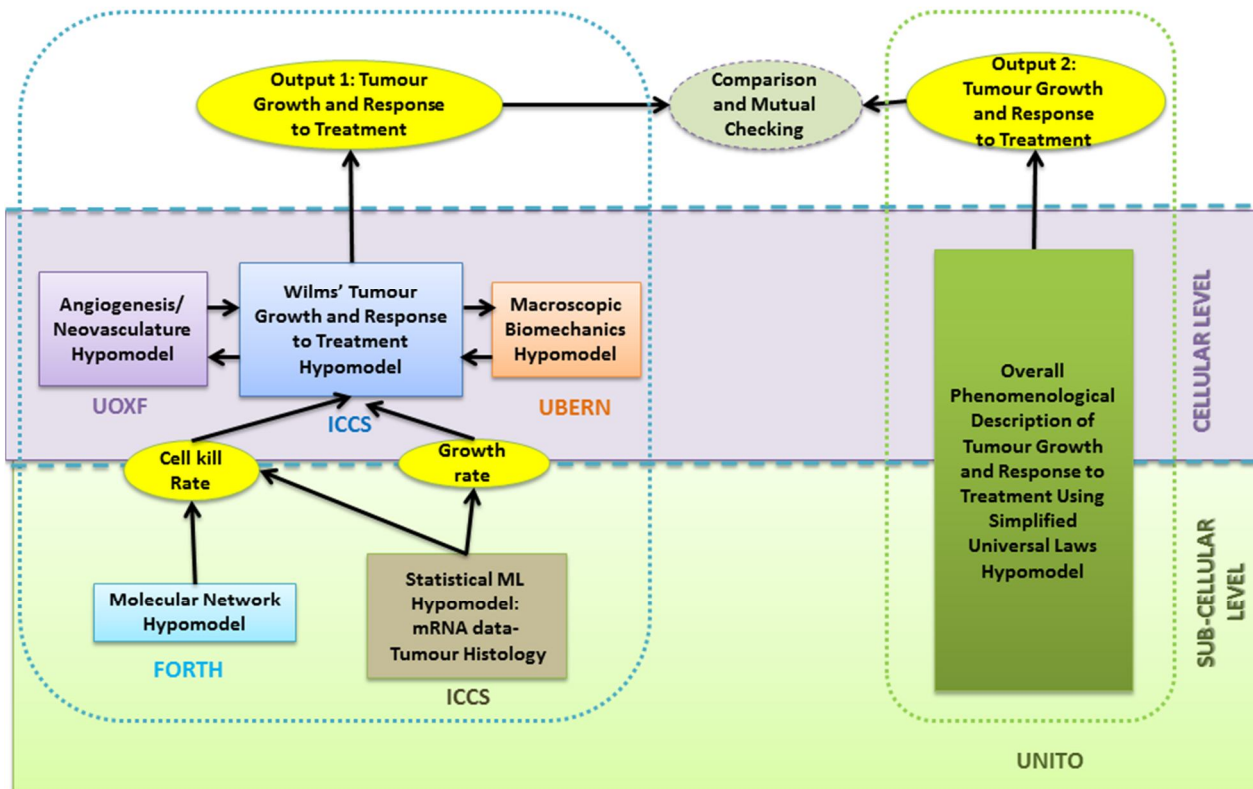


Fig. W1 Outline of an early version of the master topology of the Wilms tumour (nephroblastoma) multi-modeller hypermodel.

Although the discussions regarding the involvement of various partners is still in progress, a very brief outline of an early version of the multimodeller hypermodel concerning nephroblastoma (Wilms tumour) under development is provided here.

The hypermodel consists of two main branches:

1. A multiscale hypermodel that includes hypomodels of several critical biological mechanisms involved in the growth and response to treatment of Wilms tumours.
2. A phenomenological model simulating the tumour growth and response to treatment modalities based on simplified universal laws.

The simulating results of the two modelling branches will be compared and mutually checked. In more detail, the first branch of the hypermodel consists of the following hypomodels:

W2. Cellular and Supercellular Level

W2.1 Angiogenesis/Neovasculature Hypomodel

An angiogenesis component model quite similar to the angiogenesis component models A and AA used in the lung cancer case is to be developed and used in this case.

W2.2 Wilms Tumour Oncosimulator Hypomodel.

The Wilms Oncosimulator (Georgiadi et al., 2012, ; Stamatakis et al., 2011) is an integrated software system simulating the growth of nephroblastoma tumours and their *in vivo* response to chemotherapeutic modalities within the clinical trials environment. The nephroblastoma simulation model is a predominantly discrete, clinically oriented model of solid tumour response to treatment. Preoperative chemotherapy is the simulated form of treatment. Clinical orientation of the model has been a fundamental guiding principle throughout its development. The simulation method starts from the macroscopic imaging data of patients (MRI images). A finite number of states of the model is defined by several different types of biological cells. The transition rules of the cells from one state to another form the “decision calculators” and define the evolution and interaction rules between the predefined number of finite states of the model. In this way, several cellular-level biological phenomena that are reported in literature are incorporated in the model such as cell proliferation, quiescence, differentiation and death (normal and chemotherapy-induced). The aggregation of all the evolution and interaction rules form the “decision calculator”. The transition rates between the different states form the dynamic parameters of the model. These parameters will be considered space and time dependent in order to model the inhomogeneity (macroscopically/metabolically distinct regions) of the tumour volume, as well as the metabolic changes of the tumour due to eg. angiogenesis. The output of the model at any given instant will be the distribution of the cells of various categories, the total tumour volume, the growth rate of the tumour, the doubling time of the tumour as well as the volume reduction due to a therapeutic scheme. The model is developed in C++ programming language.

W2.3 Macroscopic Biomechanics Hypomodel

The biomechanics component model will be quite similar to the one developed for the lung cancer case.

W3. Sub-cellular Level

W3.1 Molecular Network Hypomodel

A molecular network / molecular pathway component model will be developed in order to exploit knowledge and data at the molecular level in particular related to tumour cell survival following treatment.

W3.2 Statistical Machine Learning (ML) Model to Correlate the micro-RNA data of the Patient with the Histology of Tumour

In order to exploit the micro-RNA data to be provided by the corresponding clinical partner, a statistical machine learning model will be developed. Its aim will be to correlate the micro-RNA data of the patient with the histology of the tumour. The latter plays a central role in the treatment response process.

W4. References

E.C.Georgiadi, D.D.Dionysiou, N.Graf and G.Stamatakis, "Towards In Silico Oncology: Adapting a Four Dimensional Nephroblastoma Treatment Model to a Clinical Trial Case Based on Multi-Method Sensitivity Analysis." 2012 Nov; 42(11):1064-78. doi: 10.1016/j.combiomed.2012.08.008.

S.Stamatakis, E.Ch.Georgiadi, N.Graf, E.A.Kolokotroni, and D.D.Dionysiou, "Exploiting Clinical Trial Data Drastically Narrows the Window of Possible Solutions to the Problem of Clinical Adaptation of a Multiscale Cancer Model", PLOS ONE 6(3), e17594, 2011

G. The Glioblastoma Multiforme Demonstrator

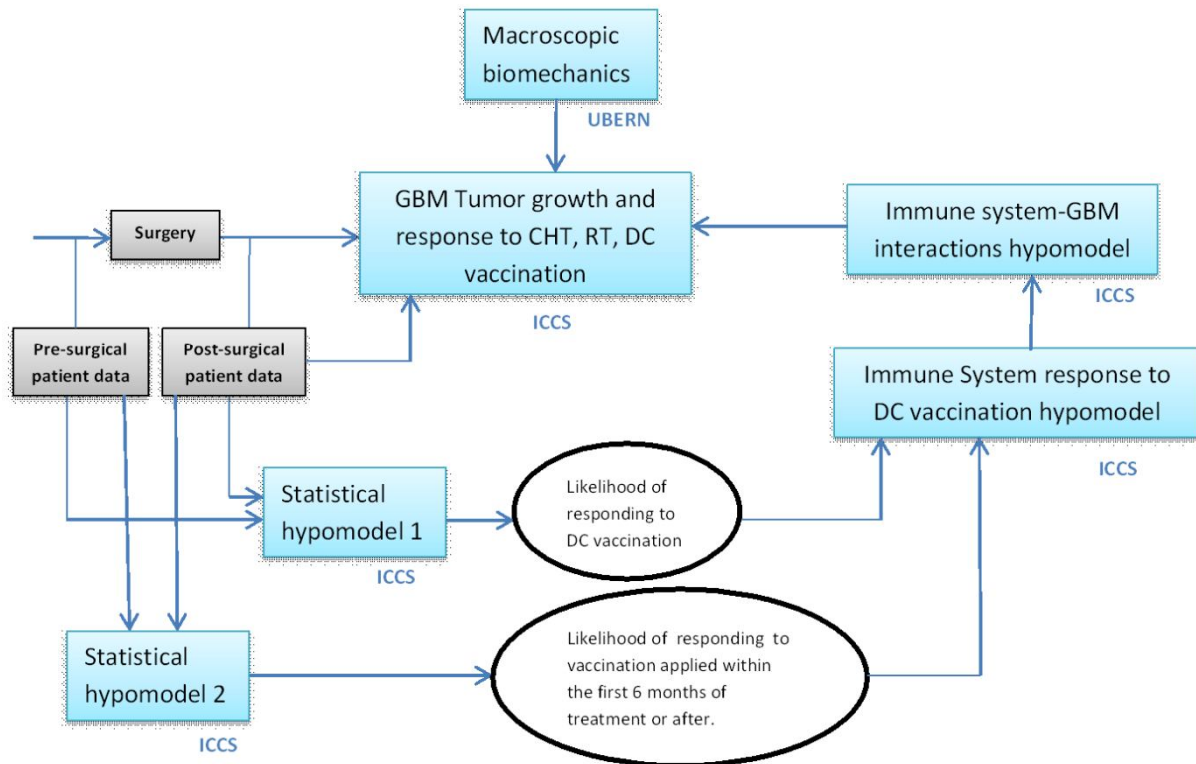
G1. Introduction

Glioblastoma multiforme, a very aggressive brain tumour, treated by classical chemotherapeutic and radiotherapeutic regimens and/or by experimental ones [G1-G4] has become the subject of intensive computer modeling approaches [G5-G9].

Dendritic cell vaccination constitutes a novel treatment for patients with glioblastoma multiforme [G1]. Integration of this particular treatment modality to standard treatment has been studied [G3] showing encouraging results. However, there are still many questions to be resolved concerning the integration of DC vaccination to standard treatment. It seems that only a rather specific patient group is likely to benefit from DC vaccination [G2],[G4] and this group remains to be determined. It is still unclear if a patient will benefit from vaccination applied at the early stages of treatment, or later. Furthermore, there is yet no clear correlation between patients' immune profile and overall outcome [G3]. Our approach, as described below, is planning to identify those missing correlations, as described by the previously stated clinical questions.

It is noted that the discussions regarding the involvement of various partners is in progress.

G2. An Initial Master Topology of the GBM Hypermodel



Fig_G1 An outline of an early version of the master topology of the Glioblastoma tumour multi-modeller hypermodel.

G2.1 Statistical Hypomodel 1

This hypomodel will classify patients to (probable) “responders” or “non-responders” to DC vaccination. It takes input from both pre-surgical and post-surgical data. If the output of this hypomodel is a non-responder one, Statistical Hypomodel 1, Immune System response to DC vaccination hypomodel and Immune system-GBM interactions hypomodel will be not used.

G2.2 Statistical Hypomodel 2

This hypomodel will be used only if the output of Statistical hypomodel 1 is positive. It also takes input from pre- and post-surgical clinical data and further classifies responders suggesting “early” or “late” DC vaccination as a more beneficial treatment strategy.

G2.3 Immune System Response to DC Vaccination Hypomodel

This hypomodel calculates the evolution of the population of various immune system cells during and after DC and tumour lysate vaccination. This hypomodel is a mechanistic one, exploiting data

concerning the actual applied vaccines (prepared using the particular patient's lymphocytes and tumour lysates) and immune monitoring measurements.

G2.4 Immune System-GBM Interactions Hypomodel

This hypomodel correlates the reshaped immune system (in terms of immune cells populations) with the immune response to GBM. It remains to be determined, if this model will be a statistical one (e.g. estimating a GBM cell kill ratio, subsequently fed to the Oncosimulator) or a mechanistic (e.g. more detailed modeling of the interactions between GBM and immune cells, subsequently coupled with the Oncosimulator).

G3. References

- [G1] de Vleeschouwer S, Rapp M, Sorg RV, Steiger HJ, Stummer W, van Gool S, Sabel M. Dendritic cell vaccination in patients with malignant gliomas: current status and future directions. *Neurosurgery*. 2006 Nov;59(5):988-99
- [G2] Van Gool S, Maes W, Ardon H, Verschuere T, Van Cauter S, De Vleeschouwer S. Dendritic cell therapy of high-grade gliomas. *Brain Pathol*. 2009 Oct;19(4):694-712.
- [G3] Ardon H1, Van Gool SW, Verschuere T, Maes W, Fieuws S, Sciote R, Wilms G, Demaerel P, Goffin J, Van Calenbergh F, Menten J, Clement P, Debiec-Rychter M, De Vleeschouwer S. Integration of autologous dendritic cell-based immunotherapy in the standard of care treatment for patients with newly diagnosed glioblastoma: results of the HGG-2006 phase I/II trial. *Cancer Immunol Immunother*. 2012 Nov;61(11):2033-44.
- [G4] Dejaegher J, Van Gool S, De Vleeschouwer S Dendritic cell vaccination for glioblastoma multiforme: review with focus on predictive factors for treatment response *ImmunoTargets and Therapy* Vol. 2014:3 Pages 55—66
- [G5] G.S. Stamatakis, D.D. Dionysiou, E.I. Zacharaki, N.A. Mouravliansky, K.S. Nikita, N.K. & Uzunoglu, In silico radiation oncology: combining novel simulation algorithms with current visualization techniques, *IEEE Proceedings: Special Issue on Bioinformatics: Advances and Challenges*, 90(11), 1764-1777, 2002
- [G6] D.D. Dionysiou, G.S. Stamatakis, N.K. Uzunoglu, K.S. Nikita, A. Marioli, A Four Dimensional In Vivo Model of Tumour Response to Radiotherapy: Parametric Validation Considering Radiosensitivity, Genetic Profile and Fractionation, *J. theor. Biol.*, 230, 1-20, 2004
- [G7] G.S. Stamatakis, V.P. Antipas, and N.K. Uzunoglu, A spatiotemporal, patient individualized simulation model of solid tumor response to chemotherapy in vivo: the paradigm of glioblastoma multiforme treated by temozolomide, *IEEE Transactions on Biomedical Engineering*, 53(8), 1467-1477, 2006
- [G8] G. Stamatakis "In Silico Oncology Part I: Clinically Oriented Cancer Multilevel Modeling Based on Discrete Event Simulation" In T. Deisboeck and G. Stamatakis Eds 407-436 2011-01-01 CRC Press, Print ISBN: 978-1-4398-1440-6 eBook ISBN: 978-1-4398-1442-0 DOI: 10.1201/b10407-19 Boca Raton, Florida, USA, 2011
- [G9] S. Giatili and G. Stamatakis "A Detailed Numerical Treatment of the Boundary Conditions Imposed by the Skull on a Diffusion-Reaction Model of Glioma Tumor Growth. Clinical Validation Aspects." *Applied Mathematics and Computation Appl. Math. Comput* vol.218 (Issue 17) pp. 8779-8799 2012

S. An Outline of the Overall Strategy of the CHIC Project

In order to link the content of the present deliverable concerning fundamental research (basic science) to the overall project implementation, this section briefly outlines the overall strategy of CHIC (Fig. S1). Clinical reality serves as the overall driver of the project. It drives clinical medicine in the sense that clinical medicine formulates concrete questions that should be answered in order to solve or approach the solution of the addressed clinical problems. Clinical medicine in turn drives fundamental research (basic science) and in particular the development of cancer hypermodels. It is noted that in the future other disease hypermodels will be possible to develop as well. Fundamental research acts as the driver of technology. The project technological infrastructure, tools, procedures and repositories should be designed in such a way so as to effectively support the semi-automatic development of hypermodels. The final integrated construct including the technological layer serves as the driver of the multifaceted exploitation activities spanning from academic exploitation (new academic domain courses and subjects) to the translation of the CHIC system and subsystems into the clinical environment. The latter concerns the clinical adaptation, the clinical validation and the clinical utilization of hypermodels and hypermodel based oncosimulators. It is pointed out that the clinical medicine, fundamental research (basic science), technology and exploitation development layers are supervised (overseen) by the law and ethics related activities and procedures in order to ensure compliance of the CHIC project with the corresponding legislation and ethical principles.

The exploitation process generates “feedback signals” which are used in order to assess the degree of improvement of the clinical reality (clinical conditions) when the CHIC integrated system or particular components are used. From an abstract epistemologic perspective it is worth noting that part of the overall work refers to reality (clinical medicine, clinical medicine, most of the technology layer, exploitation and law and ethics) whereas another part refers to virtuality (fundamental research and part of technology). Obviously coordination and management provide the overall orchestration and housekeeping of the project implementation. It is expected that the completion of the implementation of the CHIC project will lead to a crucial contribution to the advancement of the emergent scientific and technological domain of *in silico* oncology, the latter being at the same time an excellent paradigm of the broader domain of *in silico* medicine.

THE CHIC PROJECT “DRIVING DIAGRAM”

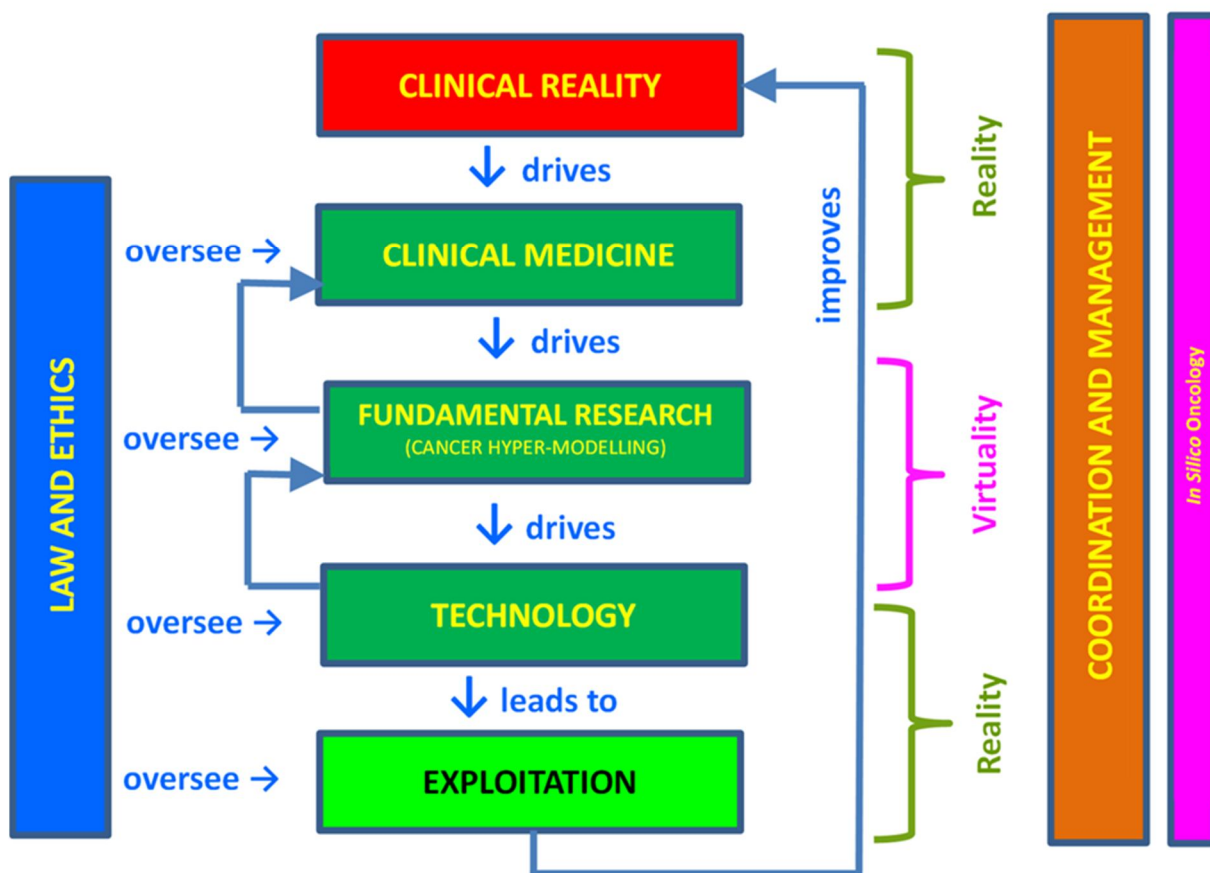


Fig. S1 A brief overall outline strategy of the CHIC project

V. VOCABULARY

V1. Definitions

V1.1 Introduction

The objective of this chapter is to present a set of definitions that will introduce the reader into the domain that the CHIC project belongs to and to provide the descriptions of the fundamental concepts and terms that will be used in the CHIC project. The collaborating efforts of all members of the CHIC consortium have resulted into the collection of a wide set of concepts and terms.

V1.2 Generic definitions

V1.1.1 *In silico*

In silico is an expression used to mean “performed on a computer or via computer simulation”. The phrase was coined in 1989 as an analogy to the Latin phrases *in vivo*, *in vitro*, and *in situ*, which are commonly used in biology and refer to experiments done in living organisms, outside of living organisms, and where they are found in nature, respectively³.

V1.1.2 *In silico* Medicine

In silico medicine (also known as “computational medicine”) is the application of *in silico* research to problems involving health and medicine. It is the direct use of computer simulation in the diagnosis, treatment, or prevention of a disease. More specifically, *in silico* medicine is characterized by modelling, simulation, and visualization of biological and medical processes by use of computers with the goal of simulating real biological processes in a virtual environment⁴.

V1.1.3 Virtual Physiological Human (VPH)

The Virtual Physiological Human (VPH) is a methodological and technological framework that enables collaborative investigation of the human body as a single complex system. The collective framework makes it possible to share resources and observations formed by institutions and organizations creating disparate but integrated computer models of the mechanical, physical and biochemical functions of a living human body⁵.

³ http://en.wikipedia.org/wiki/In_silico

⁴ http://en.wikipedia.org/wiki/In_silico_medicine

⁵ STEP Consortium. Seeding the EuroPhysiome: A Roadmap to the Virtual Physiological Human. 5 July 2007

V1.3 Scientific and Technological Definitions

V1.3.1 Data

We define data as factual information, whether observed or predicted.

- Observed: generated through observation, measurement etc.
- Predicted: generated through speculative reasoning informed by existing knowledge.

V1.3.2 Scientific Model

We can define a scientific model as a finalized cognitive construct of finite complexity that idealizes an infinitely complex portion of reality through idealizations that contribute to the achievement of knowledge on that portion of reality that is objective, shareable, reliable and verifiable⁶.

V1.3.3 Computer Model

We define a computer model as a computer program that implements a scientific model, so that, when executed according to a given set of control instructions (control inputs), it computes certain quantities (data outputs) on the basis of a set of initial quantities (data inputs) and a set of execution logs (control outputs).

V1.3.4 Metadata

Metadata is “data about data”. The term is ambiguous, as it is used for two fundamentally different concepts (types)⁷.

- Structural metadata refers to the design and specification of data structures and is more properly called “data about the containers of data”.
- Descriptive metadata, on the other hand, refers to individual instances of application data, i.e. the data content.

V1.3.5 Ontology (Computer Science)

In computer science and information science, an ontology formally represents knowledge as a set of concepts within a domain, using a shared vocabulary to denote the types, properties and interrelationships of those concepts.

⁶ Viceconti M 2011 A tentative taxonomy for predictive models in relation to their falsifiability. Philos Transact A Math Phys Eng Sci 369(1954):4149-61.

⁷ <http://en.wikipedia.org/wiki/Metadata>

V1.3.6 Folksonomy (Computer Science)

In information science, a folksonomy is a system of classification derived from the practice and method of collaboratively creating and translating tags to annotate and categorize content. This practice is also known as collaborative tagging, social classification, social indexing, and social tagging.

V1.3.7 Orchestration or Choreography (Technology)

In the context of Service-Oriented Architectures (SOA) the two terms indicate the coordinated execution of multiple services. Different authors use the two terms differently⁸. However, in cases like ours where the execution of the services is coordinated centrally (autocratic) the term orchestration is preferred.

⁸ <http://www.infoq.com/news/2008/09/Orchestration>

V1.4 CHIC Project Definitions

V1.4.1 Model

In CHIC project we use the general term “model” in order to define a mathematical or computational construct incorporating speculative information that represents the existing knowledge. Computational implementation of such a model is capable of virtually regenerating an entity or phenomenon. The above definition is in alignment with the terms “scientific model” and “computational model” described in sections 3.3.2 and 3.3.3, respectively.

V1.4.2 Hypomodel (or Component Model)

We define as a hypomodel (or component model) a model that captures the existing knowledge about a portion of the process, typically at a characteristic space-time scale, and simulates a simpler entity or phenomenon compared to a model or a hypermodel (Fig. V1) .

V1.4.3 Hypermodel (or Composite Model or Integrative Model)

We define as a hypermodel (or composite model or integrative model) a model that emerges from the composition and orchestration of multiple hypomodels, each one of which is capable of simulating a specific entity or phenomenon. The hypermodel can simulate an entity or phenomenon that may be more complex than the ones simulated by each separate simpler model (Fig. V1) .

V1.4.4 Elementary Model

We define as an elementary model a model that, from a particular standpoint, appears (subjectively) not amenable to decomposition into meaningful simpler models, mainly because the current scientific knowledge and technological status cannot support such a decomposition. It is almost certain that future scientific discoveries and technological advantages will allow models that presently are considered as elementary models to be further decomposed into new elementary models.

V1.4.5 Meta-model, meta-hypomodel, meta-hypermodel

We define as a meta-model the semantic description of a model. The meta-model can be considered as an abstract representation of a model, as it highlights certain properties of the model itself. Consequently, a meta-hypomodel and a meta-hypermodel is the semantic description of a hypomodel and a hypermodel respectively.

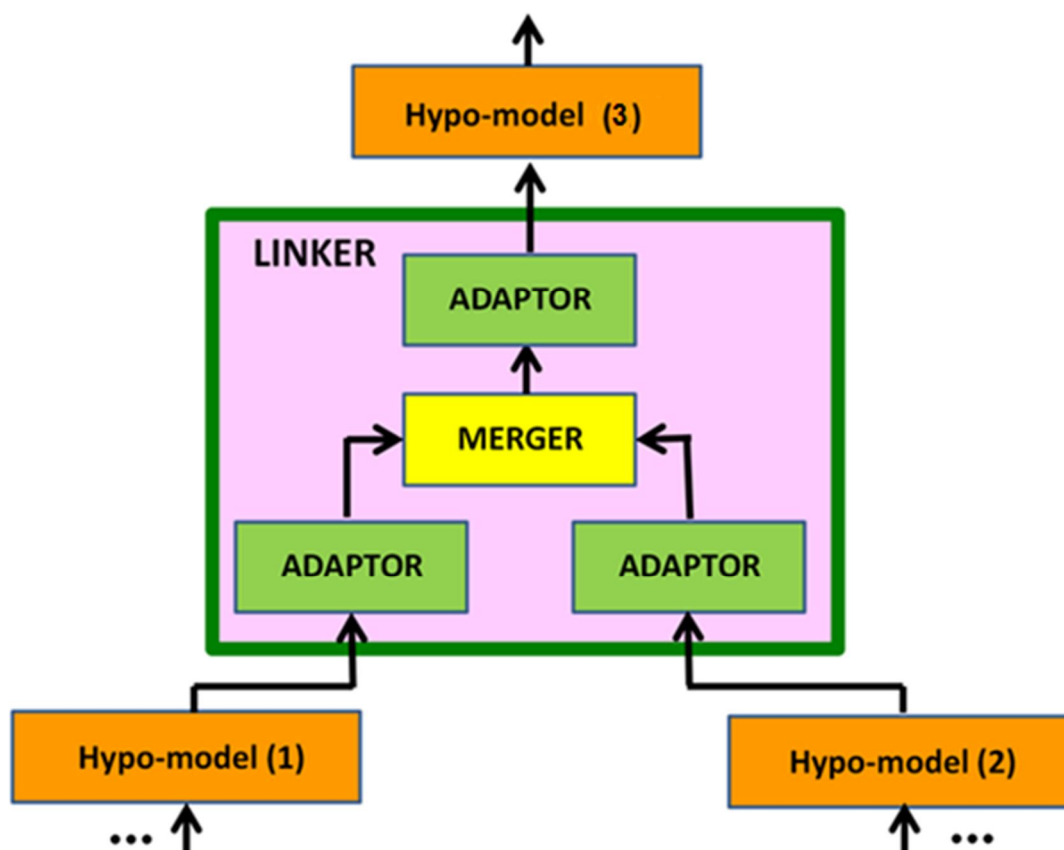


Fig. V1 Graphical representation of the linker, the adaptor and the merger. The whole figure can be viewed as representing a single hypermodel.

V1.4.6 Adaptor or Relational Model

We define as an adaptor (or relational model) a piece of software that adapts/transforms the predicted output of a hypomodel so as to enable its provision as input to another hypomodel (Fig. V1).

V1.4.7 Merger

We define as a merger a piece of software that merges the adequately adapted outputs of two hypomodels (Fig. V1).

V1.4.8 Linker

We define as a linker a piece of software inserted between the outputs of two hypomodels and the input of a third hypomodel so as to allow the merged and adapted output of the two hypomodels to be fed into the third hypomodel. The linker consists generally of adaptors and a merger. The linkers and the participating hypomodels are the constructive elements of a hypermodel (Fig. V1).

V1.4.9 Hypermodelling

We define as hypermodelling the process of developing hypermodels.

V1.4.10 Hypermodelling Infrastructure

We define as hypermodelling infrastructure the set of technological components that facilitates the development of hypermodels and allows their execution. This includes both software and hardware.

V1.4.11 Hypermodelling Framework

We define as hypermodelling framework the software layer that facilitates the development of hypermodels and allows their execution. The various models and the supplementary components (adaptors, mergers, linkers, etc.) are not considered to be part of the framework themselves, but they are retrieved or invoked upon request.

C. Conclusion

The present document has provided a fairly detailed outline of the initial tested versions of those component models (hypomodels) developed by different cancer modelling groups across the globe that will be utilized in order to build the first integrated hypermodel demonstrator concerning lung cancer. The types of multiscale clinical data being provided by the Pathology Department of the University of Saarland, Homburg, Germany have served as the clinical driver of the hypermodel and its constituent component models (hypomodels). Each hypomodel corresponds to one or more than one crucial biomechanism of the natural phenomenon of cancer. A master topology of the corresponding hypermodel has been presented. For each hypomodel its main tasks, its input and output parameters as well as several indicative behaviour and testing results have been delineated. According to the Description of Work of the CHIC project, clinical adaptation and clinical validation of the entire hypermodel will take place after the completion of the multimodeller hypermodel demonstrator. A metamodeling description of each hypomodel based on the CHIC 13 perspective approach which will facilitate its technology mediated linking has also been provided. The work that has been presented in this document will serve as a credible basis for the next steps of hypermodel development both from the fundamental (basic) science and the technology standpoints. A brief outline of the initial architecture of the multimodeller hypermodels concerning the nephroblastoma and the glioblastoma scenarios of the CHIC project, currently under development and/or refinement, has also been included. Furthermore, some important aspects of the overall strategy of the CHIC project have been presented in order to provide a broader view of the CHIC project deployment approach. A vocabulary of the main terms used throughout this and other deliverables has been provided at the end of the document.

Appendix 1 – Abbreviations and Acronyms

ADC	Adenocarcinoma
ADSCC	Adenosquamous Cell Carcinoma
Akt	Protein kinase B (PKB)
ALK	Anaplastic Lymphoma Kinase
AMD	Advanced Microdevices
AUC	Area Under Curve
BS	Biomechanics Simulator
CHIC	Computational Horizons in Cancer
CKR	Cell Kill Rate
COSMIC	Catalog of Somatic Mutations in Cancer
CS	Cell Simulator
CSF	Cerebrospinal Fluid
CSS	Cancer Stem Cell
CSV	Comma Separated Values
DC	Dendritic Cell
DIFF	Differentiated Cell
EGF	Epidermal Growth Factor
EGFR	Epidermal Growth Factor Receptor
ERBB2	erb-b2 Receptor Tyrosine Kinase 2
ERK	Extracellular Signal-Regulated Kinases
FEM	Finite Element Method
FORTH	Foundation for Research and Technology Hellas
GBM	Glioblastoma Multiforme
GC	Geometrical Cell
HER3	Human Epidermal Growth Factor Receptor 3
ICCS-NTUA	Institute of Communication and Computer Systems – National Technical University of Athens
KUL	Catholic University of Leuven
LCC	Large Cell Carcinoma
LIMP	Limited Mitotic Potential
MAPK	Mitogen-Activated Protein Kinase
MD	Molecular Dynamics
MUT	Mutant
NBC	Number of Biological Cells
NCI	National Cancer Institute
NGCT	Neighbour Geometrical Cells belonging to the Tumour
NIH	National Institutes of Health
NSCLC	Non Small Cell Lung Cancer
NSG	NOD- <i>scid</i> <i>IL2ry</i> ^{null} Mouse Model of Human Skin
OFAT	One Factor at A Time
pAKT	phospho-AKT

PDE	Partial Differential Equation
RTK	Receptor Tyrosine Kinase
SASA	Solvent Accessible Surface Area
SBML	Systems Biology Markup Language
SCC	Squamous Cell Carcinoma
SCID	Severe Combined ImmunoDeficient
SCLC	Small Cell Lung Cancer
STAT	Signal Transducer and Activator of Transcription or Signal Transduction And transcription
SVM	Support Vector Machines
TCGA	The Cancer Genome Atlas
TKI	Tyrosine Kinase Inhibitors
UBERN	University of Bern
ULC	Undifferentiated Large Cell Carcinoma
UNITO	University of Turin
UOXF	University of Oxford
UPENN	University of Pennsylvania
USAAR	University of Saarland
USFD	University of Sheffield
VPH	Virtual Physiological Human
VEGF	Vascular Endothelial Growth Factor
WT	Wild Type
XML	EXtensible Markup Language